Vapor-liquid-solid growth of semiconductor nanowires

Vladimir G. Dubrovskii, Frank Glas

Vapor-liquid-solid growth of semiconductor nanowires

Vladimir G. Dubrovskii[1*] and Frank Glas[2]

[1]ITMO University, Kronverkskiy pr. 49, 197101 St. Petersburg, Russia

[2]Université Paris-Saclay, CNRS, Centre for Nanoscience and Nanotechnology, 10 bd. Thomas Gobert, 91120 Palaiseau, France

[*]Corresponding author, e-mail: dubrovskii@mail.ioffe.ru

[2]e-mail: frank.glas@c2n.upsaclay.fr

Abstract

We discuss the growth of semiconductor nanowires, with an emphasis on the vapor-liquid-solid growth of III-V nanowires. Special attention is paid to modeling of growth and the resulting morphology, crystal phase, composition, nanowire heterostructures and statistical properties within the nanowire ensembles. We give a general overview of the vapor-liquid-solid growth of nanowires by different epitaxy techniques and the bases for nanowire growth modeling. We discuss the role of surface energetics in the formation of GaAs nanowires, which has an important impact on the nanowire morphology and crystal phase. A detailed description of the nanowire growth kinetics is prersented, including the transport-limited growth, chemical potentials, nucleation and growth of two-dimensional islands and self-consistent growth models combining the material transport equations with the nucleation rate. The nanowire length and diameter distributions are considered along with the methods for narrowing them to sub-Poisonian values. Ternary III-V nanowires and heterostructures based on such nanowires are discussed, including the relaxation of elastic stress at the free sidewalls and the sharpening the heterointerfaces. We consider polytypism of III-V nanowires and possibilities to control their crystal phase by tuning the growth parameters.

Keywords: III-V nanowires, vapor-liquid-solid growth, nucleation, growth modeling.

1. Introduction

In this chapter, we discuss the growth of semiconductor nanowires, wich an emphasis put on the vapor-liquid-solid growth of III-V nanowires. Particular attention is paid to theoretical understanding and the relevant models for the growth, morphology, crystal phase, composition and statistical properties within the naniowire ensembles.

The chapter is organized as follows. Section 2 gives a general description of the vapor-liquid-solid growth by different epitaxy techniques, including the role of equilibrium phase diagrams, growth in reguar arrays on patterned substrates such as SiO_x/Si(111), Au-catalyzed and self-catalyzed growth of III-V nanowires. We also present some recent examples of shaping GaAs nanowires in the self-catalyzed approach. In section 3, we review the basics for the nanowire growth modeling, including the kinetics of group III and V species, axial growth rate, the role of supersaturation, nucleation-limited and regular growth modes. Section 4 deals with the role of surface energetics in the vapor-liquid-solid growth of GaAs nanowires, which has an important impact on the nanowire morphology and crystal phase. Section 5 presents a brief decription of selective area epitaxy of III-V nanowires and a model for such growth. In section 6, we consider a detailed description of the nanowire growth kinetics, including the transport-limited growth, chemical potentials for the vapor-liquid-solid growth of III-V nanowires, nucleation and growth of two-dimensional islands at the liquid-solid interface, and some advanced self-consistent growth models combining the material transport equations with the Zeldovich nucleation rate.

Section 7 desribes an interesting effect of radius self-equilibration in self-catalyzed III-V nanowires. Section 8 presents the recent results on the length distributions within the ensembles of different III-V nanowires, including the role of surface diffusion and delayed nucleation of nanowires on the substrate surface, and possibilities to obtain sub-Poissonian length distributions induced by nucleation antibunching. Section 9 deals with ternary alloys in nanowires, and

describes some theoretical models for the nanowire composition. In section 10, we consider heterostructures within nanowires, in particular, relaxation of elastic stress induced by lattice mismatch, the vapor-liquid-solid growth of axial heterostructures in different III-V material systems, and sharpness of the nanowire heterointerfaces. Section 11 deals with the zincblende-wurtzite polytypism in III-V nanowires and its theoretical understanding achieved to this day.

2. Vapor-liquid-solid growth of semiconductor nanowires

The vapor-liquid-solid (VLS) method was introduced by Wagner and Ellis in 1964 to grow sub-micrometer Si "whiskers" on Si(111) substrates with Au catalyst [1]. Many fundamental aspects of the VLS growth of elemental and compound semiconductors were later developed by Givargizov [2]. At the beginning of the 2000s, a rapid development of semiconductor nanowires (NWs) started, lead by the groups of Lieber [3], Yang [4] and Samuelson [5], soon followed by many others. This has resulted in tremendous progress in the NW synthesis, characterization and applications (see, for example, Refs. [3,4,6,7] for a review). One important advantage of NWs is that they allow for a very efficient relaxation of elastic stress induced by lattice mismatch on the lateral sidewalls, thus enabling dislocation-free growth on dissimilar substrates (such as Si for III-V NWs), and in NW heterostructures [8-10]. Peculiarities of the VLS growth from nanoscale catalyst droplets in largest measure determines the resulting morphology, crystal quality and phase, and statistical properties within the NW ensembles, which explains the importance of theoretical understanding and modeling [6,7].

The VLS method makes use of a catalytic effect of a liquid metal droplet such as Au to fabricate semiconductor NWs which grow away from the substrate, with the position determined by the initial location of the droplet on the substrate. Usually, NWs grow in <111> direction perpendicular to (111) substrate. Parasitic growth between the NWs is either completely suppressed (for example, by using lithographically patterned substrates with a mask oxide layer) or proceeds at a lower rate than that of NWs. Radial growth rate of NWs by the vapor-solid (VS)

mechanism on the sidewalls or due to non-stationary droplet swelling is much lower than the axial one. In chemical epitaxy techniques, a liquid metal acts as a chemical catalyst which enhances the cracking efficiency of semiconductor precursors at the droplet surface, so ideally NWs would grow only axially [1,2,5]. In molecular beam epitaxy (MBE) [11,12], the droplet acts as a material collector (or a "physical" catalyst) which directs the material diffusion fluxes to the NW top. Whatever the epitaxy technique used to grow NWs, the VLS process necessarily involves two phase transitions of a semiconductor material: from vapor (for example, Ga and As2 beams in MBE) to liquid (Au-Ga-As liquid alloy in the droplet) and from liquid to solid (stoichiometric GaAs NW). This explains the term "vapor-liquid-solid" growth.

The nature of Au-catalyzed VLS growth, particularly for elemental semiconductors such as Si or Ge, can be understood through the equilibrium phase diagrams [1-3]. Let us consider the phase diagram shown in Figure 2.1 for a binary alloy of Au with a NW material M. At least in the M-rich region of the diagram (for large enough M fractions x), the solid state is immiscible and consists of pure GaAs and Au crystallites. In this region, above the eutectic temperature T_e and below the liquidus, the system consists of a mixed M-Au liquid and pure M crystallites, with temperature-dependent fractions of liquid and the remaining solid M. Above the liquidus, the M-Au alloy becomes a single liquid melt. Therefore, any growth temperature T between T_e and $T_{\max}$ for a given composition x (determined, say, by material flux) will produce solid M NW, with the remaining liquid melt in the droplet seated on the NW top. In other words, no Au should incorporate to the NW according to the equilibrium phase diagram. This property of the binary Au-Si, Au-Ge or pseudo-binary Au-GaAs alloys explains why Au is the most common catalyst to grow NWs. According to the lever rule [13], the fraction of liquid equals $(1-x)/(1-x_L)$, while the fraction of solid M equals $(x-x_L)/(1-x_L)$, with x_L the M content in liquid.

Of course, using pseudo-binary diagrams for Au-III-V alloys (that is, assuming stoichiometric GaAs composition in the liquid phase) is not very relevant due to the known low

solubility of highly volatile group V elements such as As and P in liquids [14]. Therefore, Au-III-As or Au-III-P liquid melts contains very small fractions of the group V elements rather than being stoichiometric. This property considerably complicates theoretical treatment as will be explained in what follows.

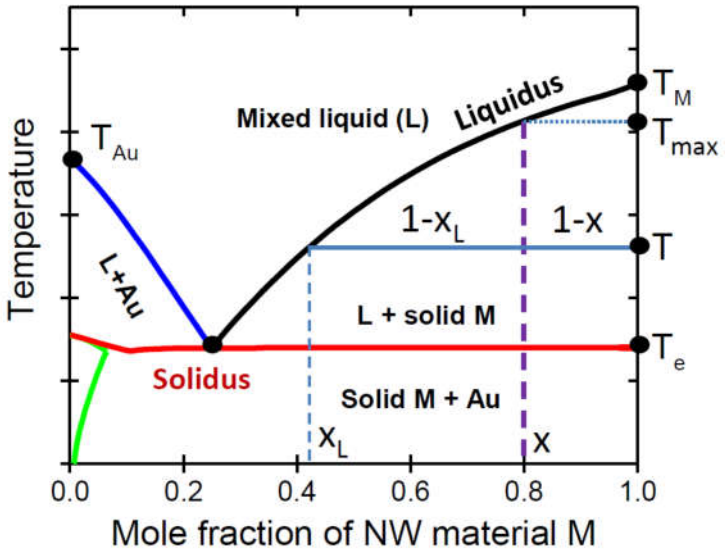

Figure 2.1. Liquid-solid phase diagram of M-Au alloy, characterized by an almost horizontal solidus at the eutectic melting temperature T_e, and the two liquidus lines separating a mixture of M-Au liquid with solid Au (for low fractions of M), or solid M (for high fractions of M) for lower temperatures, from a single melt at higher temperatures. The temperatures T_{Au} and T_M correspond to melting of pure Au (1064 ^{o}C) and M, respectively. Vertical dashed line corresponds to a fixed M fraction of 0.8. Horizontal blue line is the tie line at the growth temperature T. The M content in liquid M-Au alloy at this temperature is x_L and the fraction of liquid is $(1-x)/(1-x_L)$, while the fraction of solid M is $(x-x_L)/(1-x_L)$.

Specifically for III-V NWs, Au-catalyzed VLS growth with a high degree of control over the position, morphology, composition and crystal phase has been achieved in a wide range of epitaxy techniques, including metal organic vapor phase epitaxy (MOVPE, also known as metal organic chemical vapor deposition, MOCVD) [5,15,16], chemical beam epitaxy (CBE, the same as molecular organic MBE, MO-MBE) [17,18], and MBE [11,12,19]. In MOVPE, both group III and V elements are supplied in the form of chemical precursors, such as TMGa [$Ga(CH_3)_3$] for Ga and AsH_3 for As, in a carrier gas flow (H_2). CBE uses metal-organic precursors for the group III and either hydride gases or metal-organics TBAs (TBP) for the group V elements under high

vacuum conditions. In MBE (either solid source or gas-source), III-V materials are deposited from an atomic beam of the group III element (Ga) and molecular beam of the group V element (As_4 or As_2 after pre-cracking). Hydride vapor phase epitaxy (HVPE), which uses chloride precursors for the group III element (GaCl) and hydride gases for the group V element in a vector from of H_2 with some additional HCl, yields a less controlled nucleation but on the other hand enables the highest aspect ratio and crystal quality in the zincblende (ZB) phase of GaAs NWs [20]. Despite this variety of techniques, the major difference between them is in the different mechanisms and kinetic pathways of delivering the material into the droplet and onto the substrate surface. These differences result in more or less regular nucleation of NWs (which also depends on the substrate preparation), parasitic growth and, most importantly, different group III and V contents in an Au-III-V droplet at the typical temperatures employed in a particular growth method. The latter manifests through different axial growth rates, which are typically on the order of 1 nm/s in MBE, 1-10 nm/s in MOVPE, and reach 40 nm/s in HVPE. However, the liquid-solid phase transition can be understood from a general perspective, because the liquid alloy in any case consist of a mixture of group III and V atoms with Au.

Au-catalyzed VLS growth of III-V NWs usually consists of the following steps:

1) Preparation of the substrate surface with the Au catalyst particles;

2) Annealing the surface above the melting temperature of the alloy of Au with a given substrate material to produce liquid droplets.

3) Deposition of semiconductor material, where the properties of the NW ensembles (surface density, size uniformity, mean length, width, shape and even the crystal phase) can be tuned by the deposition conditions such as the growth time, temperature, group III and V fluxes.

In particular, Figure 2.2 illustrates the Au-catalyzed VLS growth of GaAs NWs by MBE on GaAs(111)B substrate in the simplest procedure where a thin solid Au layer is pre-deposited onto the substrate outside the MBE growth chamber. Then the substrate is transferred to the growth chamber and annealed above the eutectic temperature of Au-Ga alloy (the influence of

As can be ignored in this stage) to break the Au film into an ensemble of liquid droplets, with a broad Gaussian-like size distribution. Deposition of GaAs at a temperature of around 550 ^{o}C leads to rapid VLS growth of <111>B oriented NWs, and a much slower growth of a rough parasitic GaAs layer between the NWs. The resulting NW ensemble is irregular in terms of random positioning, broad length and radius distributions originating from the initial size inhomogeneity of the droplets and random character of the NW nucleation.

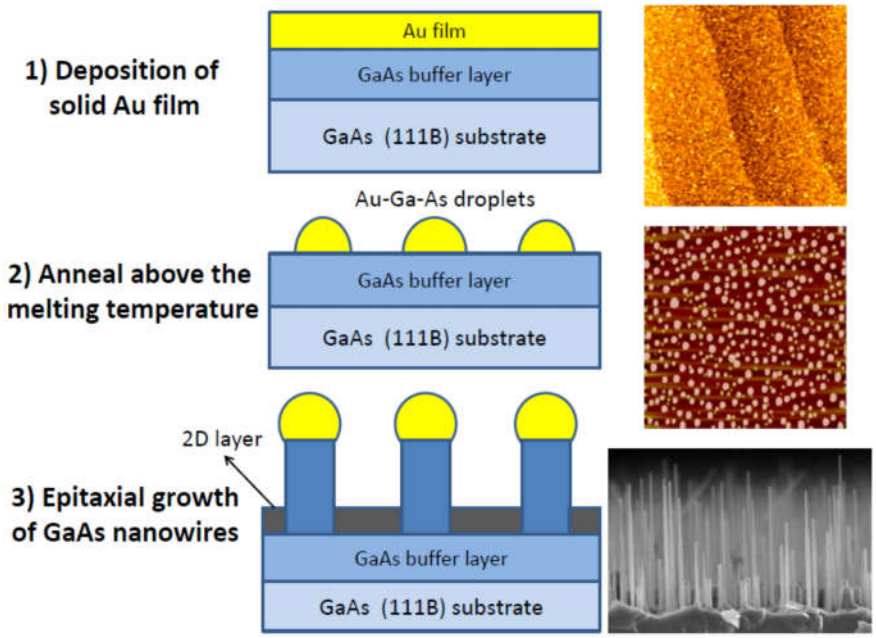

Figure 2.2. Illustration of the Au-catalyzed VLS growth of GaAs NWs on GaAs(111)B substrate by MBE with pre-deposition of ~ 1 nm thick solid Au layer. Atomic force microscopy (AFM) images show the surface after Au deposition (1st stage) and three-dimensional (3D) droplets after annealing (2nd stage). Scanning electron microscopy (SEM) image shows the vertically aligned GaAs NWs (3rd stage). Reprinted from Semiconductors and Semimetals, vol. 93, V. G. Dubrovskii, Theory of VLS growth of compound semiconductors, pp. 1-78. Copyright (2015), with permission from Elsevier.

In order to achieve more regular ensembles of NWs, Au particles can be organized before growth using electron beam [17] or nanoimprint [21] lithographical patterning of a substrate. In particular, Figure 2.3 presents the examples of InP/GaP core-shell NW arrays grown by MO-MBE from the organized Au seeds in the openings of a SiN_x mask layer on InP(111)B [17]. Compared to Figure 2.2, these NW structures (i) are positioned in regular arrays, with the inter-NW distance and arrangement determined by the lithographically defined pitch; (ii) have no

parasitic layer between the NWs, because semiconductor material does not stick onto the inert mask layer and (iii) are more regular in terms of both radius and length. The latter feature is explained by the fact that the initial growth seeds have a narrower size distribution compared to the case of thermally de-wetted Au droplets. It will be shown later that the axial NW growth rate depends on the droplet size and hence more uniform droplets should yield less variation in terms of length. It can be anticipated that the NW nucleation is better synchronized in time in the case of the VLS growth in regular templates, which also contributes into the resulting size uniformity.

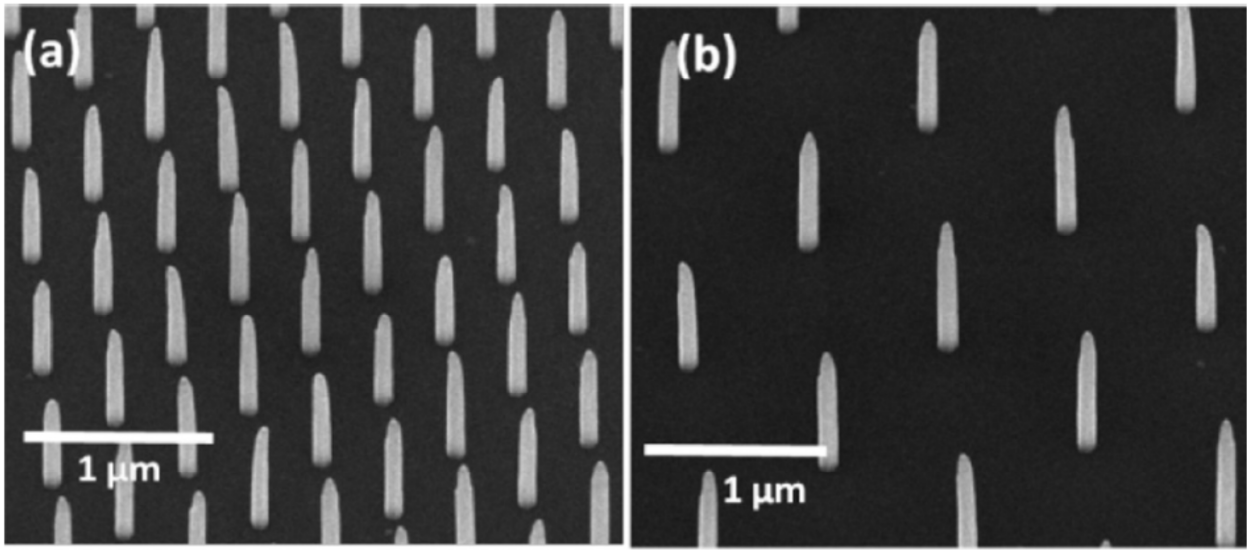

Figure 2.3. Tilted SEM images of regular two-dimensional (2D) arrays of InP/GaP core-shell NWs grown by MO-MBE from Au nanoparticles formed prior to epitaxy in the openings of a SiN_x mask, defined by electron-beam lithography. The pattern pitches are 0.5 and 1 µm in (a) and (b), respectively. Reprinted from Journal of Crystal Growth, vol. 463, N. N. Halder, A. Kelrich, Y. Kauffmann, S. Cohen and D. Ritter, Growth of wurtzite InP/GaP core-shell nanowires by metal-organic molecular beam epitaxy pp. 10-13, Copyright (2017), with permission from Elsevier.

Using Au as the VLS growth catalyst for III-V NWs is not desirable for integration with Si electronics, because Au can contaminate the NWs due to kinetic factors. Consequently, self-catalyzed (or self-assisted) VLS growth has emerged as a promising Au-free alternative, starting from the pioneering works by the group of Fontcuberta i Morral [22] and Jabeen et al. [23], and quickly adapted by other groups [23-32]. In this method, Au is replaced by the group III metal, that is, one of the NW constituents. Self-catalyzed VLS growth of III-V NWs allows one not

only to safely avoid the unwanted Au contamination, but also to achieve excellent phase purity [27] and high degree of size homogeneity within the NW ensembles in terms of both radius [28] and length [30,31]. It should be noted that the self-catalyzed growth of III-V NWs is more easily achieved in MBE. Chemical epitaxy techniques such as MOVPE, CBE or HVPE are less suited for the self-catalyzed approach, most probably due to the difficulty in maintaining Ga droplets under effectively group V rich conditions typically employed in these growth methods (see Ref. [32] and a discussion therein).

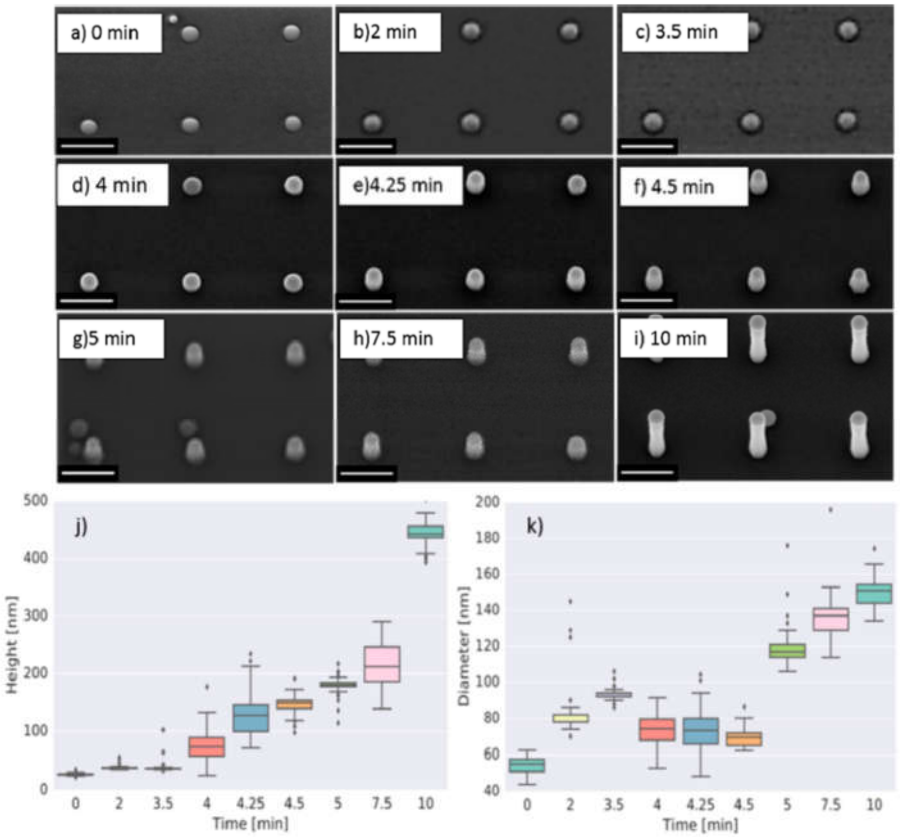

Figure 2.4. Time series of Ga-catalyzed GaAs NW arrays: (a-i) SEM images of the array grown for 0 min (just after the droplet deposition) up to 10 min. Scale bar is 200 nm, and the tilt angle is 20°; the corresponding height (j) and diameter (k) distributions obtained by AFM. The diameter decrease seen after 4 min of GaAs deposition is due to the shape change as the droplets are lifted from the substrate surface, after which the NWs start to grow radially. Reprinted from J. Vukajlovic-Plestina, W. Kim, V. G. Dubrovskii, G. Tütüncüoğlu, M. Lagier, H. Potts, M. Friedl and A. Fontcuberta i Morral, Engineering the size distributions of ordered GaAs nanowires on silicon, Nano Letters **17**, 4101-4108 (2017), https://pubs.acs.org/doi/10.1021/acs.nanolett.7b00842, with permission from the American Chemical Society, to which further permissions related to the material excerpted should be directed.

Figure 2.4 shows the initial stages of self-catalyzed GaAs NW growth in regular arrays on patterned Si [33]. MBE growth was performed on a Si(111) substrate covered with a 10 nm thick thermal oxide, in which nanoscale holes were etched with reactive ion etching. The yield of vertical NWs was higher than 85%. SEM images in Figures 2.4 (a) to (i) show the GaAs NW arrays obtained on 45 nm wide holes as a function of time. For this series of samples, the Ga flux corresponded to a GaAs planar growth rate of 0.1 nm/s, the As_4 beam equivalent pressure (BEP) was 2×10^{-6} Torr, and the substrate temperature was 635 °C. Morphological analysis [33] shows that the NWs elongate axially and extend radially, as shown in Figures 2.4 (j) and (k). Radial growth occurs due to effectively Ga-rich growth conditions, whereby more Ga atoms arrive to the droplet than used for NW growth [25]. As a consequence, the droplets inflate, first by increasing their contact angle and then by extending the radius of the NW top. Cylindrical geometry is maintained by the step flow growth on the NW sidewalls, following the radial extension of the tip. Very importantly, one can observe a long delay of the NW nucleation, about 4 min, and a wide spread of the nucleation times for different NWs, which explains the broad length distribution within the array. Minimizing the nucleation randomness is crucial for improving the length uniformity [30,31] as will be discussed in Section 8.

One of the most interesting features of self-catalyzed VLS growth is that the droplet serves as a non-stationary reservoir of a group III metal, which can either swell or shrink depending on the V/III flux ratio [25,28,34,35]. Indeed, Ga is always present in the droplet for crystallization of GaAs with the arriving As. Hence, the axial NW growth rate is determined by the As influx and temperature-dependent desorption. Then the droplet will swell under negative and shrink under positive V/III influx imbalance, depending on whether more or less As atoms arrive to the droplet compared to Ga, respectively. The Ga influx usually includes surface diffusion flux of Ga adatoms from the NW sidewalls to the droplet, which is radius-dependent and increases for smaller radii. This may result in an interesting self-equilibration effect for the NW radius [28,34]. The effect requires that the influx of As atoms from vapor (minus desorption) is larger

than that of Ga. The missing Ga is brought by surface diffusion along the sidewalls. This contribution scales with NW radius whereas Ga consumption (an As input) scales with its square. As a consequence, the droplet size, and consequently the radius of the NW top, will increase with time for thin NWs, and decrease with time for thick NWs. As a result, the NW radii will converge to a stationary value, corresponding to the stable growth at this constant radius. Therefore, the radius distribution of NWs will self-regulate to an almost delta-like function regardless of the initial size distribution of Ga droplets. Details of this process will be discussed in Section 7.

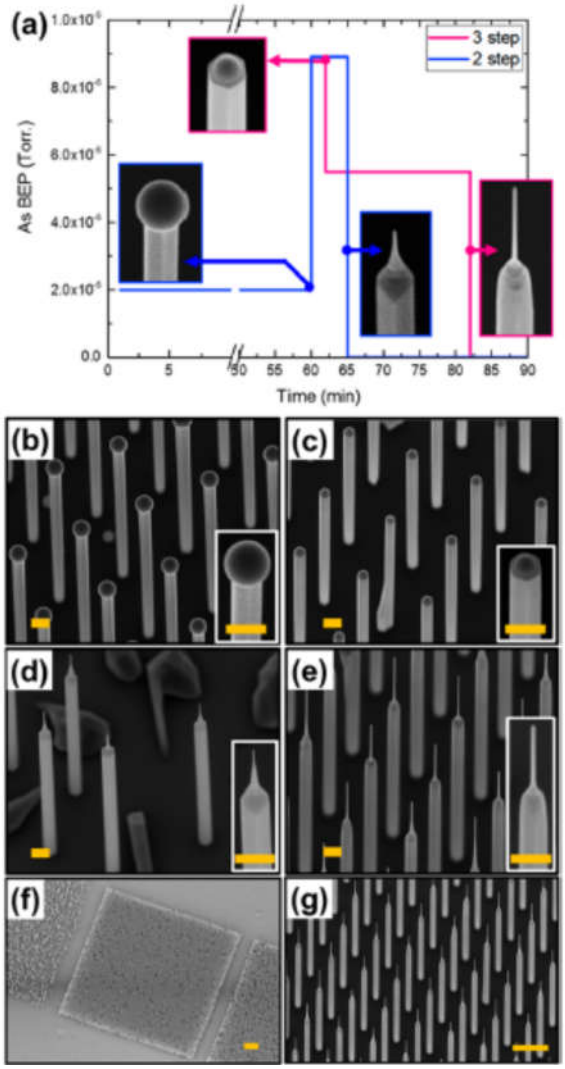

Figure 2.5. (a) Schematic morphology evolution of GaAs NWs and 20° tilted SEM images of 800 nm pitch arrays: (b) Standard growth under Ga-rich

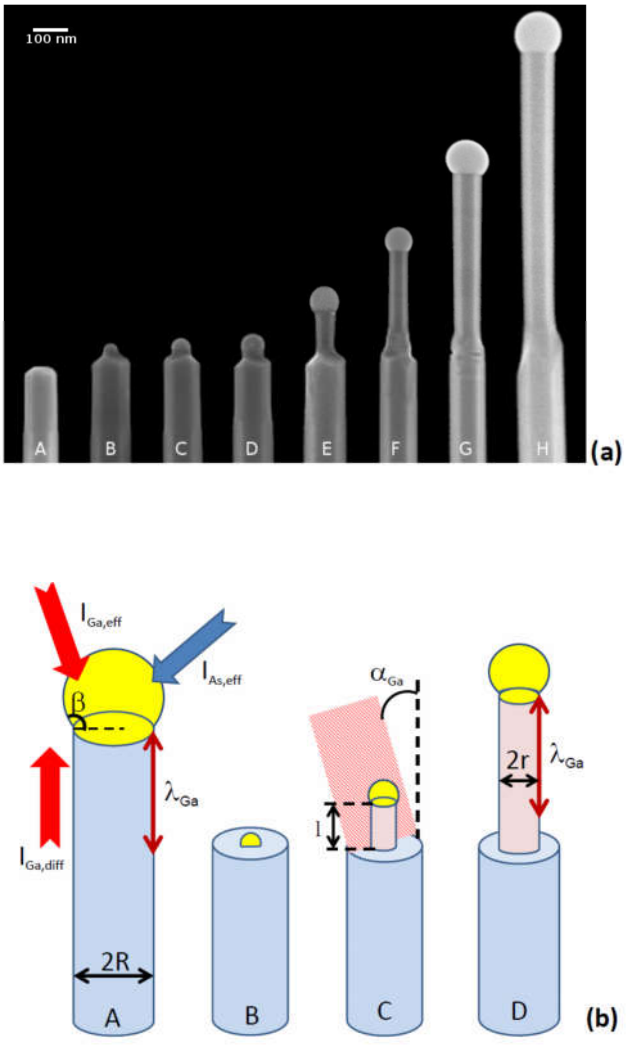

Figure 2.6. (a) Collage of SEM images of the GaAs NWs coming from different samples after the consumption of the Ga nanoparticle (A) and after

conditions at an As_4 BEP of 2×10^{-6} Torr; (c) Abrupt droplet shrinkage by increasing the As_4 BEP to 8.9 10^{-6} Torr for 2 min; (d) Further evolution of the tip under the same As_4 BEP, the tips are conically tapered and the droplets are finally lost; (e) Straight, 10 nm radius NNs on top of NWs obtained via the three-step procedure by decreasing the As_4 BEP to 5.5 10^{-6} Torr after step (c) and growing the NNs for 20 min. The inserts in (d) and (e) show the tapered tip without any droplet and straight NN with a droplet for higher and lower As_4 BEP, respectively. (f) and (g) Lower magnification SEM images of regular NNs on top of NWs. Scale bars are 200 nm in (b) to (e), 10 μm in (f) and 1 μm in (g). Reprinted from W. Kim, V. G. Dubrovskii, J. Vukajlovic-Plestina, G. Tütüncüoglu, L. Francaviglia, L. Güniat, H. Potts, M. Friedl, J.-B. Leran and A. Fontcuberta i Morral, Bistability of contact angle and its role in achieving quantum-thin self-assisted GaAs nanowires, Nano Letters **18**, 49-57 (2018), https://doi.org/10.1021/acs.nanolett.7b03126, with permission from the American Chemical Society, to which further permissions related to the material excerpted should be directed.

exposure to Ga and As beams for 30 s (B-D), 60 s (E), 150 s (F), 300 s (G) and 420 s (H). (b) Schematic of the NW growth process: Regular growth stage with the radius R increasing linearly with time due to a positive Ga imbalance arising from $I_{Ga,eff} + I_{Ga,diff} > I_{As,eff}$, with I_{eff} denoting the effective incoming fluxes of Ga and As (A); Nucleation of Ga droplet on a flat top facet of the primary NW (B); Fast radial growth of a short secondary NW (with the length l shorter than the diffusion length of Ga adatoms λ_{Ga}) due to additional diffusion flux of Ga from the top surface of the primary NW (C); Regular growth of a long secondary NW with $l > \lambda_{Ga}$ (D). Finally, the radius of secondary NW r will reach the radius of the stem R. Reprinted with permission from G. Priante, S. Ambrosini, V. G. Dubrovskii, A. Franciosi and S. Rubini, Stopping and resuming at will the growth of GaAs nanowires, Crystal Growth & Design **13**, 3976-3984 (2013). Copyright (2013) American Chemical Society.

The V/III influx imbalance can easily be regulated by the V/III flux ratio. This can be used for the fine tuning of the morphology of self-catalyzed III-V NWs. Figure 2.5 shows the example for Ga-catalyzed GaAs NWs grown in regular arrays on patterned SiO_2/Si(111) templates [35]. The initial step is the standard growth under negative V/III influx imbalance, achieved at a low As_4 BEP of 2×10^{-6} Torr for a fixed Ga flux corresponding to 0.11 nm/s planar growth rate of GaAs. All NWs grow radially in this step, reaching an average radius of 75 nm for 4 μm length. Now, the idea is to obtain quantum-thin nanoneedles (NNs) on top of this NWs by engineering the As flux. Increasing the As_4 BEP to 8.9×10^{-6} Torr for 2 min after the standard growth step yields to the structures shown in Figure 2.5 (c). Even though the Ga flux is still on,

the droplets have decreased to a radius smaller than that of the NW. Keeping these conditions for 3 min longer yields the formation of conical-like NN tops, as shown in Figure 2.5 (d). The top radius of conical-like NNs can be decreased to a very small size, about 5 nm. After that, the VLS growth should stop due to the consumption of Ga and NNs cannot grow any longer.

If, instead of maintaining the As_4 BEP at a constant value of 8.9×10^{-6} Torr in the droplet shrinking stage, it is decreased down to 5.5×10^{-6} Torr from the step shown in Figure 2.5 (c), the morphology changes dramatically. Figure 2.5 (e) shows a representative SEM image of the structures obtained after 20 min of growth at 5.5×10^{-6} Torr. It is clearly seen that introducing the third growth step with a lower As flux after shrinking the droplets results in the formation of thin NNs that first taper and then acquire a uniform radius of approximately 10 nm. This stationary radius stays constant along ~ 1 μm of the NN length. These structures show quantum confinement effect as discussed in detail in Ref. [35].

Figure 2.6 (a) shows the results of Ref. [25], where the Ga-catalyzed VLS growth of GaAs NWs was intentionally stopped and resumed by consuming Ga droplets under As flux and then nucleating a secondary NW. Primary GaAs NWs were fabricated by solid-source MBE on Si-treated GaAs(111)B substrates. The NW growth was carried out at 640°C with a V/III BEP ratio of 5. The Ga flux was set to a BEP of 3.6×10^{-7} Torr, corresponding to a growth rate of 0.28 nm/s on GaAs(100) surface. After 60 minutes of growth, the Ga shutter was closed and the sample was kept for 10 minutes under As flux to obtain the complete consumption of the droplet. After this step, the Ga shutter was opened again for different durations. NW A in Figure 2.6 (a) represents the starting point of the secondary growth step. After the complete consumption of the Ga droplet, the tip appears flat. After 30 s of exposure to Ga and As beams (NWs B, C and D) the morphology of the tip changes. A spherical cap droplet, with radius smaller than that of the NW, becomes visible. This droplet is now sitting on top of a pyramid-like structure, which morphology resembles that of NWs terminating with (110) facets. NWs B-D belong to the same sample, and the differences between them can be ascribed to local fluctuations of the effective

beam fluxes. After 60 s (NW E) a new NW portion has grown and the droplet has already reached its equilibrium geometry, with a contact angle exceeding 110°. For increased deposition times (NW F after 150 s and G after 300 s), the NW continues to elongate. NWs B to F show two diameter discontinuities along their bodies. The first related to the consumption of the droplet, as in A, and the second due to the growth resumption with smaller radius. By increasing the deposition time, the separation between the two discontinuities tends to decrease, and finally the secondary NW reaches the size of the primary one.

The model schematized in Figure 2.6 (b) and described in more detail in Ref. [25] is capable of explaining the observed trends, including (i) the linear length-time and radius-time dependences for the primary NWs; (ii) explanation of why Ga nanodroplet reappears on the NW top; and (iii) the non-linear radius-time dependence for the secondary NW, while the length-time correlation remains almost exactly identical to that at the regular growth stage.

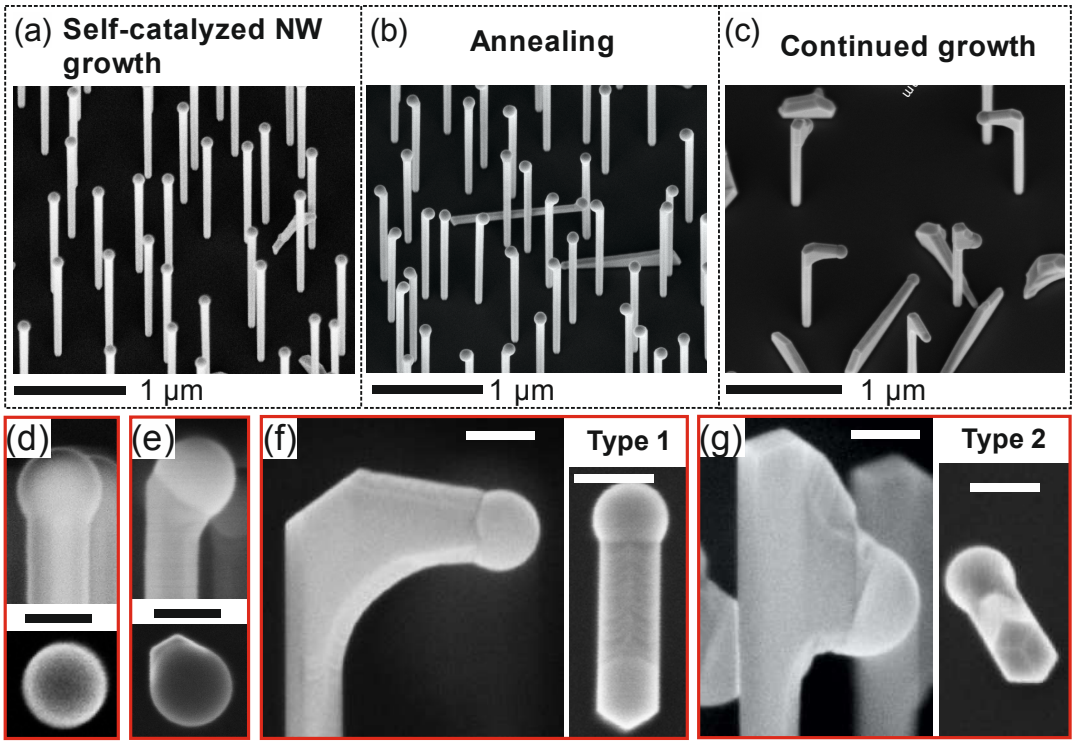

Figure 2.7. Growth of bent Ga-catalyzed GaAs NWs: (a) and (d) Vertical NWs grown for 20 min and rapidly cooled down; (b) and (e) NWs annealed at the growth temperature for 45 s prior to cool down; (c) NWs grown for 5 min after 45 s annealing; Side and top-view images of (f) type 1 horizontal and (g) type 2 downward growth. Scale bars in low magnification 30° tilted images are 1 µm in (a) to (c) and 100 nm in (d) to (g). Reprinted with permission from E. S. Koivusalo, T. V. Hakkarainen, H. V. A. Galeti, Y. G.

Gobato, V. G. Dubrovskii and M. D. Guina, Deterministic switching of the growth direction of self-catalyzed GaAs nanowires, Nano Letters **19**, 82-89 (2019). Copyright (2019) American Chemical Society.

Besides engineering the radius of vertical NWs, growth interruptions can be used for changing the NW growth direction. Controllable switching of the NW growth direction opens up new horizons in the bottom-up engineering of self-assembled nanostructures, for example, to fabricate interconnected nanowires used for quantum transport measurements. In Ref. [36], a robust and highly controllable method was proposed for deterministic switching of the growth direction of self-catalyzed GaAs NWs. The method is based on the modification of the droplet-NW interface in the annealing stage without any fluxes and subsequent growth in the horizontal direction by a twin-mediated mechanism with indications of a novel type of interface oscillations. By systematically optimizing the growth parameters, 100% yield of switching the NW growth direction from vertical to horizontal was achieved, and occurring in the same horizontal plane.

In brief, the initial self-catalyzed GaAs NWs were grown by solid source MBE on lithography-free oxide pattern templates fabricated on p-Si(111) substrates via droplet epitaxy, with remarkably narrow length distribution [30]. After growth of the vertical part, the NWs were annealed for 20 to 70 s at the growth temperature of 640 °C, without any fluxes in order to reshape the droplet-NW interface. After the annealing, the NW growth was resumed by simultaneously providing the Ga and As fluxes. A typical NW sample after 20 min of vertical growth and immediate cool down without any fluxes is shown in Figures 2.7 (a) and (d). It is clearly seen that the Ga droplets remain stationary on the NW tips just after growth. In contrast, the sample that was annealed for 45 s at the growth temperature prior to cool down [Figure 2.7 (b) and (e)] exhibits 100% yield of droplets falling toward one of the (110) side facets. When the growth is resumed after annealing by simultaneously opening the Ga shutter and As cracker, the NWs continue their growth perpendicular to their initial growth direction [type 1 NWs in Figures 2.7 (c) and (f)], or slightly downward [type 2 NWs in Figures 2.7 (c) and (g)]. The azimuthal

direction of the bent NW part is toward one of the <112> directions associated with the corners of the (110) sidewalls, in contrast to the droplet position after the annealing [see the insets in Figures 2.7 (e) to (g)].

It was found that horizontal type 1 NWs have a better crystal quality, exhibiting pure ZB structure throughout the whole NW, with a single twin plane extending along the horizontal section. For type 2 NWs, the downward section is dominated by periodic twinning. Therefore, the yield of type 1 horizontal NWs was carefully optimized by the growth parameter tuning, and reached 100% for smaller diameters of the initial NWs (75 nm), higher number density (2.5×10^8 cm^{-2}), or longer annealing times (70 s).

3. Basics of the nanowire growth modeling

These examples demonstrate almost unlimited possibilities for bottom-up design of III-V NWs. Let us now discuss the most important ingredients of the NW growth modeling, leaving the details for the next sections. We start from the kinetic equations describing the time evolution of the total number of group V (N_5) and III (N_3) atoms in a catalyst droplet with base radius R, which equals the radius of the NW top [37]

$$\frac{dN_5}{dt}=\chi_5 I_5(1+\alpha_r)\pi R^2-I_5^{des}\frac{2}{(1+\cos\beta)}\pi R^2-\frac{\pi R^2}{\Omega_S}\frac{dL}{dt}, \tag{3.1}$$

$$\frac{dN_3}{dt}=\chi_3 I_3\pi R^2+j_{3,diff}-\frac{\pi R^2}{\Omega_S}\frac{dL}{dt}. \tag{3.2}$$

Equation (3.1) accounts for (i) the direct (I_5) and re-emitted ($\alpha_r I_5$) atomic fluxes of group V atoms [26] which are entering the droplet seated on the NW top, with χ_5 accounting for the beam geometry and the droplet contact angle in MBE [38] or the precursor cracking efficiency in MOVPE (with $\chi_5=2/(1+\cos\beta)$ for 100% cracking), (ii) the desorption flux I_5^{des} from the surface area of spherical cap droplet with the contact angle β, and (iii) the sink of group V atoms

due to the NW elongation dL/dt, with Ω_S as the elementary volume per III-V pair in solid. We neglect surface diffusion of group V species due to their high volatility. The influx of group III atoms in Eq. (3.2) is the sum of the impinging flux $\chi_3 I_3$ (with the same meaning of the parameters as for group V), and the net diffusion current through the triple phase line (TPL) of cylindrical NW (in s^{-1}). The latter is given by $j_{3,diff} = -2\pi R D_3 (\partial n_3 / \partial z)\big|_{z=L}$, with D_3 as the diffusion coefficient of group III adatoms on the sidewalls, and n_3 as their surface concentration as a function of the height z. Desorption of group III atoms from the droplet is neglected. The sink due to NW growth should be exactly the same as for group V atoms to ensure stoichiometric III-V compound in the solid NW.

In the Au-catalyzed case under group V rich conditions, the excess group V atoms will desorb from the droplet. The axial NW growth rate is then obtained from the condition $dN_3/dt = 0$, in which case Eq. (3.2) yields

$$\frac{dL}{dt} = \chi_3 \Omega_{35} I_3 + \frac{\Omega_S j_{3,diff}}{\pi R^2}. \tag{3.3}$$

The diffusion flux $j_{3,diff}$ should depend on chemical potentials of group III atoms in the droplet (μ_3^L) and group III adatoms on the NW sidewalls at large enough distance from the droplet, and may be sensitive to the vapor flux of As atoms and their concentration in the droplet. The simplest approximation $j_3 = 2\pi R \varphi_3 \lambda_3 I_3$ (where φ_3 summarizes the geometrical effect in MBE or the cracking efficiency at the NW sidewalls in MOVPE and the collection length of Ga atoms λ_3 can depend on the group V flux) leads to the typical inverse radius dependence of the NW axial growth rate [5,11,37]

$$\frac{dL}{dt} = \Omega_S I_3 \left[\chi_3 + \varphi_3 \frac{2\lambda_3}{R} \right]. \tag{3.4}$$

In this transport-limited regime, the NW elongation is independent of the droplet composition. Similar equation is often used to describe the length-radius correlation of elemental semiconductor NWs such as Si [39].

For self-catalyzed VLS growth, or Au-catalyzed VLS growth under As-poor conditions (where the Ga fraction in liquid approaches unity), the axial growth rate is limited by the kinetics of group V species, while dN_3/dt is non-zero as discussed above. Putting $dN_5/dt = 0$ in Eq. (3.1), we obtain

$$\frac{dL}{dt} = \chi_5 \Omega_S I_5 (1+\alpha_r) - \frac{2}{1+\cos\beta}\Omega_S I_5^{des}. \tag{3.5}$$

However, this equation is not self-consistent because the desorption rate depends on the atomic concentration of group V atoms in the droplet c_5 (here and below, we use the normalization for c_X with $X = 3$, 5, Au such that $c_3 + c_5 + c_{Au} = 1$, which is reduced to $c_3 + c_5 = 1$ for self-catalyzed NWs). According to Refs. [40,41], if group V species desorb in the form of dimers, we have

$$I_5^{des} = I_{5,0}\exp(2\bar{\mu}_5^L), \tag{3.6}$$

where $\bar{\mu}_5^L = \mu_5^L/(k_B T)$ is the chemical potential of group V atoms in liquid in thermal units, T is temperature and k_B is the Boltzmann constant. The temperature-dependent pre-exponent $I_{5,0}$ is related to the vapor phase. Finding c_5 requires a second equation for dL/dt, which is determined by the crystallization rate at the liquid-solid interface under the droplet [40,41].

Theoretical considerations [42-46] and *in situ* growth monitoring inside a transmission electron microscope (TEM) [47-49] suggest that NWs often grow in the so-called mononuclear regime whereby only one 2D island succeeds in nucleating for each NW monolayer (ML). The probability to nucleate a 2D island on the top facet of cylindrical NW of radius R per unit time equals $\pi R^2 J$, where J is the nucleation rate. On the other hand, the island fills the complete ML slice of a NW after the time period R/v, where $v = dr/dt$ is the growth rate of a linear size of the island. The ratio of these characteristic times naturally yields the control parameter $\pi R^3 J/v$

[43]. Mononuclear growth occurs at $\pi R^3 J / v << 1$, which requires small NW radii, slow nucleation rates and rapid island growth rates. Similar considerations apply when nucleation of 2D islands takes place at the TPL rather than on the whole top facet, as has been proposed [40] to explain polytypism in NWs (see section 10.2), in which case the nucleation probability equals $2\pi R r_c J$, with r_c as the radius of the critical 2D island [41,42].

Slow nucleation rates correspond to low chemical potentials of III-V pairs in the liquid with respect to the reference solid state, defined as [14]

$$\Delta\mu(c_3, c_5, T) = \mu_3^L(c_3, c_5, T) + \mu_5^L(c_3, c_5, T) - \mu_{35}^S(T) . \tag{3.7}$$

Here, the μ_X^L are the chemical potentials of group III and V atoms in liquid, which depend on the two atomic concentrations c_3, c_5 and temperature T, and μ_{35}^S is the temperature-dependent chemical potential per III-V in solid. The number of III-V pairs in the critical 2D island (the critical size for brevity) is given by the standard equation of classical nucleat

ion theory (CNT) [6]

$$i_c = \frac{a^2}{4\Delta\bar{\mu}^2} , \tag{3.8}$$

with $\Delta\bar{\mu} = \Delta\mu/(k_B T)$ the chemical potential in thermal units. The energetic constant a is proportional to the effective surface (or edge) energy of 2D island γ_{eff}. For regular triangle shape of the island, it is given by [7]

$$a = 2 \times 3^{3/4} \frac{\gamma_{eff}}{k_B T} (\Omega_S h)^{1/2} , \tag{3.9}$$

with h the ML height. Using CNT requires that the critical size is macroscopic ($i_c >> 1$). In the mononuclear growth regime, the axial NW growth rate equals

$$\frac{dL}{dt} = \eta \pi R^2 h J , \tag{3.10}$$

with η = 1 for the center and $\eta = 2r_c / R$ for the TPL nucleation.

The Zeldovich nucleation rate of CNT was studied in Ref. [40] for self-catalyzed and in Ref. [50] for Au-catalyzed III-V NWs. It was argued that the island formation energy $F(i)$ should include the so-called self-consistency renormalization to ensure that $F(i)$ equals zero for the island of size one [51]. The details of calculations can be found in Ref. [50]. The resulting expression in the Au-catalyzed case has the form [50]

$$J = \frac{3^{3/4}}{\sqrt{\pi}} D_5 \left(\frac{h}{\Omega_S} \right)^2 e^{\bar{\mu}_{35}^S} c_5 \Delta\bar{\mu}^{1/2} \exp\left(a - \frac{a^2}{4\Delta\bar{\mu}} \right). \tag{3.11}$$

Here, D_5 is the diffusion coefficient of group V atoms in liquid, and $\bar{\mu}_{35}^S = \mu_{35}^S/(k_B T)$. This expression is consistent with the earlier result of Ref. [40] for self-catalyzed III-V NWs

$$J = J_0 c_5 \Delta\bar{\mu}^{1/2} \exp\left(-\frac{a^2}{4\Delta\bar{\mu}} \right), \tag{3.12}$$

with

$$J_0 = \frac{3^{3/4}}{\sqrt{\pi}} D_5 \left(\frac{h}{\Omega_S} \right)^2 e^{\bar{\mu}_{35}^S + a}. \tag{3.13}$$

For a Ga droplet, the surface energy and the diffusion coefficient of group V atoms in liquid Ga depend only on temperature. Therefore, the J_0 coefficient may depend on temperature but neither on $\Delta\mu$ nor c_5. According to Ref. [40], the values of the two unknowns J_0 and γ_{eff} [related to a in Eq. (3.12) through Eq. (3.9)] for Ga-catalyzed GaAs NWs equal 7 $nm^{-2}s^{-1}$ and 0.123 $J \times m^{-2}$, respectively, and can be taken independent of temperature within the range of 570-630 ^oC. Diffusion coefficient of As in liquid Ga is estimated at $D_{As} \cong 2 \times 10^{12}$ m^2s^{-1} for this temperature range [50].

When the critical size i_c approaches one III-V pair, CNT is no longer valid [6]. Small $i_c \sim 1$ correspond to high chemical potentials (or supersaturations) of the liquid phase and consequently rapid NW growth rates. This situation may occur in MOVPE and HVPE growth techniques at high material inputs, particularly for group V species. For $i_c \cong 1$, growth of 2D

islands becomes regular (or irreversible), meaning that meeting of any group III and V atoms at the liquid-solid growth interface immediately produces a stable III-V pair. The corresponding nucleation rate is then proportional to $c_3 c_5$. The axial growth rate in this case is given by [51-53]

$$\frac{dL}{dt} = K_{35} c_3 c_5 , \tag{3.14}$$

with K_{35} as the crystallization rate in $\mathrm{nm} \times \mathrm{s}^{-1}$. Obviously, regular growth is enabled on the entire surface of the top facet. In the regular growth picture, it is reasonable to take the desorption rate in the form

$$I_5^{des} = k_5^{des} c_5^2 , \tag{3.15}$$

with a certain temperature-dependent pre-exponent k_5^{des}.

Equations (3.10), (3.11) for $i_c >> 1$ or Eq. (3.14) for $i_c \cong 1$ together with Eqs. (3.1) and (3.2) and the corresponding desorption rates constitute the closed system which allows for the self-consistent determination of all the unknowns entering the equations, namely, the steady-state values of c_3, c_5 and dL/dt in the Au-catalyzed case, or c_5 and dL/dt in the self-catalyzed case. Non-stationary equation for dN_3/dt is separated from the axial growth rate in the latter case and describes the time evolution of the Ga droplet size. The full self-consistency requires determination of (i) chemical potentials as functions of the concentration(s) and temperature, (ii) desorption rate of group V atoms from the droplet, and (iii) diffusion flux of group V atoms into the droplet. This will be discussed in Section 6. Furthermore, relating N_X to c_X and β to c_3 by simple geometrical expressions enables one to treat interesting not-stationary problems such as formation of axial NW heterostructures in ternary III-V NWs [53, 54], or evolution of the droplet volume under time-dependent fluxes [55].

4. Role of surface energy

Nebol'sin and Shchetinin [56] presented a model for the surface energetics of VLS NWs, in which a stable contact angle of the droplet was introduced related to stable growth of NWs with vertical sidewalls. The model enabled a simple classification of the catalyst metals suitable for the VLS growth of Si NWs [56]. The surface energy criteria were later reconsidered by Tersoff *et al*. [47,48,57] and Dubrovskii [58] and turned out to have an important impact on the droplet stability issues [35,59], NW morphologies [57, 58], and related crystal phases of III-V NWs [48,60,61]. In particular, *in situ* monitoring of the VLS growth of GaAs NWs [48,61] reveal the occurrence of a truncated corner facet at the growth interface at large enough contact angles of the droplet. The amount of truncation oscillates with the period of ML formation. The presence or absence of the truncation is related to the crystal phase of III-V NWs [47,48,61], which can be either cubic ZB or hexagonal wurtzite (WZ). Morphology of the growth interface has an interesting connection with the Glas theory of polytypism of VLS III-V NWs [42]. All these factors show the importance of the surface energy constrains in the VLS growth of NWs.

Possible geometries of the VLS growth interface are shown in Figure 4.1. The NWs can form in (i) inward tapered geometry with non-wetted (N-W) narrowing (n) facets making a positive angle θ_n with respect to vertical [Figure 4.1 (a)]; (ii) outward tapered geometry with non-wetted widening (w) facets inclined at a negative angle θ_w with respect to the vertical [Figure 4.1 (b)]; (iii) with truncated (tr) wetted (W) growth interface at an angle θ_{tr} with respect to the vertical, which can grow only to a finite length according to Ref. [47] [Figure 4.1 (c)]; or (iv) with non-wetted vertical facets and planar growth interface [Figure 4.1 (d)], which is the standard VLS configuration. The solid-vapor surface energies $\gamma_{SV}(\theta)$ depend on the crystal phase (ZB or WZ) [62,63], while the solid-liquid surface energies $\gamma_{SL}(\theta)$ are usually assumed phase-independent for any θ according to Ref. [42].

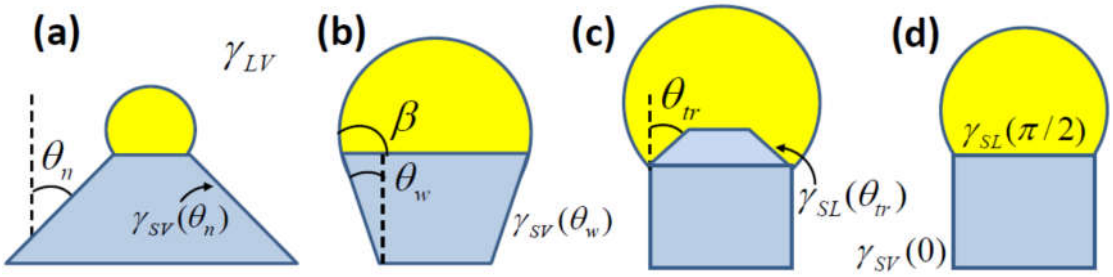

Figure 4.1. Non-wetted (a) narrowing and (b) widening facets, yielding an increasing or decreasing contact angle β, respectively. (c) Truncated wetted facet with the angle θ_{tr}, which will grow only to a finite length. Configurations (a) to (c) are compared to the standard VLS growth mode with planar liquid-solid interface and vertical side facets, shown in (d). Reprinted with permission from V. G. Dubrovskii, N. V. Sibirev, N. N. Halder and D. Ritter, Classification of the morphologies and related crystal phases of III–V nanowires based on the surface energy analysis, Journal of Chemical Physics C **123**, 18693-18701 (2019). Copyright (2019) American Chemical Society.

Using the results of Ref. [58], the excess surface energy (per unit area) of forming NWs with non-wetted facet at the angle θ to the vertical with respect to the standard non-wetted vertical facet in the ZB phase is given by

$$\Delta\Gamma_{N-W} = \frac{\gamma_{SV}(\theta)}{\cos\theta} - \gamma_{SV}(0) - [\gamma_{SL}(\pi/2) + \gamma_{LV}\cos\beta)]\tan\theta\,. \qquad (4.1)$$

Here, $\theta = \theta_n > 0$ for narrowing or $\theta_w < 0$ for widening facet. The excess surface energy of forming NWs with truncated wetted facet with the angle θ_{tr} equals

$$\Delta\Gamma_W = \frac{\gamma_{SL}(\theta_{tr})}{\cos\theta_{tr}} - \gamma_{SV}(0) - \gamma_{SL}(\pi/2)\tan\theta_{tr} + \gamma_{LV}\sin\beta\,. \qquad (4.2)$$

We note that these expressions are actually insensitive to whether the VLS growth is considered as instantaneous adding of MLs or at a constant volume of the catalyst droplet [58].

The preferred morphology is now determined by the minimum $\Delta\Gamma$ at a given contact angle β, where the zero level corresponds to the vertical sidewalls and planar liquid-solid interface in the ZB phase. Constructing the structural diagrams for different contact angles requires knowing the types of different facets and their surface energies. Below we consider the best known case of GaAs NWs. The widening facet should be the low energy (111)B facet in the

ZB phase, with θ_w=-19.5^o. The narrowing facet is the (110) ZB facet according to the *in situ* data of Ref. [61] (obtained for Ga-catalyzed GaAs NWs), with $\theta_n = 54.7^o$. The wetted truncated facet makes the same angle to the vertical, with $\theta_{tr} = 54.7^o$. The lowest energy vertical facet in the WZ phase is the $(1\bar{1}00)$ facet, whose surface energy is lower than that of the (110) ZB vertical facet according to the calculations of Refs. [62,63]. This feature is essential for the WZ phase formation in III-V NWs (see, for example, Ref. [6] for a detailed review). The calculated surface energies of the solid-vapor facets are given in Table 4.1, along with the corresponding references. The droplet surface energy γ_{LV} should be close to that of pure liquid Ga. This is guaranteed for Ga-catalyzed growth and should also be the case for Au-catalyzed due to the lower surface energy of liquid Ga compared to Au. We take the Ga surface energy at 420^{o}C, corresponding to the growth temperature employed during *in situ* measurements [61]. However, the temperature dependence of the surface energy of liquid Ga is very week [65]. All these considerations show that the structural diagram for a given material should not be much affected by the catalyst type and temperature.

Table 4.1. Parameters of GaAs used for modeling the NW morphology

Parameter	$\gamma_{(111)B}$ (J/m^2)	$\gamma_{(110)}$ (J/m^2)	$\gamma_{(1\bar{1}00)}$ (J/m^2)	γ_{Ga} (J/m^2)	$\beta_{\min}$ (deg)	$\beta_{\max}$ (deg)	θ_w (deg)	$\theta_n = \theta_{tr}$ (deg)	$\gamma_{SL}(\pi/2)$ (J/m^2)	$\gamma_{SL}(\theta_{tr})$ (J/m^2)
Value	0.690	0.798	0.700	0.684	100	125	-19.5	54.7	0.593	0.566
Source	Calc. [64]	Calc. [62]	Calc. [62]	Calc. [65]	Exp. [61]	Exp. [61]	Assum.	Exp.	Fit	Fit

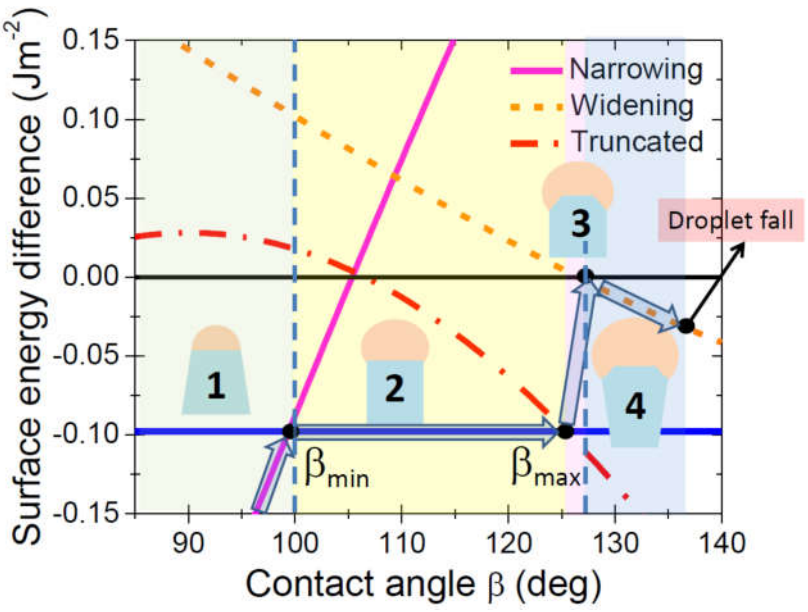

Figure 4.2. Structural diagram for VLS GaAs NWs, showing the energetically preferred morphology versus the contact angle of the droplet. Zero energy level corresponds to vertical (110) ZB side facets. Horizontal line at -0.098 Jm^2 corresponds to the negative surface energy difference between $(1\bar{1}00)$ WZ and (110) ZB vertical facets. Structure 1 with tapered NW shape and planar liquid-solid interface is preferred at small contact angles < 100°. The stable contact angle $\beta_{min} \cong 100^o$ corresponds to the VLS growth with vertical sidewalls at high V/III flux ratios. Any decrease of the contact angle below this value will introduce the narrowing facet and vertical growth will be resumed. Therefore, contact angles smaller than β_{min} are possible only in the kinetic regime where the droplet volume is gradually decreasing. The crystal phase in zone 1 is cubic ZB. Structure 2, observed between $\beta_{min} \cong 100^o$ and $\beta_{max} \cong 125^o$, corresponds to the VLS growth with vertical sidewalls and planar liquid-solid interface, most probably in the WZ phase. Above β_{max}, the truncated corner facets are developed, growing to a finite length. The crystal phase of such NWs should be cubic ZB. There is a narrow range of contact angles, approximately between 125° and 127°, where the truncated top is followed by vertical (110) ZB sidewalls (structure 3). The contact angle of $\cong 127^o$ can be called the second stable angle for the VLS growth at low V/III flux ratios, because any further increase will be compensated by introduction of the widening facet. If the droplet volume keeps increasing under excessive Ga influx, like in Ga-catalyzed GaAs NWs grown under Ga-rich conditions, the top facet increases its radius. This leads to reverse tapered geometry (structure 4). Subsequent radial growth on the NW sidewalls may resume cylindrical geometry, with the uniform NW radius increasing with time. Further increase of the contact angle to ~ 137° (in the kinetic regime) leads to the droplet fall onto the NW sidewalls. The arrows show the transformation of morphology with increasing the contact angle. The increase of surface energy in transition from structure 2 to 3 is explained by the fact that the vertical part of the NW must follow the ZB phase, determined by the center nucleation on the top facet.

With the known angles θ_w, θ_n, θ_{tr}, and the surface energies γ_{SV} and γ_{LV}, Eqs. (4.1) and (4.2) contain two unknowns, the solid-liquid interface energies $\gamma_{SL}(\pi/2)$ and $\gamma_{SL}(\theta_{tr})$. These values can be deduced based on the results of *in situ* monitoring of Ga-catalyzed GaAs NWs [61]. These results were obtained under varying Ga and As fluxes, which resulted in different contact angles of Ga droplets. At small contact angles, typically below 100^o, the NW morphology was tapered and the liquid-solid interface was planar. This kinetic regime was achieved under high As and low Ga fluxes where the droplet volume was gradually diminishing. At intermediate contact angles, typically between 100^o and 125^o, stable NW growth was observed, with vertical facets and planar liquid-solid interface. At large contact angles, above 125^o the truncated wetted corner facets developed, oscillating with the period of ML growth and increasing their size toward larger β. Soon after the 125^o contact angle, the NWs became reverse tapered due to the droplet swelling. Very importantly, these changes of the morphology led to the crystal phase switching – the crystal phase was ZB for small ($\beta < 100^o$) and large $\beta > 125^o$) and WZ for the intermediate range of β. Fitting the two critical contact angles, $\beta_{\min} = 100^o$ and $\beta_{\max} = 125^o$ yields the structural diagram of VLS GaAs NWs shown in Figure 4.2. From the fits, deduce the plausible values of γ_{SL} =0.593 J/m^2 and $\gamma_{\theta_{tr}L}$ = 0.566 J/m^2, which appear close to each other. The entire set of the parameters for GaAs NWs is summarized in Table 4.1, where "Calc." stands for calculations, "Exp." for the *in situ* data of Ref. [61], "Assum." for the assumption, and "Fit" for the fits of the surface energy curves with the two critical contact angles corresponding to the morphological transformations.

The structural diagram shown in Figure 4.2 reveals the following general trends. There are two critical contact angles, $\beta_{\min} \cong 100^o$ and $\beta_{\max} \cong 125^o$, between which the droplet changes its volume under varying group V and III fluxes (or the V/III flux ratio) by changing its contact angle. Within this range, the NW sidewalls are vertical and the liquid-solid interface is planar. The crystal phase of such NWs is expected to be WZ (see further details in what follows). In the

narrow range of contact angles, between 125^{o} and 127^{o}, the NWs grow with vertical sidewalls and truncated wetted top, in the ZB crystal phase. The two stable contact angles of 100^{o} and 127^{o} correspond to the vertical VLS growth under high and low V/III flux ratios, respectively. Decreasing the contact angle below the first stable value of 100^{o} is possible only in the kinetic regime where the droplet volume rapidly shrinks, and leads to tapered NW geometry, planar growth interface and the ZB phase. Excessive supply of Ga, as in some Ga-catalyzed GaAs NWs, will yield the radial growth at the NW top. Increasing the contact angle even above 127^{o} in the kinetic regime leads to more reverse tapered NWs. Quite interestingly, the two stable angles deduced here (100^{o} and 127^{o}) are very close to the ones obtained in Ref. [35] from *ex situ* measurements (95^{o} and 130^{o}). The small stable angle in Ref. [35] corresponded to predominantly WZ and the large stable angle to pure ZB crystal phase, which is also consistent with the diagram in Figure 4.2. Overall, Figure 4.2 explains quite well the known prevalence of the WZ phase in the steady-state growth of Au-catalyzed GaAs NWs, because the ZB phase forms in a very narrow range of contact angles (structure 3), and predominantly ZB phase of Ga-catalyzed GaAs NWs with large contact angles and radial growth at the NW top (structures 3 and 4).

It should be noted that treatment of the crystal phase presented here are based entirely on the surface energetics of ZB or WZ NWs in different morphologies and ignore the influence of chemical potential on the crystal phase switching, which is very important in the Glas theory of polytypism [42]. In this simplified picture, the preferred crystal phase is controlled by the sole parameter, the droplet contact angle. While including the chemical potential considerations may refine the picture, the existence of the two critical contact angles for the crystal phase switching in GaAs NWs strongly suggests that phase transitions occur quite abruptly whenever allowed by surface energetics. In other words, chemical potential near the transition points quickly exceeds the energy of stacking fault, which is required for switching from the ZB to WZ phase [42,43,60], and do not significantly affect the critical contact angles for the transition. We anticipate that a similar growth picture is relevant for other III-V NWs, but with different contact

angles for the morphological transformations and the related crystal phase switching. These contact angles are entirely determined by the surface energies of the relevant facets. It would be very interesting to perform similar *in situ* growth experiments for other material systems in the future.

5. Selective area epitaxy of III-V nanowires

Selective area epitaxy (SAE) of III-V NWs, pursued by Fukui *et al*. [66,67] and other groups [68-73], is another Au-free alternative to the Au-catalyzed VLS growth method. SAE growth of III-V NWs works equally well in MOVPE and MBE techniques. In the true SAE mode with no group III droplets on the NW tops, vertical growth of NWs is directed by the arrays of lithographically defined holes, or pores on patterned substrates such as SiO_x/Si(111). To improve the vertical yield of NWs, a balanced V/III flux ratio should be employed in order to avoid the formation of too large group III droplets in the holes or irregular III-V crystallites [72]. However, the initial stage of the SAE growth of III-V NWs may have the self-catalyzed VLS nature [72,73], with group III droplets disappearing in a later stage due a reduced material supply of group III atoms by surface diffusion.

According to the experimental data [66-71], both length L and radius R of the SAE-grown NWs usually increase with time, while the radius of Au-catalyzed VLS III-V NWs is fixed by the initial size of the growth seed and stays constant under optimized conditions. Here, we present a model for the time evolution of the mean length and radius of SAE NWs versus the growth parameters [74]. In particular, we discussed why, after a short incubation stage, the NW length and radius often feature scaling power-law dependences on the growth time, with the power exponents related to the growth conditions, the NW length and the array pitch.

Consider the SAE growth from the group III and V atomic fluxes I_3 and I_5, arriving onto the top NW facet and its sidewalls with the efficiencies χ_3, χ_5 and $\chi_3^{'}$, $\chi_5^{'}$ respectively. Group III adatoms are able to migrate from the NW sidewalls to the top, with the corresponding net

diffusion flux j_3, as in Eq. (3.2). For highly volatile group V atoms such as As and P, we account for desorption in the form of dimers (As_2 or P_2). We use Eq. (3.14) for the growth rate on both top and side facets of the NW, and Eq. (3.15) for the desorption rates of group V species. For SAE growth, it is more natural to consider the surface concentrations of group III and V atoms on the NW top (n_3, n_5) and sidewalls ($n_3^{'}$, $n_5^{'}$), in nm^{-2}. Under the steady state conditions, we thus have

$$\chi_3 I_3 + \frac{j_3}{\pi R^2} = k_{35} n_3 n_5 \;\; \chi_5 I_5 = 2k_5 n_5^2 + k_{35} n_3 n_5; \tag{5.1}$$

$$\chi_3^{'} I_3 - \frac{j_3}{2\pi R L_*} = k_{35}^{'} n_3^{'} n_5^{'}, \; \chi_5^{'} I_5 = 2k_5^{'} (n_5^{'})^2 + k_{35}^{'} n_3^{'} n_5^{'}, \tag{5.2}$$

with k_5 and $k_5^{'}$ as the desorption rates of group V atoms from the NW top and sidewalls, and k_{35} and $k_{35}^{'}$ as the crystallization rates of III-V pairs on the NW top and sidewalls, respectively. The latter are measured in $nm^2 s^{-1}$, and related to K_{35} in Eq. (3.14) as $k_{35} = K_{35}\Omega_S / h^2$ due to $n_X = c_X h / \Omega_S$ for $X = 3, 5$.

The net diffusion current arriving to the top should be divided by the surface area of the top facet πR^2 to give the diffusion-induced contribution into the adatom surface concentration. The same flux should be divided by the collection area $2\pi R L_*$ to describe the corresponding decrease in the surface concentration of the group III adatoms on the NW sidewalls. The collection length for group III adatoms can equal either the entire NW length L or only the effective diffusion length λ_3 at the NW top [6,7]. In the directional deposition techniques such as MBE, this λ_3 can be limited by the shadowing effect [75], with $\lambda_3 \cong P \cot an \alpha_3$ related to the inter-wire spacing (pitch) P and the angle α_3 of the group III beam with respect to the vertical. Therefore, the expression

$$L_* = \min\{L, \lambda_3\} \tag{5.3}$$

can be used in the first approximation. Then the axial and radial NW growth are given by

$$\frac{dL}{dt} = \Omega_S k_{35} n_3 n_5 ; \quad \frac{dR}{dt} = \frac{L_*}{L} \Omega_S k_{35}^{'} n_3^{'} n_5^{'}, \tag{5.4}$$

In the equation for the radial growth rate, the L_* / L factor accounts for the fact that crystallization of III-V pairs occurs only at the NW areas exposed to the vapor fluxes but contributes into the radial growth of the entire NW (under the assumption of cylindrical NW having a uniform radius from base to top at any moment of time).

Kinetic equations (5.1), (5.2) and (5.4) should be valid for the SAE NW growth under rather general conditions. In Ref. [74], two additional simplifications were used. First, it was assumed that the SAE growth proceeds under group V rich conditions – otherwise, it would quickly transition to a self-catalyzed mode with a group III droplet appearing on the NW top [73]. Then, much more group V atoms should desorb than crystallize in solid, corresponding to negligible desorption terms in Eqs. (5.1) and (5.2) for group V atoms. Second, the diffusion current j_3 should be presented as a function of n_3. In the absence of desorption of a group III element, the simplest approximation used in Ref. [74] writes

$$j_3 = 2\pi R L_* \chi_3^{'} I_3 (1 - \varepsilon_f). \tag{5.5}$$

Here, the most important parameter of the model

$$\varepsilon_f = \frac{\chi_3 I_3 \tau_5}{\chi_3^{'} I_3 \tau_5^{'}} = \frac{\chi_3 k_{35}^{'}}{\chi_3^{'} k_{35}} \left(\frac{\chi_5^{'} k_5}{\chi_5 k_5^{'}} \right)^{1/2} \tag{5.6}$$

is given by the ratio of the group III adatom activities on the NW top facet over the sidewalls.

Under these assumptions, Eqs. (5.1), (5.2) and (5.4) yield the kinetic equations for the axial and radial NW growth rates of the form

$$\frac{dL}{dt} = v_3 \left[\chi_3 + \chi_3^{'} \frac{2L_*}{R} (1 - \varepsilon_f) \right], \quad \frac{dR}{dt} = v_3 \chi_3^{'} \frac{L}{L_*} \varepsilon_f, \tag{5.7}$$

where $v_3 = \Omega_S I_3$ is the vapor flux of group III species in nm/s. This model should be relevant for sufficiently long NWs, while for shorter ones we should additionally account for a diffusion flux from the substrate surface [73]. While negligible for the growth on rough substrates with a

parasitic layer [76], this flux can be much more important in the case of atomically flat patterned SiO_x/Si(111) substrates, and essential for understanding of the growth start.

Equation (5.7) for dL/dt is similar to the conventional expression for the axial growth rate of VLS III-V NWs [5,11,41,65,76-80] or self-induced GaN NWs [81] under group V rich conditions. For small $\varepsilon_f << 1$, it gives the exponential elongation with time at $L < \lambda_3$, followed by the linear elongation at $L > \lambda_3$, and almost negligible radial growth. The smallness of ε_f for VLS NWs can be due to fast crystallization rate from liquid compared to the VS crystallization rate on the NW sidewalls ($k_{35} >> k_{35}^{'}$), slower desorption of group V atoms from liquid compared to the NW sidewalls ($k_5 << k_5^{'}$) or their better adsorption at the liquid surface ($\chi_5 >> \chi_5^{'}$). The ε_f values for the SAE NWs are expected to be larger, and highly dependent on the material composition. This explains, for example, why InSb NWs grown on InAs stems become nano-discs at high Sb fluxes [71], that is, grow faster in radius than in length.

Solutions to Eqs. (5.7) for short NWs ($L < \lambda_3$) are given by

$$L = (L_0 + R_c)\left(1 + \frac{t}{t_0}\right)^a - R_c\left(1 + \frac{t}{t_0}\right), \quad R = R_0\left(1 + \frac{t}{t_0}\right), \tag{5.8}$$

with $a = 2(1-\varepsilon_f)/\varepsilon_f$, $R_c = R_0\chi_3/[\varepsilon_f(a-1)\chi_3^{'}]$, $t_0 = R_0/(\varepsilon v_3 \chi_3^{'})$, and R_0, L_0 as the initial NW radius and length at $t = 0$, respectively. For long NWs ($L \geq \lambda_3$), the solutions change to

$$L \cong \lambda_3\left(1 + \frac{t - t_*}{t_1}\right)^{\frac{a}{a+1}}, \; R = R_*\left(1 + \frac{t - t_*}{t_1}\right)^{\frac{1}{a+1}}, \tag{5.9}$$

with $t_1 = R_*/[(2-\varepsilon_f)v_3\chi_3^{'}]$ and R_* as the NW radius at the moment of time t_* where L becomes equal λ_3. With the known deposition rate v_3 and geometry (the χ coefficients and the pore radius R_0), these simple expressions are controlled by the single parameter ε_f. It determines the power exponents in the scaling power-law dependences of the length and radius on the growth time as well as the characteristic times t_0 and t_1 for the axial elongation and radial extension in different

stages. After an incubation stage, the NW radius evolves linearly with time as long as $L < \lambda_3$, while the length increases super-linearly for $\varepsilon_f < 2/3$, or $a > 1$. The limiting case of the highest $\varepsilon_{f,\max} = 2/3$, or the lowest $a_{\min} = 1$, corresponds to the linear time dependence of the NW length. At $L > \lambda_3$, both length and radius increase sub-linearly with time. At $\varepsilon_{f,\max} = 2/3$, the power exponent for both length and radius at $L > \lambda_3$ equals 1/2.

We now consider experimental data on the SAE InAs NWs grown by MBE in patterned arrays on SiO_2/Si(111) at 480 ^{o}C, with As-BEP fixed at 3.5×10^{-6} Torr, and In flux corresponding to 0.024 nm/s, in 18 nm deep pores with a fixed radius of 40 nm and variable pitches [69]. Figures 5.1 (a) and (b) show the time evolution of the NW length and diameter, respectively, for pitches varying from 250 nm to 3000 nm. In MBE technique, the collection length of In should be limited by shadowing, which is expected to be almost negligible for 3000 nm pitch. Therefore, these data points were fitted by Eqs. (5.8) at $L < \lambda_3$, yielding the linear time dependence of the NW diameter (with $R_0 = 24$ nm and $t_0 = 26$ min). This corresponds to the effective deposition rate on the NW sidewalls $\chi_3' v_3 \cong 1.45$ nm/min. As discussed in detail in Ref. [69], the axial NW growth rate is faster at the beginning of growth, which can be attributed to the additional collection of In from the oxide surface. Leaving aside this initial stage, Eq. (5.8) was used for the NW length starting from $L_0 = 170$ nm. The best fit to the length data for 3000 nm pitch shown in Figure 5.1 (a) is obtained with $R_c = 17.5$ nm and $a = 1.14$, corresponding to $\varepsilon_f =$ 0.637. This large ε_f value yields only a slight super-linearity of the length versus time. The data for smaller pitches clearly show sub-linear behavior of the NW length and diameter, both decreasing with decreasing the pitch. All sets of data for 250 to 1000 nm pitches are well fitted by Eqs. (5.9) at $L > \lambda_3$ if we assume that the In collection length decreases from ~ 1.85 μm for 1000 nm pitch to ~ 0.5 μm for 250 nm pitch. All the curves in Figs. 5.1 correspond to the same $\varepsilon_f = 0.637$, related to a fixed V/III flux ratio, with the characteristic times t_1 in the range from

24 to 76 nm/min. Overall, the model reproduces very well the data, explaining why the length and diameter are almost linear in time for the largest pitch and become more and more sub-linear for smaller pitches after the NW length exceeds the collection length of In.

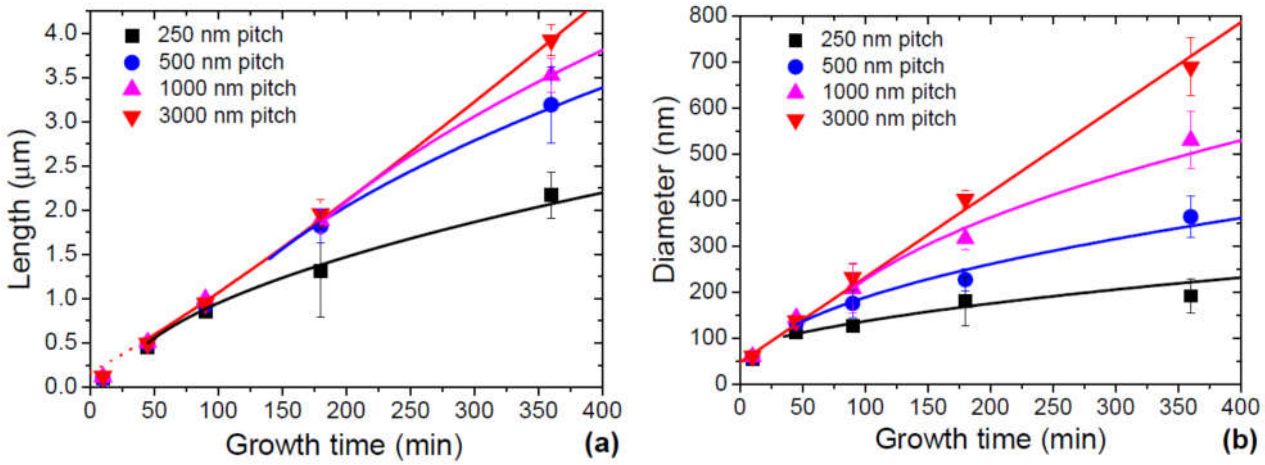

Figure 5.1. Time evolution of (a) length and (b) diameter of SAE InAs NWs grown by MBE in patterned arrays on SiO_x/Si(111) with different pitches from 250 to 3000 nm (symbols) [69], fitted by the model (lines). For the largest pitch of 3000 nm, the length evolution is slightly super-linear and the diameter is linear in time in the absence of shadowing. Decreasing the pitch leads to the decrease of the In collection length due to the shadowing effect, from more than 3500 nm for 3000 nm pitch down to 500 nm for 250 nm pitch. This leads to sub-linear behavior of both length and diameter after the NW length exceeds the collection length of In. Reprinted from V. G. Dubrovskii, Evolution of the length and radius of III-V nanowires grown by selective area epitaxy, ACS Omega **4**, 8400-8405 (2019), https://pubs.acs.org/doi/10.1021/acsomega.9b00525, with permission from the American Chemical Society, to which further permissions related to the material excerpted should be directed.

Next, we discuss the data of Ref. [70] for the length and diameter evolution of GaAs NWs grown by SAE MOVPE at 750 ^{o}C on patterned SiO_2/GaAs substrates, with a 600 nm pitch and variable pore diameter from 125 to 225 nm. These data show that the NW length first increases super-linearly with time, converging to a sub-linear behavior for longer times (Figure 5.2). This effect should be due to a limited diffusion length of Ga adatoms on the NW sidewalls. At a high temperature of 750 ^{o}C, a fraction of Ga adatoms desorb before reaching the NW top, corresponding to the transition from the growth regime at $L > \lambda_3$ to the one at $L < \lambda_3$. The pronounced super-linear increase of the NW length for shorter times requires sufficiently large a according to Eq. (5.8). The NW diameter in this stage is linear in time regardless of a. All

theoretical curves shown in Figure 5.2 correspond to a fixed $a = 1.83$, or $\varepsilon_f = 0.522$, at $L_0 = 0$. Other parameters are summarized in Table 5.1 and provide the excellent fits to all data. From the fits, we can deduce the values of $\chi_3' v_3 = 5.44$ nm/min and $\chi_3 / \chi_3' = 1.78$, showing that the adsorption of gallium is better on the top NW facet than on the sidewalls. The observed decrease of the NW length for larger pore size is explained simply by the fact that the NW elongation is controlled by surface diffusion of Ga, which contributes more into the axial growth rate of thinner NWs. The Ga diffusion length on the sidewalls appears very close to 2 μm in all cases.

Table 5.1. Parameters of GaAs NWs used for the fits in Figure 5.2

Pore size $2R_0$ (nm)	ε_f	R_c / R_0	t_0 (min)	t_1 (min)	t_* (min)
125	0.522	3.73	22	44	44
150	0.522	3.73	27	46	46.5
175	0.522	3.73	37	47	57.2
200	0.522	3.73	43	47	60
225	0.522	3.73	53.5	47	69

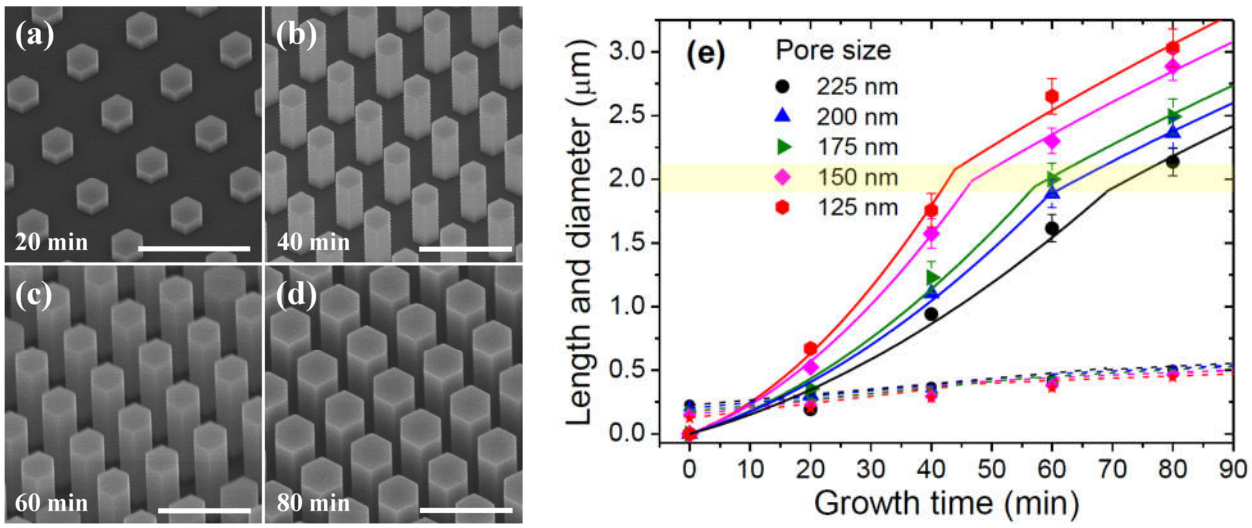

Figure 5.2. Length and diameter evolution of SAE GaAs NWs grown by MOVPE in patterned arrays on SiO_2/GaAs. SEM images in (a) to (d) show the time-dependent morphology of NWs after 20, 40, 60, and 80 min of growth, respectively, for a 600 nm pitch and 225 nm diameter pore array. All scale bars represent 1 μm. (e) Time-dependent mean length and diameter in the arrays with different pore sizes from 125 nm to 225 nm (symbols), fitted by the model (solid lines for the length and dashed lines for the diameter) with the parameters summarized in Table 5.1. Time dependence of the NW length converges

from super-linear to sub-linear at around 2 μm, corresponding to the diffusion length of Ga adatoms on the NW sidewalls (shown by the shaded zone). The NW diameters increase linearly before and slightly sub-linearly after 2 μm of length. The diffusion-like character of growth leads to the increase of length for thinner NWs. Reprinted from K. P. Bassett, P. K. Mohseni and X. Li, Evolution of GaAs nanowire geometry in selective area epitaxy, Applied Physics Letters **106**, 133102 (2015)., with the permission of AIP Publishing.

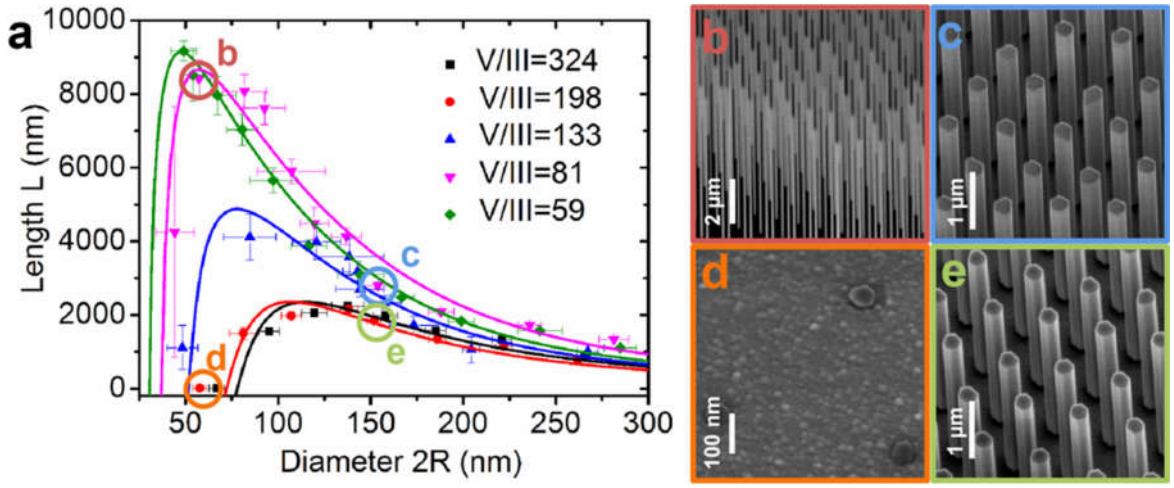

Figure 5.3. (a) Average NW length (after 5 min of growth time) of <111>A-oriented InP NWs grown by MOVPE in patterned arrays on SiO_x/InP(111)A substrates with variable pore size, as a function of their diameter under different V/III ratios obtained by varying only group V flow. Panels (b, c) and (d, e) show 30° tilted SEM images of the InP NWs grown with a V/III ratio of 81 and 198, respectively, as indicated in (a). The NW diameters are around 60 nm in (b), 150 nm in (c), 60 nm in (d), and 150 nm in (e). Lines in (a) are theoretical fits by the model. Reprinted with permission from Q. Gao, V. G. Dubrovskii, P. Caroff, J. Wong-Leung, L. Li, Y. Guo, L. Fu, H. H. Tan and C. Jagadish, Simultaneous selective-area and vapor-liquid-solid growth of InP nanowire arrays, Nano Letters **16**, 4361-4367 (2016). Copyright (2016) American Chemical Society.

In Ref. [73], it was shown that true SAE growth without droplets on top can coexist with the In-catalyzed VLS growth for InP NWs by MOVPE even in the same sample. The actual growth mode of NWs depends on the initial radius of the pores, V/III flow ratio and growth time. The VLS growth mode becomes more probable for thinner NWs (which start from smaller pores), lower V/III flow ratios and shorter times. In particular, Figure 5.3 shows the length-diameter correlation for InP NWs grown for 5 min with different V/III ratios, which can only be understood by considering simultaneous SAE and VLS growth. The growth rate of thin, 50-60 nm diameter NWs is tremendously enhanced by the presence of In droplet, forming

spontaneously at the tip due to surface diffusion of In. Medium diameter NWs evolve in a combined mode, with In droplets appearing and then disappearing in the course of growth. Only thick, ~ 150 nm diameter NWs grow in the true SAE mode from the very beginning. The coexistence of the VLS and SAE mechanism was also observed in Ref. [72] for InAs NWs grown by MBE in patterned arrays on SiOx/Si(111) substrates. It was found that most NWs start with In droplets that nucleated in the pores and disappeared in a later stage due to insufficient In supply from the oxide surface.

6. Growth kinetics of III-V nanowires

As already discussed in Section 3, the main kinetic processes governing the VLS growth of III-V NWs include (i) material transport of the group III and V species into the droplet by different kinetic pathways, including surface diffusion of group III atoms, (ii) desorption of group V atoms, and (iii) nucleation of 2D islands on the liquid-solid interface or at the TPL (at low supersaturations) or their regular crystallization (at high supersaturations). Here, we briefly discuss theoretical understanding and modeling methods for these processes achieved to this end.

6.1. Transport-limited nanowire growth

Models based on the mass transport equations do not consider 2D nucleation and hence are relevant in the case of Au-catalyzed VLS growth of III-V NWs under group V rich conditions, self-induced growth of GaN NWs or true SAE growth of III-V NWs. The axial NW growth rate in this case is limited by the mass transport of group III atoms into the droplet according to Eq. (3.3). Similar models can also be used for NWs of elemental semiconductors. The main problem is in finding the diffusion-induced contribution to the axial NW growth rate, given by

$$\left(\frac{dL}{dt}\right)_{diff} = -\frac{2\Omega_S}{R} D_f \left.\frac{dn_f}{dz}\right|_{z=L}. \qquad (6.1)$$

Here, subscript “f” is introduced instead of “3” in order to distinguish group III adatoms on the NW sidewalls (“f”) or on the substrate surface (“s”).

Diffusion-limited growth of NWs was considered in many original papers and reviews, for example, in Refs. [2,6,7,11,65,77-81]. The most general result is given by [78]

$$\frac{1}{V_3}\left(\frac{dL}{dt}\right)_{diff} = \frac{BU(L/\lambda_f)+C}{U'(L/\lambda_f)}, \tag{6.2}$$

where $V_3 \equiv I_3\Omega_S\cos\alpha_3$ is the 2D equivalent growth rate in MBE, α_3 is the angle of group III beam to the vertical, and λ_f is the diffusion length of group III adatoms on the NW sidewalls. The functions U and U' are defined as follows

$$U(L/\lambda_f) = \sinh\left(\frac{L}{\lambda_f}\right) + Q\delta\left(\frac{R}{\lambda_s}\right)\left[\cosh\left(\frac{L}{\lambda_f}\right)-1\right], \tag{6.3}$$

$$U'(L/\lambda_f) \equiv \frac{dU}{d(L/\lambda_f)} = \cosh\left(\frac{L}{\lambda_f}\right) + Q\delta\left(\frac{R}{\lambda_s}\right)\sinh\left(\frac{L}{\lambda_f}\right). \tag{6.4}$$

Here, $\delta(R/\lambda_s) = K_1(R/\lambda_s)/K_0(R/\lambda_s)$, with $K_m(x)$ as the modified Bessel functions of order m, R as the radius of the NW top, and λ_s as the diffusion length of group III adatoms on the substrate surface. The kinetic coefficients B and C stand for the diffusion fluxes into the droplet which originate from the NW sidewalls and the substrate, respectively

$$B = \frac{2\lambda_f\tan\alpha_3}{\pi R}(1-\varepsilon_f), \quad C = \frac{2\lambda_s}{R}\delta\left(\frac{R}{\lambda_s}\right)(1-\varepsilon_s). \tag{6.5}$$

The parameters ε_f and ε_s describe the differences between chemical potentials of group III atoms on the two surfaces and in liquid, similarly to Eq. (5.5):

$$\varepsilon_f = \exp\left(-\frac{\Delta\mu_{fl}}{k_BT}\right), \quad \varepsilon_s = \exp\left(-\frac{\Delta\mu_{sl}}{k_BT}\right). \tag{6.6}$$

Here, $\Delta\mu_{fl} = \mu_f - \mu_3^L$, $\Delta\mu_{sl} = \mu_s - \mu_3^L$ are the chemical potential differences for group III atoms on the surfaces (μ_f on the NW sidewalls and μ_s on the substrate) and in the liquid phase (μ_3^L). The coefficient Q in Eqs. (6.3) and (6.4) is given by

$$Q = \frac{\lambda_s}{\lambda_f}\frac{\varepsilon_s}{\varepsilon_f}\frac{\pi}{\tan\alpha_3}, \tag{6.7}$$

and does not contain chemical potential in liquid.

The total group III limited axial NW growth rate is obtained by summing up Eq. (6.2) with the flux originating from the direct impingement from vapor. If NWs grow on unpatterned substrates, we should subtract the 2D growth rate of parasitic layer between the NWs. Without desorption, all group III atoms deposited from vapor should be distributed in the parasitic layer and NWs. Then the final result for the axial growth rate takes the form [77]

$$\frac{1}{V_3}\frac{dL}{dt} = \left(A + \frac{BU(L/\lambda_f) + C}{U'(L/\lambda_f)}\right)\left(1 + \frac{R^2}{S_{NW}}\right) - 1, \tag{6.8}$$

with S_{NW} as the mean substrate area per NW (the reverse of the NW surface density). The vapor flux in the MBE case is given by

$$A = \frac{\chi_3(\alpha_3, \beta)}{\cos\alpha_3}, \tag{6.9}$$

where the geometrical function $\chi_3(\alpha_3, \pi/2) = (1 + \cos\alpha_3)/2$ at $\beta = \pi/2$, $\chi_3 = 1/\sin^2\beta$ when $\beta \geq \alpha_3 + \pi/2$, and has a more complex form for intermediate contact angles β [38]. Thus, the transport-limited elongation rate generally contains four unknown parameters: the two adatom diffusion lengths on the substrate surface and the NW sidewalls (λ_s and λ_f), and the two chemical potential differences between the surface and sidewall adatoms and group III atoms in liquid ($\Delta\mu_{sl}$ and $\Delta\mu_{fl}$).

The transport-limited growth model given by Eq. (6.8) was used for modeling the growth kinetics of a single $InP_{1-x}As_x$ NW with modulated composition in Ref. [77]. The NWs were

grown at 420°C by the Au-catalyzed MBE on InP (111)B substrates. These growth conditions produced NWs of WZ structure which grow in the [0001] direction without stacking faults, with a uniform diameter. A periodic modulation of the incident As_4:P_2 flux ratio was achieved by using non-uniformity of the fluxes on the substrate area. The $InP_{1-x}As_x$ NWs were removed from their substrate and imaged by high angle annular dark field scanning TEM (HAADF STEM). The image of a NW segment of 45 nm diameter is presented in Figure 6.1. The modulation of the HAADF intensity profile integrated over the whole diameter is superimposed [Figure 6.1 (a)]. The FFT-filtered HAADF image with the corresponding intensity profile is shown in Figure 6.1 (b). The oscillation amplitude is about 0.7% of the total HAADF intensity. The corresponding variation Δx of the As concentration x was determined to be about 0.03 around the mean value of 0.66. Such a small variation of composition is not expected to influence the NW elongation.

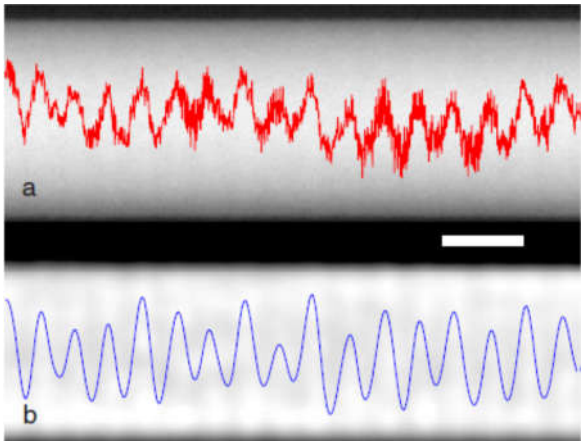

Figure 6.1. (a) HAADF STEM image of an $InP_{1-x}As_x$ NW segment grown with a modulated As_4:P_2 flux ratio. Scale bar represents 20 nm. The HAADF signal is integrated over the whole diameter and the profile is plotted along the growth axis. (b) FFT-filtered HAADF image and corresponding profile. Reprinted with permission from J. C. Harmand, F. Glas and G. Patriarche, Physical Review B **81**, 235436 (2010), https://doi.org/10.1103/PhysRevB.81.235436. Copyright (2010) by the American Physical Society.

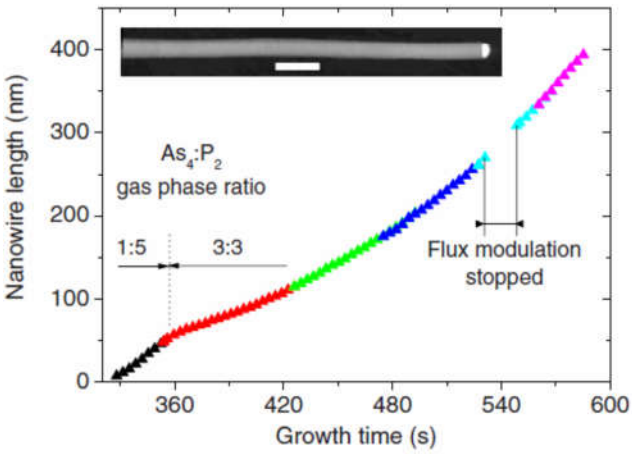

Figure 6.2. Growth chronology of a single $InP_{1-x}As_x$ NW. The length of the NW shown in the inset (Scale bar is 50 nm), is plotted as a function of time, as deduced from the composition oscillations along its axis. The different colors correspond to overlapping HAADF images. During growth, the flux modulation was stopped for 12 time periods. The corresponding region serves as a time reference. At 355 s, the nominal As_4:P_2 flux ratio was changed abruptly from 1:5 to 3:3. Reprinted with permission from J. C. Harmand, F. Glas and G. Patriarche, Physical Review B **81**, 235436 (2010),

The distance between any two concentration extrema equals the increase of the NW length during one time period. Therefore, it is straightforward to determine the instantaneous growth rate at each oscillation. This procedure was applied to a 21 nm diameter NW. The dependence with time of the NW length counted from the cleaved end is shown in Figure 6.2. The measured NW length clearly displays a nonlinear behavior with time. In this growth experiment, the flux modulation was stopped for 12 time periods. The corresponding region without compositional modulation, indicated in Figure 6.2, may serve as a time reference. At some point during growth, the nominal As_4:P_2 ratio was changed abruptly from 1:5 to 3:3, while the total average group V flux was kept constant. Thanks to the former time reference, this event can be accurately dated, as shown in Figure 6.2. The impact of this large change of flux ratio is strong and immediate - as seen from the change of the slope in Figure 6.2, the growth rate was suddenly reduced by a factor of 2.

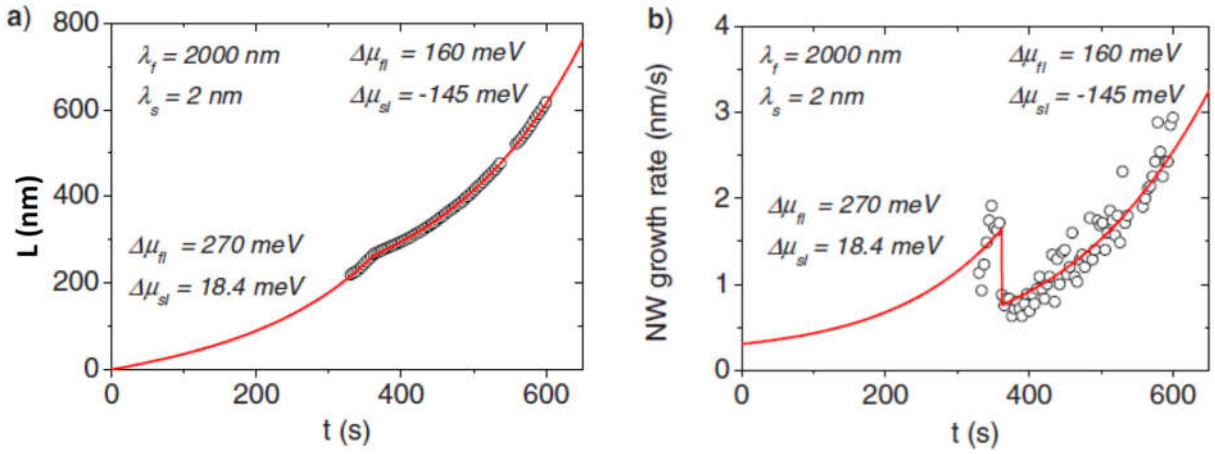

Figure 6.3. (a) Experimental NW elongation and (b) axial growth rate (circles), fitted with the diffusion transport model with the four parameters shown in the legends. Different chemical potentials are used for each As_4:P_2 ratio, before and after t=355 s. Reprinted figure with permission from J. C. Harmand, F. Glas and G. Patriarche, Physical Review B **81**, 235436 (2010), https://doi.org/10.1103/PhysRevB.81.235436. Copyright (2010) by the American Physical Society.

The obtained length-time dependence was fitted by Eq. (6.8). The value of λ_f has little influence on the results, provided that it is larger than the final NW length. Therefore, it was chosen to be 2 μm. Concerning λ_s, it was found that very small values (a few nm) are necessary to fit the experiment. The best fit is obtained with λ_s = 2 nm. This very short length can be understood as a limitation of adatom diffusion by atomic steps of the rough parasitic layer. The abrupt change of As_4:P_2 flux ratio is expected to modify significantly the composition and chemical potential of the catalyst droplet. Accordingly, two sets of chemical potential differences were adjusted, valid before and after this change. The best fit for the first part of growth at As_4:P_2 flux ratio of 1:5 was obtained with $\Delta\mu_{fl}$=270 meV and $\Delta\mu_{sl}$=18.2 meV. The contribution from the substrate surface is very small due to the combination of low λ_s and moderate $\Delta\mu_{sl}$. Very quickly, the contribution from the sidewalls dominates largely. After the change of As_4:P_2 flux ratio to 3:3, $\Delta\mu_{fl}$ must be reduced to 160 meV, which indicates that the flow from the sidewalls to the droplet is less efficient when P_2 is replaced by As_4. At the same time, $\Delta\mu_{sl}$ takes a negative value of 145 meV, showing that a significant part of the atoms intercepted by the NW now migrates to the substrate surface. With these parameters, the diffusion transport model describes fairly well the experimental $L(t)$ dependence, as shown in Figure 6.3. For both As_4:P_2 flux ratios, NW length increases almost exponentially with time, because the diffusion-induced is proportional to the length at $\lambda_f >> L$.

As regards the length-radius dependences of different semiconductor NWs, they were measured and modeled by many authors (see Refs. [6] and [7] for a detailed review). The diffusion transport into the droplet given by the general Eq. (6.2) can be reduced to the inverse power law dependence on the NW radius and becomes independent of length in some important particular cases (see Ref. [7] for systematization of such growth modes). For thin NWs, the chemical potential of group III atoms in the catalyst droplet can be elevated by the Gibbs-Thomson effect due to the curvature of the droplet surface according to [65,82]

$$\mu_3^{eff} = \mu_3^L + \frac{2\gamma_{LV}\tilde{\Omega}_L \sin\beta}{R}. \tag{6.10}$$

Here, $\tilde{\Omega}_L$ is the elementary volume per group III atom in the liquid phase and $R_d = R/\sin\beta$ is the droplet radius, with R as the radius of the NW top. Using Eq. (6.6) for the adatoms contributing to the NW elongation in a given growth regime, we obtain

$$\frac{1}{V_3}\frac{dL}{dt} = A_* + \left(\frac{\Lambda_3}{R}\right)^p \left(1 - be^{R_{GT}/R}\right). \tag{6.11}$$

Here, A_* stands for the vapor flux and accounts for possible growth on the substrate surface. The $b = \exp[(\mu_3^L - \mu_a)/k_BT]$ is a radius-independent constant (with index "a" corresponding to sidewall or surface adatoms), Λ_3 is the effective diffusion length of group III adatoms and p is the growth index which typically ranges from ½ to 2. For example, $p=1$ corresponds to the collection of group III atoms from the top part of the NW as discussed above, and $p=2$ to the collection from the substrate surface. The characteristic Gibbs-Thomson radius is given by

$$R_{GT} = \frac{2\tilde{\Omega}_L\gamma_{LV}\sin\beta}{k_BT}, \tag{6.12}$$

and equals a few nanometers in the typical cases [65].

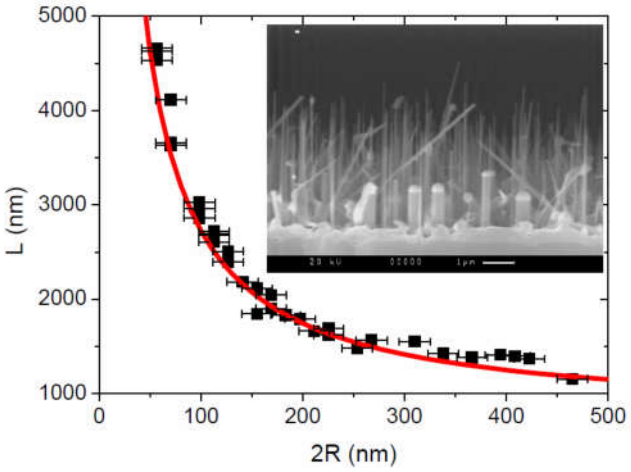

Figure 6.4. Length-diameter correlation of Au-catalyzed WZ GaAs NWs grown by MBE on a GaAs(111)B substrate at 585°C, with Ga flux

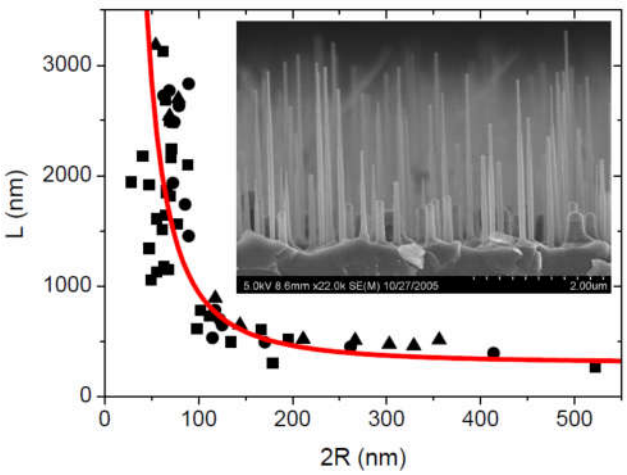

Figure 6.5. Length-diameter correlation of Au-catalyzed WZ GaAs NWs grown by MBE on a GaAs(111)B substrate at 560°C, with Ga flux

corresponding to 1 ML/s, and GaAs deposition thickness of 1000 nm (symbols). The insert shows a typical SEM image. The line shows the fit by $L = H(A_* + \Lambda_3 / R)$, with $A_* = 0.75$ and $\Lambda_3 = 100$ nm. Reprinted figure with permission from V. G. Dubrovskii, G. E. Cirlin, L. P. Soshnikov, A. A. Tonkikh, N. V. Sibirev, Yu. B Samsonenko and V. M. Ustinov, Physical Review B **71**, 205325 (2005), https://doi.org/10.1103/PhysRevB.71.205325. Copyright (2005) by the American Physical Society.

corresponding to 1 ML/s, and GaAs deposition thickness of 1000 nm (squares, dots, and triangles correspond to different parts of the same sample). The insert shows a typical SEM image. The line shows the fit by $L = H(A_* + \Lambda_3^2 / R^2)$, with $A_* = 0.3$ and $\Lambda_3 = 40$ nm. Reprinted from Surface Science, vol. 601, V. G. Dubrovskii, N. V. Sibirev, R. A. Suris, G. E. Cirlin, J. C. Harmand and V. M. Ustinov, Diffusion controlled growth of semiconductor nanowires: vapor pressure versus high vacuum deposition, pp. 4395-4401, Copyright (2007), with permission from Elsevier.

Integration of Eq. (6.11) at a time-independent NW radius gives

$$L = H\left[A_* + \left(\frac{\Lambda_3}{R} \right)^p \left(1 - be^{R_{GT}/R} \right) \right], \tag{6.13}$$

with $H = V_3 t$ as the effective deposition thickness. This simplified expression shows that the length decreases with their radius for thick enough NWs where the Gibbs-Thomson effect becomes negligible, while for thin NW the growth rate tends to zero at a certain minimum droplet size. NWs cannot be grown thinner that this minimum size due to the Gibbs-Thomson effect [65,82]. Therefore, the length-radius correlation is generally composed of an increasing part for thin NWs, then reaching a maximum and further decreasing toward larger R in the pure diffusion-controlled regime [65]. The probability to observe non-monotonic length-radius correlation increases for smaller radii and larger μ_3^L, while the length of thicker NWs decreases inversely proportional to R^p. Figures 6.4 and 6.5 present the examples of the inverse $L(R)$ correlations with $p = 1$ and 2, where the influence of the Gibbs-Thomson effect is not visible.

6.2. Chemical potentials for the VLS growth of III-V nanowires

Chemical potentials of group III and V atoms in a ternary Au-III-V liquid are given by

$$\mu_3^L = \mu_3^{PL} + k_B T \ln c_3 + \omega_{35} c_5^2 + \omega_{3Au}(1-c_3-c_5)^2 + (\omega_{35} + \omega_{3Au} - \omega_{5Au}) c_5 (1-c_3-c_5) + \ldots ,$$

$$\mu_5^L = \mu_5^{PL} + k_B T \ln c_5 + \omega_{35} c_3^2 + \omega_{5Au}(1-c_3-c_5)^2 + (\omega_{35} + \omega_{5Au} - \omega_{3Au}) c_3 (1-c_3-c_5) + \ldots , \qquad (6.14)$$

Here, μ_X^{PL} are the temperature-dependent chemical potentials of pure liquids and ω_{XY} are the binary interaction parameters between X and Y atoms accounting for deviations from ideality, for X, Y = 3, 5 and Au. The written terms with composition-independent interaction constants correspond to the regular solution model. In the so-called sub-regular solution model, ω_{XY} are allowed to depend on concentrations, as in Refs. [14] or [84]. In Ref. [14], the ω_{XY} were calculated according to Stringfellow [85]. Johansson *et al*. [84] took the ω_{XY} in the form $\omega_{XY} = \omega_{XY}^0 + \omega_{XY}^1 (c_X - c_Y)$, where ω_{XY}^0 and ω_{XY}^1 denote the zero-order and first-order binary interaction parameters, respectively. Higher order terms include ternary interactions, described by the (composition-independent) ternary interaction parameter $\omega_{35\,Au}$ (more parameters appear if ternary interactions are considered in a quaternary liquid during the Au-catalyzed growth of ternary III-V NWs [84]). To compute the chemical potential difference with respect to the solid state as given by Eq. (3.7), one needs to know the interaction parameters and the temperature-dependent $\mu_3^{PL}(T)$, $\mu_5^{PL}(T)$, and $\mu_{35}(T)$. The latter values values are usually referred to the standard reference states of pure elements at temperature T_0 = 298.15 K. The reader may refer to Refs. [14,40,84] for the parameters of different material systems.

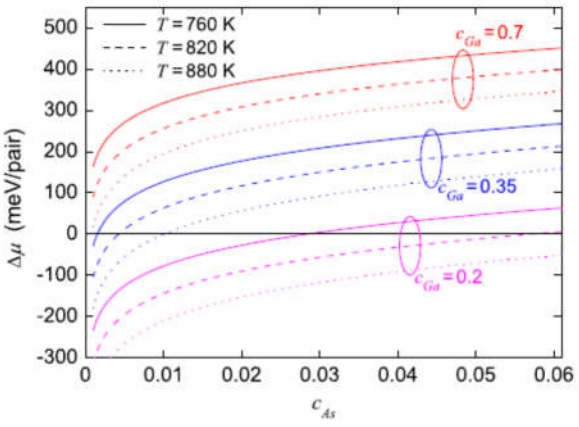

Figure 6.6. Variation with the atomic

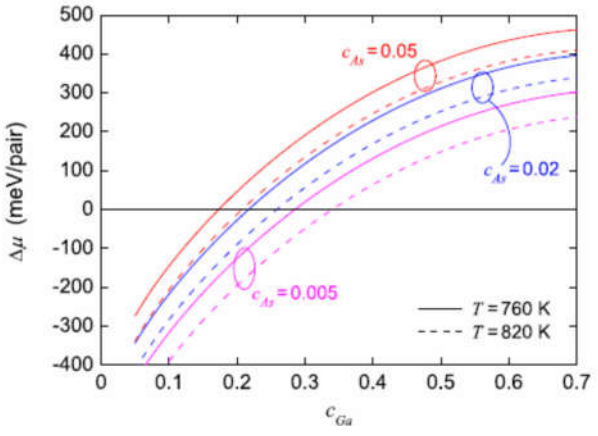

Figure 6.7. Variation with the atomic

concentration of As of the difference of chemical potential per Ga-As pair between a ternary Au-Ga-As liquid and solid ZB GaAs, calculated for a set of temperatures and Ga concentrations. Reprinted from F. Glas, Chemical potentials for Au-assisted vapor-liquid-solid growth of III-V nanowires, Journal of Applied Physics **108**, 073506 (2010), with the permission of AIP Publishing.

concentration of Ga of the difference of chemical potential per Ga-As pair between a ternary Ga-As-Au liquid and solid ZB GaAs, calculated for a set of temperatures and As concentrations. Reprinted from F. Glas, Chemical potentials for Au-assisted vapor-liquid-solid growth of III-V nanowires, Journal of Applied Physics **108**, 073506 (2010), with the permission of AIP Publishing.

Due to a low solubility of As and P atoms in liquid, their concentrations should be a few percent at most, and undetectable by compositional measurements. Conversely, group III atoms may take a significant fraction of the liquid. Figures 6.6 and 6.7 present chemical potentials $\Delta\mu$ for Au-catalyzed GaAs NWs calculated by Glas in Ref. [14]. Figure 6.6 shows chemical potential as a function of atomic concentration of As $c_5 = c_{As}$ between 0.001 and 0.06 at three different temperatures within the typical growth domain, and for three different Ga concentrations $c_3 = c_{Ga}$ of 0.2 0.35 and 0.7. Figure 6.7 shows chemical potential as a function of c_{Ga}, for three different c_{As} = 0.005, 0.02 and 0.05, and at two different temperatures. It is seen $\Delta\mu_{LS}$ is most sensitive to the group V concentration when the latter is less than ~ 0.01, whereas the variations with group III concentrations are more uniform. The $\Delta\mu$ increases with group III and group V concentrations in the range considered. However, this property is not critical and some calculations show that chemical potential may decrease with c_3 in group III rich regions [54]. At the fixed concentrations, $\Delta\mu$ always decreases with increasing temperature. These trends remain the same for other Au-III-V systems such as Au-In-As, Au-In-P and Au-Ga-P [14]. For WZ III-V NWs, all the curves will be shifted down by a constant value $\psi = \mu_{35}^{WZ} - \mu_{35}^{ZB}$ (ψ = 24 meV per pair for GaAs [7]).

6.3. Nucleation and growth of 2D islands

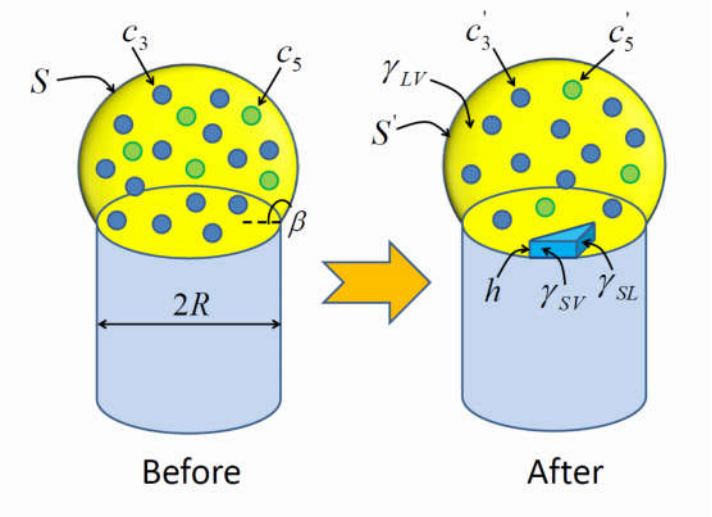

Figure 6.8. III-V VLS system with an Au-III-V droplet having the atomic concentrations c_3 of group III and c_5 of group V atoms before nucleation, decreasing to c_3' and c_5', respectively, after nucleation of a 2D island at the TPL. For highly volatile As or P species, the group V concentration is always much lower than the group III one. The island of height h consists of i III-V pairs. The contact angle of the droplet with respect to the horizontal equals β. The droplet base radius equals the NW radius R. The surface energies of interest are those of the liquid-vapor interface (γ_{LV}), solid-vapor lateral interface for one third of the island perimeter (γ_{SV}) and solid-liquid lateral interface for two thirds of the island perimeter (γ_{SL}) [86,87]. Reprinted with permission from V. G. Dubrovskii, Refinement of nucleation theory for vapor-liquid-solid nanowires, Crystal Growth & Design **17**, 2589-2593 (2017). Copyright (2017) American Chemical Society.

Figure 6.8 illustrates the VLS growth model for Au-catalyzed III-V NWs in the case of TPL nucleation. Let us first consider change of the surface energy upon island nucleation, assumed for the moment to be instantaneous. The edge of an island formed at the TPL comprises a solid-liquid interface with surface energy $(1-x_{TPL})Ph\gamma_{SL}$ and a solid-vapor interface with surface energy $x_{TPL}Ph\gamma_{SV}$, where P is the island perimeter and x_{TPL} its fraction along the TPL [42]. The surface energy of the droplet changes by $-x_{TPL}Ph\gamma_{LV}\sin\beta$ due to elimination of its portion replaced by the ML edge (this results in an effective areal energy $\gamma_{eff}=\gamma_{SV}-\gamma_{LV}\sin\beta$ for that portion of the TPL located at the TPL [42]; see also Section 11.2) and by $\gamma_{LV}\Delta S = 2\gamma_{LV}\sin\beta\,\Delta V/R$ due to the volume variation $\Delta V = (\Omega_S \quad \Omega_L)i$ in the liquid-solid phase

transition of i III-V pairs having the elementary volumes Ω_S and Ω_L in the solid and liquid phases, respectively [42,44]. This gives the additional Gibbs-Thomson term $2\gamma_{LV}\sin\beta(\Omega_S-\Omega_L)i/R$ (which is positive when $\Omega_S>\Omega_L$, as in the Au-Ga-As system [44]), proportional to the island size i (which is why it modifies the chemical potential). The total surface energy change thus equals [44]

$$\Delta G_{surf}=[(1-x_{TPL})\gamma_{SL}+x_{TPL}(\gamma_{SV}-\gamma_{LV}\sin\beta)]Ph+\frac{2\gamma_{LV}\sin\beta}{R}(\Omega_S-\Omega_L)i. \quad (6.15)$$

For $x_{TPL}=1$, $P=2\pi R$ and $i=\pi R^2h/\Omega_s$, this yields the exact result for the complete ML slice in the non-wetting growth mode (where the droplet sits entirely above the ML), namely $\Delta G_{surf}=[\gamma_{SV}-(\Omega_L/\Omega_S)\gamma_{LV}\sin\beta]2\pi Rh$ (Ref. [6]). Note that x_{TPL} generally changes during the island growth, which is considered in the generalized expression for the surface energy of Ref. [86]. In any case, the last, Gibbs-Thomson term in Eq. (6.15) is proportional to the difference between elementary volumes in the solid and liquid phase Ω_S Ω_L and becomes negligible when Ω_S Ω_L, as in the case of GaAs NWs [40,44].

Let us now include the volume energy change upon island formation [86]. For the fast growth stage of island that occurs before refill, let j_0 be the initial number of As atoms in the droplet, j_{eq} the number of As atoms corresponding to its equilibrium concentration with the solid phase, and i the number of As atoms (or GaAs pairs) in the single island growing in the mononuclear growth regime. In the closed system, the number of group V (As) atoms remaining in the droplet simply equals $j=j_0$ i. The concentration of As atoms in the droplet is $c=(j_0$ $i)/j_{tot}$, where j_{tot} $const$ is the total number of all atoms in the droplet, hence $c/c_{eq}=j/j_{eq}$. We introduce the dimensionless free energy of forming an island (formation energy for brevity) consisting of i III-V pairs (size for brevity), $F(i)=\Delta G(i)/k_BT$. According to the general result [86], its derivative with respect to size is given by

$$\frac{\partial F(i)}{\partial i}= [\mu(j_0 \quad i) \quad \mu_{eq}]+\frac{\partial\Gamma(i)}{\partial i}. \quad (6.16)$$

Here, $\mu(j_0 \quad i)$ is the chemical potential (in thermal units) of a III-V pair in a droplet containing $j_0 - i$ As atoms, μ_{eq} the equilibrium chemical potential, and $\Gamma(i) = \Delta G_{surf}/k_B T$ the island surface energy (with the Gibbs-Thomson term now removed from ΔG_{surf}) which scales as $i^{1/2}$ for small enough islands and in any case does not grow faster than $i^{1/2}$ [86]. The stopping size introduced in Ref. [87] corresponds to the minimum of the formation energy [86], while the critical size of CNT (which is of course smaller) is determined by its maximum. After reaching the stopping size, the island cannot continue growing from liquid; its further extension requires refill from vapor (for wurtzite GaAs NWs) or developing an interface truncation (for zincblende GaAs NWs), as described in Section 4 [86].

Let us derive Eq. (6.16) directly in the specific case of self-catalyzed GaAs NWs growing from a binary Ga-As liquid alloy droplet, in which the chemical potentials depend on a single concentration, for instance that of As. Then, the initial state of the liquid consists of j_0 As atoms (labeled "5"), with chemical potential $\mu_5(c_5)$, and $j_{tot} \quad j_0$ Ga atoms (labeled "3"), with chemical potential $\mu_3(c_5)$. Here, j_{tot} is the total number of atoms in liquid before nucleation and $c_5 = j_0/j_{tot}$ is the initial As concentration in liquid. The final state after nucleation and formation of a fractional ML consists of $j_0 \quad i$ As atoms in liquid, with chemical potential $\mu_5(c_5')$, $j_{tot} \quad j_0 \quad i$ Ga atoms in liquid, with chemical potential $\mu_3(c_5')$, and i GaAs pairs in solid, with chemical potential μ_{eq}. The As and Ga concentrations in the final state are $c_5' = (j_0$ $i)/(j_{tot} \quad 2i)$, and $c_3' = (j_{tot} \quad j_0 \quad i)/(j_{tot} \quad 2i)$, respectively, with $j_{tot} \quad 2i$ the total number of atoms remaining in liquid after removing i GaAs pairs. The free energy change upon forming the island of size i therefore equals

$$F(i) = \quad i\left[\mu_3(c_5') + \mu_5(c_5') \quad \mu_{eq}\right] + \Gamma(i) + j_0[\mu_5(c_5') \quad \mu_5(c_5)] + (j_{tot} \quad j_0)[\mu_3(c_5') \quad \mu_3(c_5)]. \tag{6.17}$$

Differentiating this with respect to i, we get

$$\frac{\partial F(i)}{\partial i} = \quad [\mu_3(c_5') + \mu_5(c_5') \quad \mu_{eq}] + \frac{\partial \Gamma(i)}{\partial i} + \left[(j_{tot} \quad j_0 \quad i)\frac{\partial \mu_3}{\partial c_5'} + (j_0 \quad i)\frac{\partial \mu_5}{\partial c_5'}\right]\frac{\partial c_5'}{\partial i}. \tag{6.18}$$

The first term in the right hand side of Eq. (6.18) is indeed the same as in Eq. (6.16). The second bracket in Eq. (6.18) equals zero regardless of the specific form of chemical potentials. This is a consequence of the equality $d\mu_3 = (c_5'/c_3')d\mu_5$ following from the Gibbs-Duhem equation for a binary system [86]. Using the expressions of c_5' and c_3', we get $d\mu_3 = [(j_0 - i)/(j_{tot} - j_0 - i)]d\mu_5$ and hence the second bracket term cancels. It can be shown that this result remains valid in the more general case of metal (Au)-catalyzed VLS growth of III-V NWs [86].

We now recall that the chemical potential of a III-V pair in the droplet is well approximated by a logarithmic function of the group V concentration (due to the low value of this concentration) [86], therefore

$$\mu_3(c_5') + \mu_5(c_5') - \mu_{eq} = \ln[(j_0 - i)/j_{eq}], \tag{6.19}$$

(this also holds for Au-catalyzed VLS growth, but then j_{eq} depends also on the Ga concentration). As recalled above, the stopping size i_s corresponds to the minimum of the formation energy [86,87]. Neglecting the variation of edge energy Γ (which is a good approximation if i_s is much larger than the critical size of CNT and smaller than a full ML [86]), it simply equals

$$i_s = j_0 - j_{eq}. \tag{6.20}$$

This corrects the result of Ref. [87], obtained under unnecessarily restrictive assumptions.

Using Eqs. (6.18) and (6.19), the formation energy itself is obtained by integration:

$$F(i) = -\int_0^i du \ln\left(\frac{j_0 - u}{j_{eq}}\right) + \Gamma(i). \tag{6.21}$$

The result is:

$$F(i) = -i\ln\left(\frac{j_0 - i}{j_{eq}}\right) + j_0 \ln\left(\frac{j_0 - i}{j_0}\right) + i + \Gamma(i). \tag{6.22}$$

This can be rewritten

$$F(i) = F_\infty(i) + (j_0 - i)\ln\left(1 - \frac{i}{j_0}\right) + i, \tag{6.23}$$

with

$$F_\infty(i) = -i\ln(j_0 / j_{eq}) + \Gamma(i) \tag{6.24}$$

$F_\infty(i)$ is the CNT result for infinite systems (not affected by depletion), which is indeed recovered from Eq. (6.23) at $i/j_0 \to 0$. Eq. (6.23) thus separates the CNT result $F_\infty(i)$ from a size-dependent correction which vanishes at $i/j_0 \to 0$.

Accounting for the refill from vapor and neglecting As desorption from liquid, the number of As atoms in the droplet by time *t* equals $j_0 \quad i + vt$, where v is the rate of refill and i the number of GaAs pairs in the island, as above. Note that between nucleation and time *t,* the volume enclosed by the droplet surface (liquid and island) increases by $V = (vt - i)\Omega_L + i\Omega_S$. Using Eq. (6.22), and presenting the result in terms of the ML coverage $\theta = i/i_{ML}$ (with $\mathrm{i_{ML}} = (3\sqrt{3}/2)\mathrm{R}^2 \ /\Omega_S$ the number of GaAs pairs in the complete ML and R the radius of the hexahedral NW), we obtain the normalized formation energy in the form

$$f = \frac{F}{i_{ML}} = (\theta \quad x)ln\left(\frac{\theta_0 - \theta + x}{\theta_{eq}}\right) + \theta_0 ln\left(1 \quad \frac{\theta - x}{\theta_0}\right) + \theta \quad x + \gamma(\theta) \quad x\left(\mu_{VS} \quad \frac{2\gamma_{LV}\Omega_S \sin\beta}{R}\right)$$

(6.25)

Here, $\theta_0 = j_0/i_{ML}$ is the initial As content at nucleation, $\theta_{eq} = j_{eq}/i_{ML}$ the equilibrium As content, $x = vt/i_{ML}$ the coverage equivalent to refill (which is proportional to time), μ_{VS} the chemical potential difference per Ga-As pair between vapor and solid, and $\gamma(\theta) = \Gamma(i)/i_{ML}$. In Ref. [86], we derived a representation of the ML edge energy from modeling *in situ* experiments [49], namely:

$$\gamma(\theta) = \alpha\left[A\theta^{1/2} + B(1 \quad \theta)^{1/2} \quad B + (1 \quad A + B)\theta\right]. \tag{6.26}$$

with $\alpha = 4\gamma_{eff}\Omega_{35}/\left(\sqrt{3}k_BTR\right)$ and γ_{eff} the effective surface energy of the island edge defined earlier. Eq. (6.26) correctly accounts for the non-monotonous variation of the edge energy with ML size and for leading terms $\sim i^{1/2}$ and $\sim (i_{ML} \quad i)^{1/2}$ at small and large sizes, respectively

[86]. This functional form is expected to be general but coefficients A =3.3748 and B = 2.2993 should vary with catalyst and contact angle (fits to *in situ* experiments on Au-catalyzed NWs [49] yield A =3.3748 and B = 2.2993 [86]).

The NW ML is completed at $\theta = 1$ whereas the ML formation cycle ends at $x = 1$, after a full equivalent ML of GaAs is added to the droplet from vapor. Since $\partial F/\partial i = \partial f/\partial \theta$, the minimum of the formation energy obtained by differentiating Eq. (6.25) at given refill yields the size θ_s of the island as a function of time. The extrema of the formation energy are given by

$$ln\left(\frac{\theta_0-\theta+x}{\theta_{eq}}\right) + \alpha\frac{d\gamma}{d\theta} = 0. \quad (6.27)$$

At $\alpha \ll 1$, corresponding to large NW radius R and low values of γ_{eff}, the influence of the surface energy term on island size is negligible. In this case, this size equals $\theta_s = \theta_0 \quad \theta_{eq} + x$, which is reduced to $\theta_s = \theta_0 \quad \theta_{eq}$ for instantaneous growth from liquid. Figure 6.9 (a) shows the behavior of $f + x(\ \mu_{VS} \quad 2\gamma_{LV}\Omega_S \sin\beta/R)$ as a function of θ at different x (and hence times) for a 20 nm radius GaAs NW, at a growth temperature of 610°C, in the case of a low surface energy γ_0 =0.037 J/m^2. For instance, values of θ_{eq}= 0.34 and θ_0 =0.7 yield the stopping size θ_s =0.36 in the absence of refill. Then, the minimum of the formation energy shifts to the right as x increases. This describes the slow growth stage at the rate of refill. The minimum of the formation energy is well approximated by the volume part of the formation energy shown by the dashed lines, which indicates a negligible effect of the island surface energy. The situation changes at a high surface energy, *e.g.* γ_{eff} = 0.25 J/m^2. According to Fig. 6.9 (b), the minimum of the formation energy then disappears for large enough x, meaning that fractional ML can grow even from equilibrium liquid. This effect is due to a decrease of the surface energy at high coverage, partly explained by a decrease of the island perimeter, which enables fast ML growth from undersaturated liquid [86]. These questions are investigated in detail in Ref. [86], where the present thermodynamic treatment is complemented by a kinetic model taking into account As desorption and a possible hindered incorporation to the growing ML.

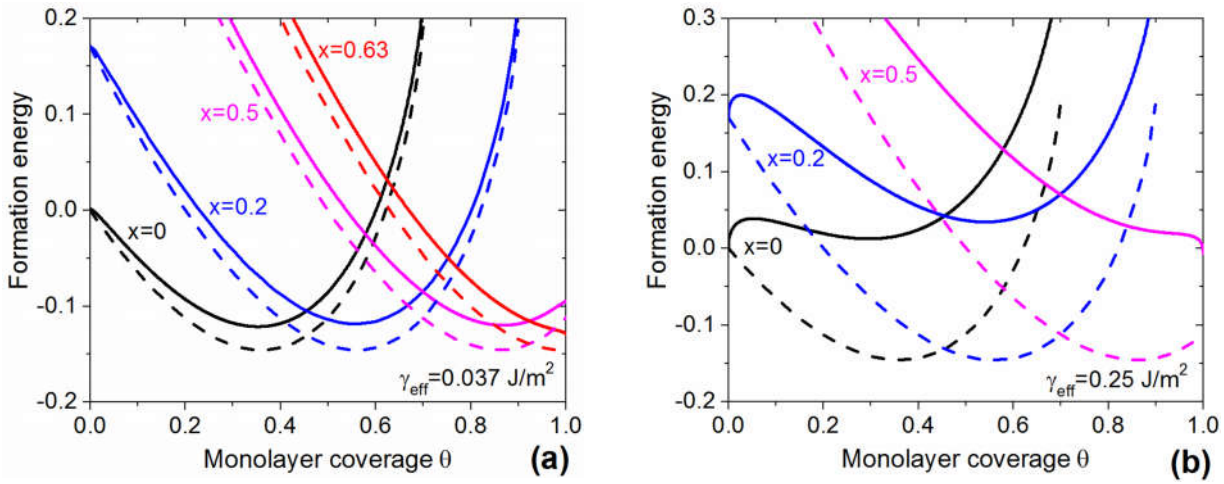

Figure 6.9. (a) Normalized island formation energy $f + x(\ \mu_{VS}\ \ 2\gamma_{LV}\Omega_S \sin\beta/R)$ versus θ for different x indicated near each curve (solid lines). The curves are obtained from Eqs. (6.25) and (6.26) for a GaAs NW with $R = 20$ nm, at T=610°C, θ_{eq}= 0.34, θ_0 =0.7 at a low γ_{eff} =0.037 J/m^2, corresponding to α =0.01584. Dotted lines show the volume part of the formation energy and correctly describe the stopping size in all cases. (b) Same as (a) at a high γ_{eff} =0.25 J/m^2, corresponding to α =0.1056. A minimum of the formation energy is observed only at small x and disappears above $x = 0.5$, due to a decrease of the ML surface energy [86]. The volume part of the formation energy gives an incorrect behavior at large x.

The stopping effect does not change the NW axial growth rate given by Eq. (3.10), which still equals the nucleation rate times the available area for nucleation at the maximum chemical potential within the ML growth cycle. However, it may affect the oscillations of the truncated facet [47] and nucleation statistics in VLS NWs [88] which in turn influence some important properties such as the preferred crystal phase and length uniformity within the NW ensembles. One important conclusion is that the nucleation probability in VLS NWs exponentially decreases immediately after nucleation, which makes the next nucleation improbable until the droplet is refilled from vapor [88]. In III-V NWs, this nucleation "antibunching" is critically sensitive to the concentration of group V atoms in the catalyst droplet.

6.4. Self-consistent growth models

The first fully self-consistent VLS growth model was developed by Glas *et al*. in Ref. [40] for Ga-catalyzed GaAs NWs grown by MBE. The NW growth rate given by the As input,

desorption and nucleation [stationary Eq. (3.1)] was solved numerically using Eq. (3.10) in the case of center nucleation. The Zeldovich nucleation rate was used given by Eq. (3.12). The model reproduces quantitatively all salient features of Ga-catalyzed VLS growth, namely the variations of the axial NW growth rate with the As flux, temperature, and NW radius.

Figure 6.10 (a) shows the calculated nucleation barrier $\Delta G_c = 3\sqrt{3}\Omega_S h\gamma_e^2/\Delta\mu$, chemical potential $\Delta\mu$, As concentration in the droplet c_{As}, and axial growth rate dL/dt as a function of As_4 BEP at a constant temperature of 610 ^oC. The As_4 BEP P_{As_4} was converted into the atomic As influx I_5 using the linear relationship $I_5 = \nu P_{As_4}$, with $\nu = 2.3\times10^{24}$ atoms$\times$m$^{-2}\times$s$^{-1}\times$Torr^{-1} for this MBE system [26]. Experimental data shown in the bottom panel were obtained for NW1 having a constant radius R of 32 nm, with $\beta \cong 125$. Figure 6.10 (b) shows the same quantities for NW2 grown under $P_{As_4} = 4.8\times10^{-6}$ Torr and different temperatures. For this NW, $R =$ 37 nm and β =125 . The crystal phase of both NWs was ZB. It is interesting to note that this contact angle is close to the one corresponding to vertical growth of ZB GaAs NWs in Figure 4.2 (between 125^o and 127^o). The best fits to the data were obtained with the re-emission coefficient $\alpha_r =$ 3.25 and temperature-independent J_0 and γ_{eff} given in Section 3.

According to these calculations, the As concentration increases almost linearly with the As flux and temperature, and varies only from ~ 0.01 to 0.015 in the experimental range. The chemical potential also does not vary much over the experimental range, remaining within the interval of 115-160 meV. These small variations result in almost linear correlation of the axial growth rate with As flux, as observed earlier in Ref. [22]. The decrease of dL/dt with temperature is stronger than linear. The radius dependence of the axial growth rate will be discussed shortly.

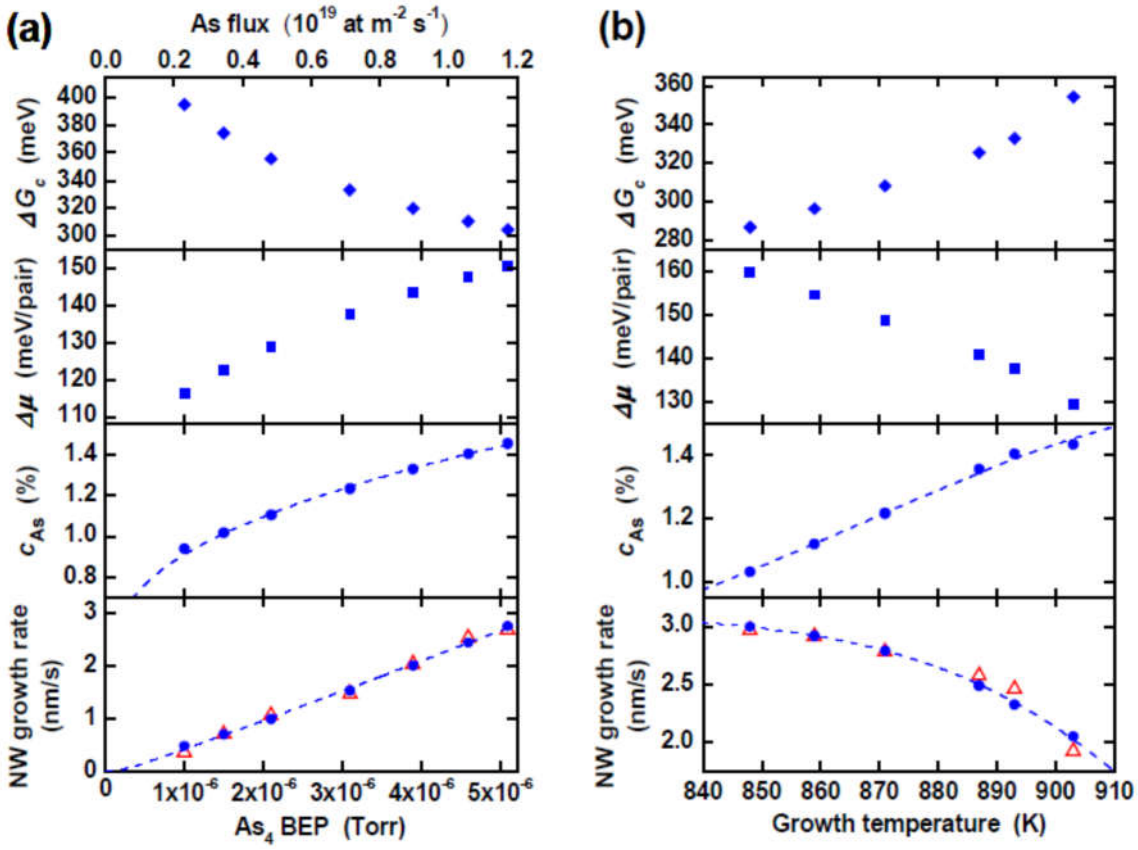

Figure 6.10. (a) Bottom panel: growth rates measured (triangles) and calculated (disks) for NW1, as a function of incoming As flux, at temperature T= 883 K. Three upper panels: As concentration in the droplet, difference of chemical potential between liquid of composition c_{As} and solid ZB GaAs, and nucleation barrier, calculated for each discrete data point of bottom panel. In the two bottom panels, the dashed lines are calculations extended to the whole pressure range, made for NW1 using the best model parameters. The As flux is expressed as BEP (lower scale) and as absolute atomic flux. (b) Same as (a) for NW2, as a function of growth temperature. Reprinted figure with permission from F. Glas, M. R. Ramdani, G. Patriarche and J. C. Harmand, Physical Review B **88**, 195304 (2013), https://doi.org/10.1103/PhysRevB.88.195304. Copyright (2013) by the American Physical Society.

In Ref. [41], an analytic approach was developed for the self-consistent description of Au-catalyzed and self-catalyzed VLS growth of III-V NWs, based on some earlier results [78]. Using the simplified diffusion flux of group III adatoms as given by Eq. (6.11), it is easy to obtain

$$\frac{dR}{dt}=\frac{\widetilde{\Omega}_L}{\Omega_S f(\beta)}\left[\chi_3 v_3+\left(\frac{\Lambda_3}{R}\right)^p\left(\varphi_3 v_3-\frac{h}{\tau_3}e^{\bar{\mu}_3^L}\right)-\frac{dL}{dt}\right], \tag{6.28}$$

$$\bar{\mu}_5 = \frac{1}{\nu}\ln\left(\frac{\chi_5 v_5 - dL/dt}{v_5^{des}}\right). \tag{6.29}$$

Equation (6.28) describes the time evolution of the NW radius (at a fixed contact angle β), with with v_3 as the deposition flux in nm/s and τ_3 as the characteristic time constant for the reverse diffusion flux from the droplet to the NW sidewalls, which is proportional to $\exp(\bar{\mu}_3^L)$. Equation (6.29) gives chemical potential of group V atoms in the droplet, for gaseous precursor incorporating ν As atoms, with v_5 as the vapor flux including re-emitted species and v_5^{des} as the pre-exponent in the desorption rate. The NW elongation rate in the mononuclear regime is given by Eq. (3.10), with the Zeldovich nucleation rate of CNT $J \propto \exp[-a^2/(4\Delta\bar{\mu})]$, as in Eq. (3.11).

Under certain assumptions, solution to the closed system of stationary Eq. (6.28), Eq. (6.29) and (3.11) can be approximated by the following analytical formula for the growth rate

$$\frac{dL}{dt} = \frac{\nu\chi_5 v_5}{(1+\Delta)(1+G)}, \tag{6.30}$$

with

$$G = \frac{i_*}{W[(R/R_*)^2\eta(1+\Delta)]}, \tag{6.31}$$

$$\Delta = \frac{\nu\chi_5 v_5}{\chi_3 v_3 + (\Lambda_3/R)^p \varphi_3 v_3} = \frac{\nu F_{53}}{1+(\varphi_3/\chi_3)(\Lambda_3/R)^p}, \tag{6.32}$$

and $W(y)$ is the Lambert function such that $W\exp(W) = y$. The F_{53} stands for the effective V/III flux ratio, defined as $F_{53} = \chi_5 v_5/(\chi_3 v_3)$. The "nucleation" radius R_* is given by

$$R_* = \left(\frac{\nu\chi_5 v_5}{\pi h i_* J(\Delta\bar{\mu}_0)}\right)^{1/2} \tag{6.33}$$

with chemical potential $\Delta\bar{\mu}_0$ containing characteristics of the vapor phase and becoming radius-independent in many practical cases,

$$\Delta\mu_0 = \ln\left(\frac{\chi_3 v_3 + (\Lambda_3/R)^p \varphi_3 v_3}{(\Lambda_3/R)^p (h/\tau_3)}\right) + \frac{1}{\nu}\ln\left(\frac{\chi_5 v_5}{v_5^{des}}\right) - \mu_{35}. \tag{6.34}$$

The $i_* = i_c(\Delta\mu_0)$ denotes the critical size at this chemical potential.

The axial growth rate given by Eq. (6.30) is reduced to the transport-limited growth rate given when $\Delta >> 1$ and $G << 1$, while at $G >> 1$ it yields the nucleation-limited growth rate. In some regimes, this model is further reduced to the result of Ref. [78], providing explicitly the NW length in the form

$$L = H\left(\frac{\widetilde{\Lambda}_3}{R}\right)^p W\left[\left(\frac{R}{R_n}\right)^{p+q}\right]. \tag{6.35}$$

Here, H is the deposition thickness, $\widetilde{\Lambda}_3$ is the re-normalized diffusion length of group III adatoms, R_n is the re-normalized nucleation radius (which depends on the kinetics of group V species), and the index q equals 2 for the center and 1 for the TPL nucleation position.

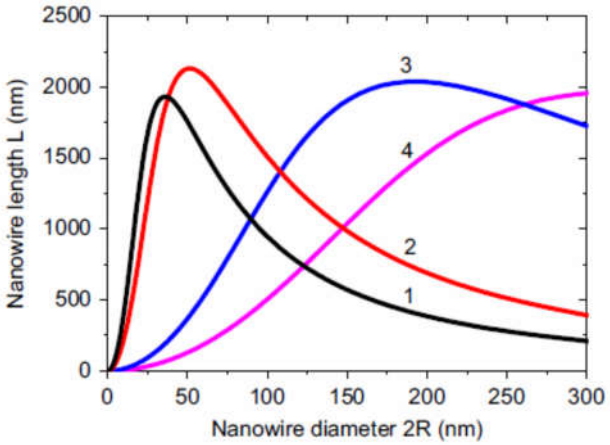

Figure 6.11. Transition from non-monotonic to increasing length-diameter correlation with increasing R_n, obtained from Eq. (6.35) at $p = q = 2$: curve 1- R_n = 14 nm, $\widetilde{\Lambda}_3$=50 nm; curve 2 - R_n=40 nm, $\widetilde{\Lambda}_3$ = 75 nm; curve 3 - R_n = 75 nm, $\widetilde{\Lambda}_3$ = 225 nm; curve 4 - R_n = 125 nm, $\widetilde{\Lambda}_3$ = 450 nm. Reprinted from Journal of Crystal Growth, vol. 401, V. G. Dubrovskii and Yu. Yu. Hervieu, Diffusion-induced growth of nanowires: generalized boundary conditions and self-consistent kinetic equation, pp. 431-440, Copyright (2014), with permission from

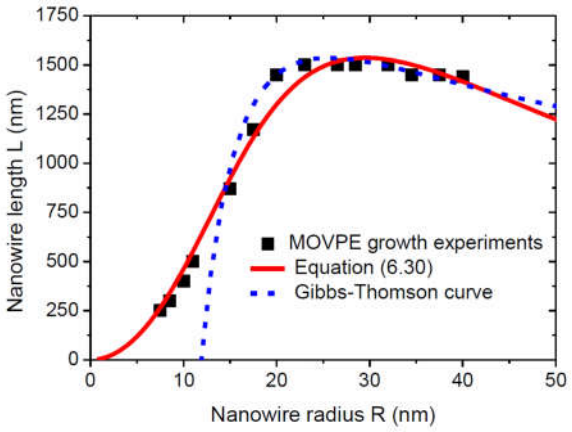

Figure 6.12. Length-radius correlation of MOVPE-grown InP NWs [89], fitted by Eq. (6.35) (solid line) and by the Gibbs-Thomson curve [65] (dashed line). Reprinted from Journal of Crystal Growth, vol. 401, V. G. Dubrovskii and Yu. Yu. Hervieu, Diffusion-induced growth of nanowires: generalized boundary conditions and self-consistent kinetic equation, pp. 431-440, Copyright (2014), with permission from Elsevier.

Elsevier.

Similarly to Eq. (6.30), Eq. (6.35) describes the diffusion-limited regime (for sufficiently thin NWs) at small R_n, transitioned to the nucleation-limited regime at large R_n. The *L(R)* correlation transitions from non-monotonic to monotonically increasing, as shown in Figure 6.11. The limitation of the axial growth rate at small R is explained, roughly, by a small facet area available for nucleation even without the Gibbs-Thomson effect. Figure 6.12 shows the example of non-monotonic length-radius curve for Au-catalyzed InP NWs grown by MOVPE at 470 ^{o}C [89]. The NW length first increases with R, then saturates at about 22 nm, and starts to slightly decrease after that. The fit obtained from Eq. (6.35) with $p = q = 2$, $H\Lambda^2$ = 1340 nm^3 and $R_* = 23$ nm provides better fit than the Gibbs-Thomson curve [65], particularly for thinner NWs. More examples of different length-radius correlations of III-V NWs, related to their crystal phase, fitted by a more general Eq. (6.30), can be found in Ref. [41]. It turns out that WZ GaAs NWs usually exhibit the transport-limited inverse length-radius correlations, while ZB GaAs NWs often show lengths that increase with the radius, and in this sense become similar to the self-catalyzed case.

For self-catalyzed III-V NWs, the analytic approximation for the axial growth rate is given by [41]

$$\frac{dL}{dt} = \frac{\chi_5 v_5}{1+\delta} \ , \tag{6.36}$$

with

$$\delta = \frac{i_c}{\nu W[(R/R_*)^2]} \ . \tag{6.37}$$

The nucleation radius R_* is given by Eq. (6.33) but at the different, radius-independent chemical potential

$$\Delta\mu_0 = \mu_3(1) + \frac{1}{\nu}\ln\left(\frac{\chi_5 v_5}{v_5^{des}}\right) - \mu_{35} \ . \tag{6.38}$$

Here, the value of $\mu_3(1)$ now relates to pure Ga droplet and hence cannot regulate the overall diffusion flux of Ga adatoms.

Because of that, there is no steady state solution to Eq. (6.28) for R and instead the NW top radius becomes time-dependent. When $\delta << 1$, Eq. (6.36) yields $dL/dt = \chi_5 v_5$, that is, the NW growth rate is simply proportional to the total As influx, including re-emitted flux. If we also assume $p = 1$ and $\varphi_3 v_3 >> h\exp(\bar{\mu}_3)/\tau_3$, Eq. (6.28) yields the result of Ref. [25]

$$\frac{dR}{dt} = a + \frac{b}{R}, \tag{6.39}$$

with the coefficients

$$a = g(\chi_3 v_3 - \chi_5 v_5),\ b = g\varphi_3 v_3 \Lambda_3. \tag{6.40}$$

Here, $g = \Omega_L/[\Omega_{35} f(\beta)]$ is the shape constant, which can be treated as time-independent at $\beta = const$. Integrating this with the initial condition $R(t = t_0) = R_0$, one obtains

$$t = t_0 + \frac{R - R_0}{a} + \frac{b}{a^2}\ln\left(\frac{R_0 + b/a}{R + b/a}\right). \tag{6.41}$$

Using $dL/dt = \chi_5 v_5$, the shape of Ga-catalyzed GaAs NWs can be put as

$$L = L_0 + \frac{F_{53}}{g(F_{53} - 1)}\left[R_0 - R + R_s \ln\left(\frac{R_0 - R_s}{R - R_s}\right)\right]. \tag{6.42}$$

From Eqs. (6.39), (6.40), we have

$$R_s = -\frac{b}{a} = \frac{\varphi_3 \Lambda_3}{\chi_3(F_{53} - 1)}. \tag{6.43}$$

Here, R denotes the NW top radius corresponding to its length L at a given moment of time, but can also be treated as the radius at a given position along the NW ("height") without subsequent VS radial growth on the sidewalls. The radius increases with time, or with the height when $a > 0$, corresponding to the case of positive Ga to As imbalance ($F_{53} < 1$ and $R_s < 0$). When $F_{53} > 1$, positive R_s gives the stable NW radius as will be discussed shortly.

Figure 6.13 shows the excellent correlation between the model given by Eqs. (6.36) and (6.37) and the numerical calculations of Glas *et al.* [40] for the growth rates of MBE-grown, Ga-catalyzed GaAs NWs versus the NW radius at two different temperatures. The calculations of Ref. [40] were performed under the assumption of a time-independent NW radius, for an As flux of 0.498 nm/s, a droplet contact angle of 125° and a re-emission coefficient of 3.1, yielding $\chi_5 v_5 = 3.04$ nm/s. The best fits by the analytic expressions yield a nucleation radius R_* of 20 nm at 610°C and 27 nm at 640°C. This should be due to a higher As desorption coefficient v_5^{des} which decreases the $\Delta\mu_0$ in Eq. (6.38) toward higher temperatures. While the fits by the analytic expressions are good, we note that they require very small values of the critical sizes (~ 2 GaAs pairs) where CNT reaches its limit.

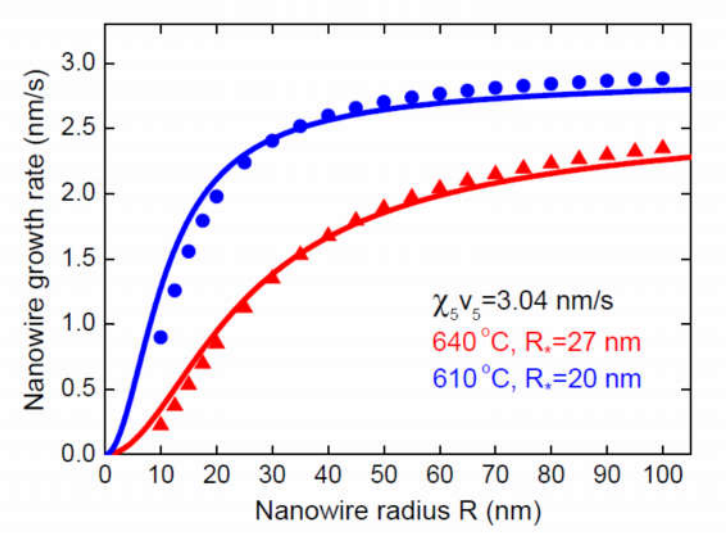

Figure 6.13. Growth rate of Ga-catalyzed GaAs NWs grown by MBE versus the NW radius at two different temperatures. Numerical calculations of Ref. [40] (symbols) and fits by Eqs. (6.36), (6.37) with the parameters listed in the insert [90]. Reprinted from Journal of Crystal Growth, vol. 440, V. G. Dubrovskii, Group V sensitive vapor-liquid-solid growth of Au-catalyzed and self-catalyzed III–V nanowires, pp. 62-68, Copyright (2016), with permission from Elsevier.

In Ref. [90], the shapes of Ga-catalyzed GaP NWs grown at 600 °C by gas source MBE in patterned arrays on Si(111) substrates was analyzed as a function of V/III flux ratio. The shape of these NWs was not considerably affected by radial VS growth on the sidewalls. In particular, Figure 6.14 shows an example of a NW array grown with a V/III flux ratio of 4, whose shape is

tapered toward the top. For high V/III flux ratios, some shorter NWs were systematically observed without any droplets on top. Figure 6.15 shows the measured shapes of NWs for different V/III flux ratios changing from 1 to 6. It is seen that the NWs are reverse tapered for at V/III=1, almost straight at V/III=3, and tapered for V/III>3, with the degree of tapering increasing for higher V/III. These results are fully consistent with the model presented above, and well fitted by Eqs. (6.41), (6.42) with the parameters detailed in Ref. [90]. In particular, the stable radius R_s was found in the range 12-18 nm for the V/III flux ratios from 3 to 6.

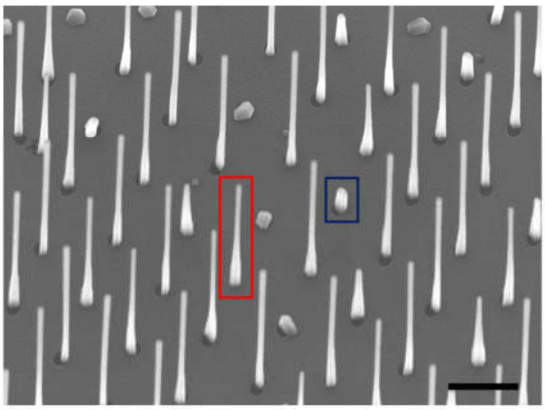

Figure 6.14. 30° tilted SEM image of an array of self-catalyzed GaP NWs for a V/III flux ratio of 4. Two types of NWs, with (red box) and without (blue box) Ga droplets are indicated. Scale bar is 440 nm. Reprinted from E. D. Leshchenko, P. Kuyanov, R. R. LaPierre and V. G. Dubrovskii, Tuning the morphology of self-assisted GaP nanowires. Nanotechnology **29**, 225603 (2018); https://doi.org/10.1088/1361-6528/aab47b. © IOP Publishing. Reproduced with permission. All rights reserved.

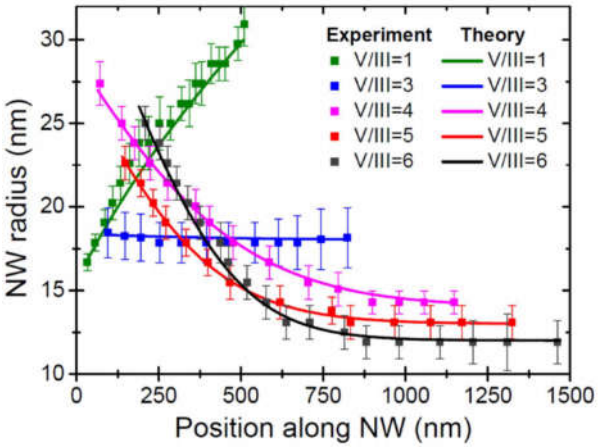

Figure 6.15. Experimental (symbols) and theoretical (lines) morphologies of GaP NWs at a fixed pitch of 360 nm and different V/III flux ratios. Experimental morphologies correspond to a fixed growth time of 870 s under different V/III flux ratios after the initial growth step of 435 s at a fixed V/III=2 to form the NW stems. The measured and calculated shapes correspond only to the upper NW parts, with the initial conditions $R_0(L_0)$ relating to the initial stems. Reprinted from E. D. Leshchenko, P. Kuyanov, R. R. LaPierre and V. G. Dubrovskii, Tuning the morphology of self-assisted GaP nanowires. Nanotechnology **29**, 225603 (2018); https://doi.org/10.1088/1361-6528/aab47b. © IOP Publishing. Reproduced with permission. All rights reserved.

7. Self-equilibration of the radius of self-catalyzed nanowires

Equations (6.41) and (6.42) demonstrate that the radius distribution of self-catalyzed III-V NWs can be narrowed during growth to an almost delta-like shape due to the unusual self-focusing effect. This effect can be observed if the group V atomic flux into the droplet, including re-emitted species, is larger than that of group III ($F_{53} > 1$). A positive diffusion flux of group III atoms from the NW sidewalls contributes more to the increase of droplet volume for thinner NWs and less for thicker NWs. Therefore, larger droplets will grow and smaller droplets will shrink until the diffusion flux equalizes the positive group V to III imbalance. As a result, the droplet volume will converge to a certain stationary one regardless of the initial size distribution of the growth seeds. For a fixed contact angle of the droplet, increase or decrease of the droplet volume leads to extending or diminishing the radius of the NW top. This was predicted theoretically in Ref. [25] and later in Ref. [34], and confirmed experimentally in Ref. [28] for Ga-catalyzed GaAs NWs.

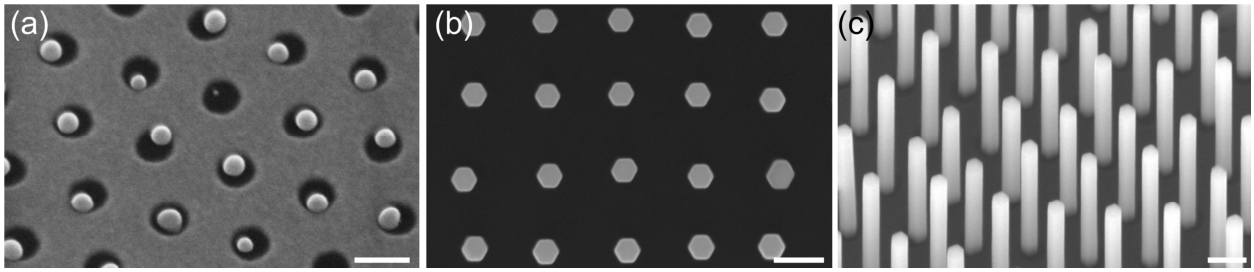

Figure 7.1. 30° tilted SEM image of Ga droplets obtained after predeposition of Ga onto a hole array in a SiO_2 on Si(111) substrate. The diameter of the holes is 60 nm and the pitch between the holes is 100 nm. (b) and (c) show top view and 30° tilted SEM images of self-catalyzed GaAs NWs grown from the array of Ga droplets shown in (a). Scale bar corresponds to 100 nm. Reprinted with permission from V. G. Dubrovskii, T. Xu, A. Díaz Álvarez, G. Larrieu, S. R. Plissard, P. Caroff, F. Glas, B. Grandidier, Self-equilibration of the diameter of Ga-catalyzed GaAs nanowires, Nano Letters 15, 5580-5584 (2015). Copyright (2015) American Chemical Society.

These NWs were grown by MBE on Si(111) substrates through three steps: (i) patterning of a hole array in a thin SiO_2 layer, (ii) predeposition of Ga to form droplets in the etched holes, and (iii) growth of NWs at a temperature of 630°C, As/Ga growth rate equivalent ratio of 1.8 and

2D equivalent growth rate of GaAs of 1 ML/s for 5 min. Figure 7.1 shows the SEM images obtained after steps (ii) and (iii) for an array of holes with a diameter of 60 nm and a pitch of 100 nm. It is seen that the Ga predeposition leads to the formation of Ga droplets in the oxide-free openings only, resulting in the growth of NWs at the position of the holes. While the diameter of the Ga droplets varies significantly from hole to hole (the droplet diameter distribution may depend on the droplet preparation process but is never uniform), a high degree of uniformity of the NW diameters is noticed.

This difference between the droplet size distribution and the NW diameter distribution was reproducible, whatever the initial size and the pitch between the holes in the array are. For example, Figure 7.2 compares the size distribution of the Ga droplets with the distribution of the NW diameters for an array with a hole size of 60 nm and a pitch of 250 nm. Again, the NWs in the array are quite uniform and the NW diameter distribution appears clearly much narrower than the hole size distribution. The Ga-catalyzed growth of NWs leads to a focusing effect towards a diameter of ~ 50 nm, slightly bigger than the peak value of the droplet size distribution, but still smaller than the hole size.

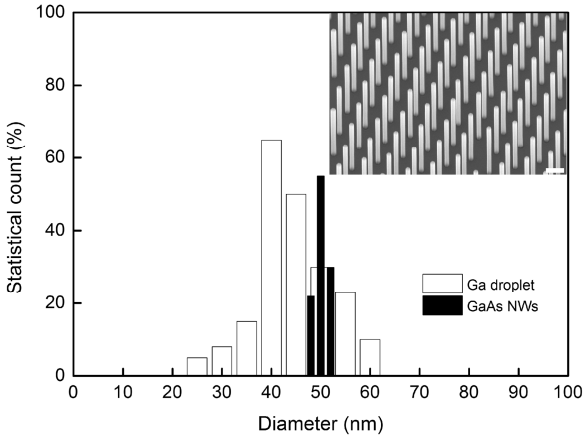

Figure 7.2. Histograms of the Ga droplet size distribution and the NW diameter distribution. Inset: 30°tilted SEM images of the corresponding array of GaAs NWs with the hole size and pitch of 60 nm and 250 nm, respectively. Scale bar in the insert corresponds to 100 nm. Reprinted with permission from V. G. Dubrovskii, T. Xu, A. Díaz Álvarez, G.

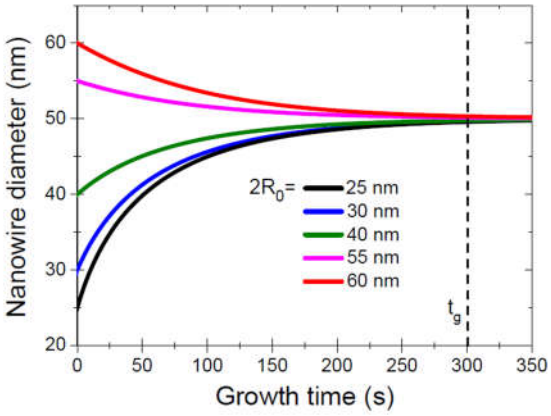

Figure 7.3. Time dependences of the NW diameters obtained from Eq. (6.41) with $t_0 = 0$, different R_0, a=-0.30 nm/s and b=7.50 nm^2/s. The vertical dash segment indicates the experimental growth time of 300 s, where full self-equilibration of the NW diameter is reached.

Larrieu, S. R. Plissard, P. Caroff, F. Glas, B. Grandidier, Self-equilibration of the diameter of Ga-catalyzed GaAs nanowires, Nano Letters **15**, 5580-5584 (2015). Copyright (2015) American Chemical Society.

Reprinted with permission from V. G. Dubrovskii, T. Xu, A. Díaz Álvarez, G. Larrieu, S. R. Plissard, P. Caroff, F. Glas, B. Grandidier, Self-equilibration of the diameter of Ga-catalyzed GaAs nanowires, Nano Letters **15**, 5580-5584 (2015). Copyright (2015) American Chemical Society.

Figure 7.3 shows the time evolution of the NW diameters for the array shown in Figure 7.2. These curves are obtained from Eq. (6.41) with a=-0.30 nm/s and b=7.50 nm^2/s, corresponding to the stable radius $R_s = 25$ nm for the given MBE growth conditions. These curves can equivalently be presented in the form of $R(L)$ dependence using Eq. (6.42) with the known NW axial growth rate of 3.33 nm/s. It is seen that the initial inhomogeneity of the droplet diameters, ranging from 25 to 60 nm, converges to the size-uniform array of NW after only 5 min of MBE growth.

8. Length distributions of nanowires

Consider an ensemble of VLS NWs growing from pre-existing catalyst droplets on a substrate. Then the number density of NWs having the length of $s = L/h$ MLs, with $s = 0,1,2...$, including free droplets (at $s = 0$), equals the number density of the initial droplets at any time t. Therefore, the length distribution (LD) of NWs $f_s(t)$ can be normalized to unity, $\sum_{s=0}^{\infty} f_s)(t) = 1$. The set of rate equations describing the time evolution of the LD has the form [91-96]

$$\frac{df_0}{dt} = -p_0 f_0 ,$$

$$\frac{df_s}{dt} = p_{s-1} f_{s-1} - p_s f_s , \; s = 1,2,3... \; . \tag{8.1}$$

Here, $p_s(t)$ are the probabilities of adding 1 ML to the NW of length s per unit time (or the instantaneous growth rate of the NW of length s), including the probability of forming the very first ML from the droplet laying on the substrate surface $p_0(t)$. These probabilities generally

depend on s and t. From the first equation, $f_0(t) = \exp(-p_0 t)$ for a time-independent p_0, and the nucleation rate of NWs on the substrate is given by $J(t) = p_0 \exp(-p_0 t)$.

The continuum approximation reduces the discrete set of Eqs. (8.1) at $s >> 1$ to the Fokker-Planck type equation in partial derivatives [92,95,96]

$$\frac{\partial f(s,t)}{\partial t} = -\frac{\partial}{\partial s}[p(s,t) f(s,t)] + \frac{1}{2}\frac{\partial^2}{\partial s^2}[p(s,t) f(s,t)], \tag{8.2}$$

If Green's function $F(s,t)$ of this equation is obtained, the resulting LD is given by the convolution of Green's function with the nucleation rate [96]

$$f(s,t) = \int_0^t dt F(s, t-\tau) J(\tau). \tag{8.3}$$

The simplest case corresponds to the so-called Poissonian growth, where

$$p_s = v, \; s = 0,1,2... . \tag{8.4}$$

Here, v is the vapor flux onto the droplet surface in ML/s, which determines the probabilities of adding the MLs to NWs of any length. Then the exact solution to Eqs. (8.1) is given by the Poisson LD [91]

$$f_s(t) = e^{-Vt}\frac{(vt)^s}{s!} \cong \frac{1}{\sqrt{2\pi vt}} \exp\left[-\frac{(s-vt)^2}{2vt}\right]. \tag{8.5}$$

The discrete Poisson LD rapidly converges to the continuum Gaussian (the approximate expression). The mean length $\langle s \rangle$ and variance σ^2 of this LD equal vt, corresponding to the standard deviation (width) which spreads with time as $\sigma = \sqrt{vt}$, or

$$\langle s \rangle = \tau, \;\; \sigma^2 = \tau \tag{8.6}$$

with $\tau = vt$.

The measured [30,31,92,93,97] and modeled [30,31,92-97] NW LDs are commonly compared to this Poissonian case.

Without one specific effect which will be discussed later on, the Poisson LD is the best case regarding the length uniformity. There are several effects contributing into the LD broadening, including (i) a nucleation delay due to difficult nucleation of NWs emerging from the substrate; (ii) continuing nucleation of the seed droplets during the NW growth, as in the Ga-catalyzed growth of GaAs NWs without Ga pre-deposition [97], (iii) surface diffusion of group III adatoms, (iv) collective effects in the NW growth such as shadowing in directional MBE method, and (v) initial size inhomogeneity of the droplets.

To account for the nucleation delay for NWs whose growth rate is controlled by the direct impingement from vapor, the probabilities $p_s(t)$ are written in the form

$$p_0 = \alpha v,\ p_s = v, s =,1,2,3... \ . \tag{8.7}$$

Here, $\alpha < 1$ describes difficult nucleation of the very first NW ML relative to the upper layers. The corresponding continuum LD is now given by [92]

$$f(s,\tau) = \frac{\alpha}{2} e^{\alpha(s-\tau)+\alpha^2\tau/2} erfc\left[\frac{s-\tau+\alpha\tau}{\sqrt{2\tau}}\right]. \tag{8.8}$$

The $erfc(y)$ is the complimentary error function defined according to

$$erfc(y) = \frac{2}{\sqrt{\pi}} \int_y^\infty dt e^{-t^2} \ . \tag{8.9}$$

The mean length and variance of this LD, assuming that it is fully formed ($f(s=0,\tau) \to 0$), equal

$$\langle s \rangle = \tau - \frac{1}{\alpha},\ \sigma^2 = \tau + \frac{1}{\alpha^2}, \tag{8.10}$$

showing that the mean length decreases and the variance increases with respect to the Poisson case.

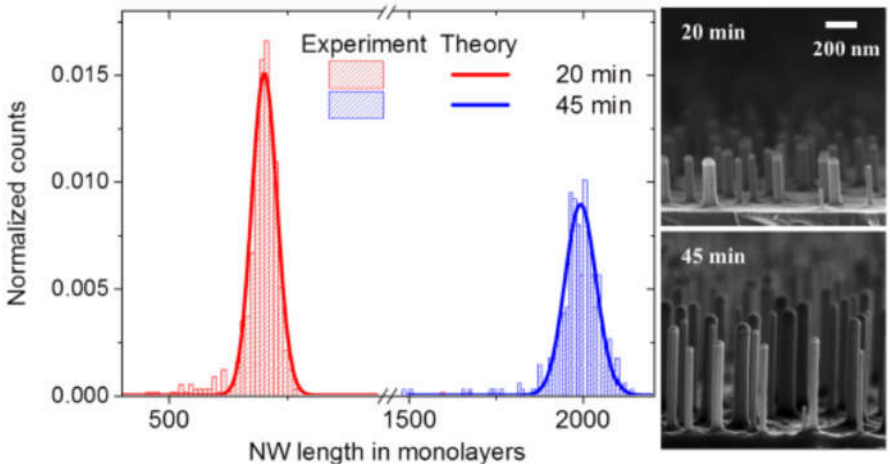

Figure 8.1. (a) Normalized LDs (histograms) fitted by the Poissonian shapes (lines) for Au-catalyzed InAs NWs grown by CBE for 20 and 45 min from Au nanoparticles obtained by thermally dewetting of 0.5 nm thick Au film at 510 °C for 20 min, along with their plan view SEM images. Reprinted from V. G. Dubrovskii, N. V. Sibirev, Y. Berdnikov, U. P. Gomes, D. Ercolani, V. Zannier and L. Sorba, Length distributions of Au-catalyzed and In-catalyzed InAs nanowires, Nanotechnology **27**, 375602 (2016); doi:10.1088/0957-4484/27/37/375602.

The Poisson LDs were obtained in Ref. [92] for InAs NWs grown at 380 ^{o}C on InAs(111)B substrates with Au nanopartciles obtained by thermal dewetting of a thin Au film. These data are shown in Figure 8.1, and confirm that the VLS growth of these InAs NWs is controlled by the direct vapor flux. Figure 8.2 shows the LDs of InAs NWs grown for 60 and 130 min from 40 nm Au colloids annealed at 500 °C, along with the corresponding SEM micrographs. These NWs clearly feature much broader LDs with a long left tail that spread with the growth time. Clearly, no new Au nanoparticles can emerge after starting the InAs deposition. and thus the striking difference in the LD shapes between Figures 8.1 and 8.2 should be associated with a much longer nucleation step of InAs NWs grown from Au colloidal nanoparticles.

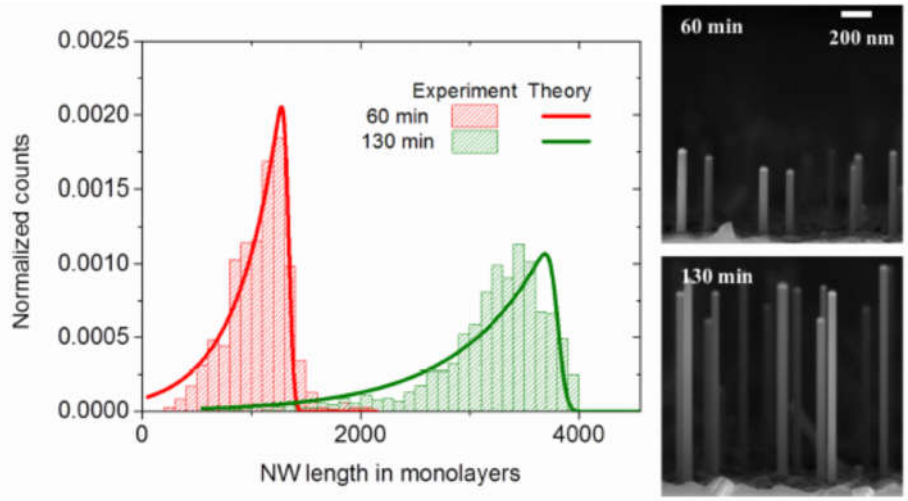

Figure 8.2. Normalized LDs (histograms) of Au-catalyzed InAs NWs grown from 40 nm colloids annealed at 500 °C for 60 and 130 min, along with their plan view SEM images. The fits (lines) are obtained from Eq. (8.8) with α = 0.0025 for 60 min and 0.0013 for 130 min. Reprinted from V. G. Dubrovskii, N. V. Sibirev, Y. Berdnikov, U. P. Gomes, D. Ercolani, V. Zannier and L. Sorba, Length distributions of Au-catalyzed and In-catalyzed InAs nanowires, Nanotechnology **27**, 375602 (2016); doi:10.1088/0957-4484/27/37/375602. © IOP Publishing. Reproduced with permission. All rights reserved.

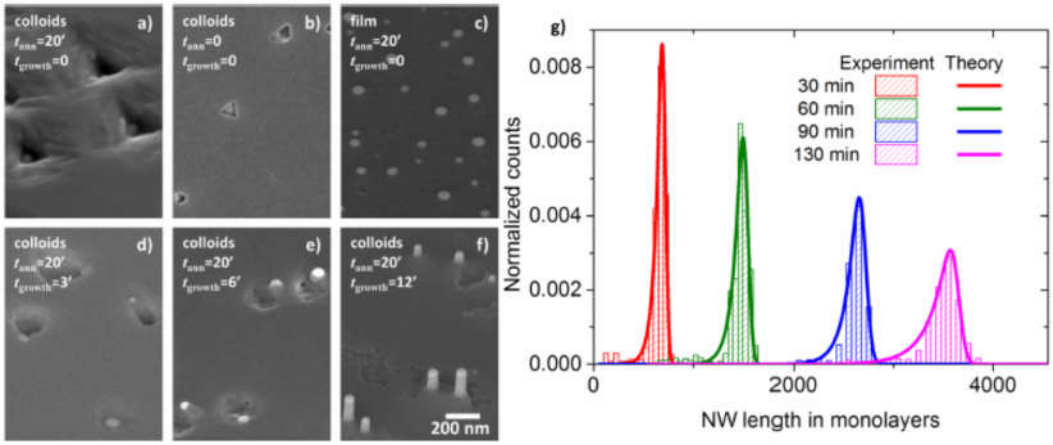

Figure 8.3. 45° tilted SEM image of (a) Au colloidal nanoparticles after the standard annealing step (20 min at 500 °C under TBAs=1.0 Torr), compared to (b) Au colloidal nanoparticles with just ramping the temperature up to 380 °C under TBAs=4.0 Torr and removing the annealing step; (c) the reference sample with thermally dewetted 0.5 nm thick Au film after the standard annealing step; (d)–(f) slow emerging of InAs NWs during the early stages of NW growth (3-12 min); (g) normalized LDs (histograms) of Au-catalyzed InAs NWs grown from Au colloids at 380 °C without the annealing step for 30, 60, 90 and 130 min respectively. The fits (lines) are obtained from Eq. (8.8) with α ranging from 0.0053 to 0.017. Reprinted from V. G. Dubrovskii, N. V. Sibirev, Y. Berdnikov, U. P. Gomes, D. Ercolani, V. Zannier and L. Sorba, Length distributions of Au-catalyzed and In-catalyzed InAs

It was noticed that during the standard annealing step (temperature ramp up to ~500 °C and substrate kept at this temperature for 20 min under TBAs=1.0 Torr), the Au colloidal nanoparticles dig deep into the substrate, as shown in the SEM micrographs in Figure 8.3 (a). The holes are formed as a result of interaction between Au nanoparticle and InAs substrate to form Au–In alloy accompanied by the evaporation of As. The nucleation delay causing the wide and asymmetric LDs in Figure 8.2 should be due to a slow re-emerging of Au nanoparticles from the holes when the NW growth is started. In fact, it is evident from the early stages of growth from 3 to 12 min illustrated in Figures 8.3 (d)–(f) that there is a significant delay in the NW nucleation due to the presence of holes. In order to minimize this effect, the annealing step was removed by just ramping the temperature up to 380 °C under TBAs=4.0 Torr which reduced the size of the holes, as shown in Figure 8. 3(b). InAs NWs were then grown at the same temperature. The measured LDs of these InAs NWs are shown in Figure 8.3 (g). It is clearly seen that the NWs grown without the annealing step feature much narrower and symmetric LDs, in comparison to the LDs of InAs NWs grown under exactly identical conditions but with the standard annealing step as shown in Figure 8.2, confirming that the nucleation delay is mainly due to the burial of Au nanoparticles during the annealing.

In the full agreement with this observation, the NW LDs shown in Figs. 8.2 are best fitted by Eq. (8.8) with α = 0.0025 for 60 min and 0.0013 for 130 min**.** This corresponds to a very long delay in nucleation of the very first NW ML, ~ 1000 times slower than in the upper layers. The best fits of the LDs shown in Figs. 8.3.correspond to α between 0.0053 and 0.017, which are on the order of magnitude larger than for the standard annealing step but still two orders of magnitude lower than in the best Poissonian case achieved for thermally dewetted Au film.

In-catalyzed InAs NWs [92] and Ga-catalyzed GaAs NWs [97], whose growth is accompanied by simultaneous nucleation of the group III droplets, feature much broader LDs than shown here, because the NWs continue to emerge from the newly formed droplets.

In Ref. [93], it was demonstrated experimentally and explained theoretically that NWs growing by surface diffusion of group III adatoms exhibit very broad LDs, with the variance increasing proportionally to the squared mean length. Theoretical work [94] considered simultaneous effects of surface diffusion and nucleation delay on the LDs and predicted even larger broadening than in Ref. [93]. Figure 8.4 shows the model with its main ingredients, a delayed nucleation and the diffusion flux of adatoms collected from the entire length of the NW, which equals s MLs. As a result, the instantaneous growth rates become linear in s. Such size-linear model was discussed earlier in connection with the scaling regime of growth of 2D islands competing for the diffusion flux of adatoms (see Ref. [98] and references therein).

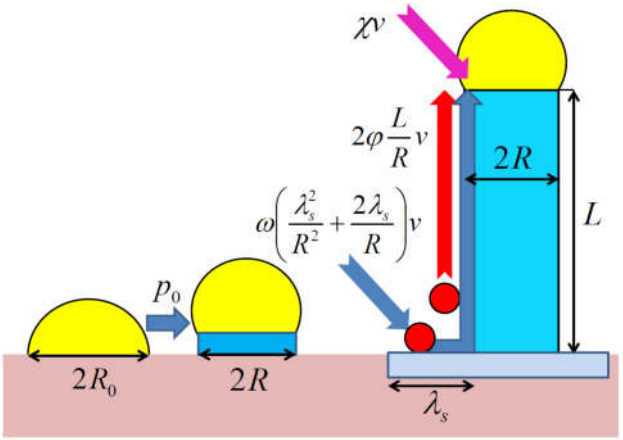

Figure 8.4. Schematics of the VLS NW growth from pre-existing Au droplets with the radius R_0. The nucleation probability of the very first NW ML equals p_0. Upon the formation of the first ML, the droplet changes its shape and the NW acquires a steady state radius R. Subsequent elongation rate of the NW contains three contributions: (i) the vapor flux χv, (ii) the diffusion flux $\omega(\lambda_s^2/R^2+2\lambda_s/R)v$ of adatoms collected by the substrate area of width λ_s and (iii) the diffusion flux $2\varphi(L/R)v$ of adatoms collected by the NW sidewalls of length $L=hs$. The χ, φ and ω are some coefficients on the order of unity. Reprinted from Journal of Crystal Growth, vol. 463, V. G. Dubrovskii, Length distributions of nanowires: effects of surface diffusion versus nucleation delay, pp. 139-144, Copyright (2017), with permission from Elsevier.

Introducing the dimensionless time τ and the model parameters a and b according to

$$\tau = \frac{2\varphi h v t}{R},\ \ a = \frac{\chi R + \omega(\lambda_s^2 / R + 2\lambda_s)}{2\varphi h},\ b = \frac{p_0 R}{2\varphi h v}, \tag{8.11}$$

with t as the growth time and other parameters illustrated in Figure 8.4, Eqs. (8.1) take the form

$$\frac{df_0}{d\tau} = -bf_0,$$

$$\frac{df_1}{d\tau} = bf_0 - (a+1)f_1,$$

$$\frac{df_s}{d\tau} = (a+s-1)f_{s-1} - (a+s)f_s,\ \ s \geq 2. \tag{8.12}$$

Here, b describes the nucleation probability of the first ML [in a different normalization compared to α in Eq. (8.7)], while a appears due to normalization of the diffusion flux (to make it equal s at $s \to \infty$). This a is usually much larger than unity due to the presence of the R/h term in the corresponding Eq. (8.11), which equals the NW radius in the units of lattice spacing.

Exact solution to Eqs. (8.12), given in Ref. [94], is expressed through the incomplete beta-function. The particular case of this LD at $a = b$ is reduced to the Polya distribution [93,94]. In the continuum limit $s >> 1$, the beta-distribution converges to

$$f(s,\tau) = \frac{be^{-\tau}}{\Gamma(a+1)}(se^{-\tau})^{b-1}\Gamma(se^{-\tau}, a-b+1), \tag{8.13}$$

with

$$\Gamma(y,q) = \int_y^\infty dt t^{q-1}e^{-t}. \tag{8.14}$$

as the upper incomplete gamma-function and $\Gamma(y)$ as the gamma-function. The mean value of such LD equals

$$\langle s \rangle = c(e^\tau - 1) \cong ce^\tau,\ \ c = \frac{(a+1)b}{(b+1)}, \tag{8.15}$$

where the approximate expression corresponds to the continuum LD. The variance of the continuum LD is given by

$$\sigma = \frac{[a+2+b(b+2)]}{(a+1)b(b+2)}\langle s\rangle^2 . \tag{8.16}$$

For $a = b$, corresponding to the case of NWs growing by surface diffusion from their entire length without nucleation delays, the mean length and variance become

$$\langle s\rangle = a(e^{\tau}-1),\ \sigma^2 = \frac{\langle s\rangle^2}{a} . \tag{8.17}$$

At $s >> a >> 1$, the continuum Polya LD is reduced to the symmetric Gaussian

$$f(s,\langle s\rangle) \cong \frac{1}{\langle s\rangle}\sqrt{\frac{a}{2\pi}}\exp\left[-\frac{a}{2}\frac{(s-\langle s\rangle)^2}{\langle s\rangle^2}\right]. \tag{8.18}$$

Figure 8.5 shows how the symmetric Polya LD transitions to much broader LDs, which are asymmetric toward their longer left tails, with increasing the nucleation delay. The LDs can even become monotonically decreasing for very difficult nucleation from the substrate ($b<1$). But even for the best case without any delays for NWs emerging from the substrate, the variance scales as $\langle s\rangle^2 / a$, leading to the extreme broadening of the LDs due to the surface diffusion effect.

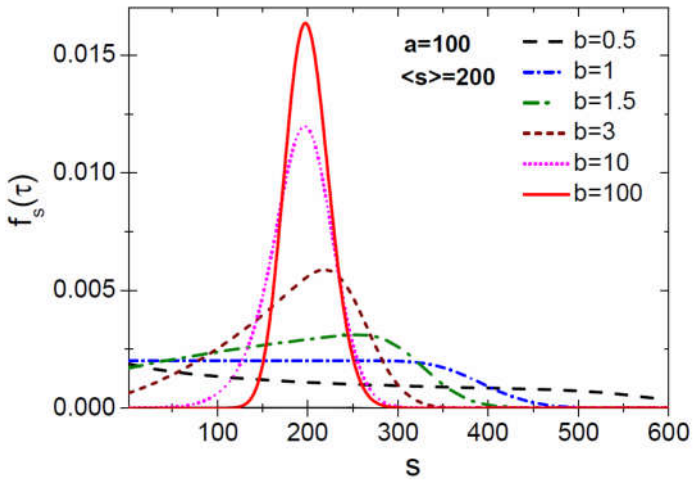

Figure 8.5. Discrete beta-distribution at a fixed a of 100, which is very well approximated by the continuum LD given by Eq. (8.13), transitioning from the symmetric Polya LD at $a = b$ to much broader and asymmetric LDs with decreasing b, and finally becoming monotonically decreasing at $b<1$. Reprinted from Journal of Crystal Growth, vol. 463, V. G. Dubrovskii, Length distributions of nanowires: effects of surface diffusion versus nucleation delay, pp. 139-144, Copyright (2017), with permission from

Elsevier.

Au-catalyzed InAs NWs of Ref. [93] were grown by MOVPE. Before MOVPE growth, patterns of Au particles were prepared by means of electron beam lithography (EBL) followed by thermal evaporation of Au and lift-off. The distance between the Au particles was 1000 nm and by varying the EBL dose the nominal NW diameter was varied between 20 and 100 nm. The NWs were grown at 450°C and the investigated growth times were 7.5, 15, 22.5, 30, and 60 min. SEM images of the NW arrays were recorded at the specific tilt angles and NW length and diameter statistics were extracted using the SEM image analysis. Figure 8.6 shows the typical SEM images of differently sized InAs NWs after 7.5 min of growth. It is clearly seen that the NW length decreases for larger diameters, which confirms that their VLS growth is controlled by surface diffusion of In adatoms.

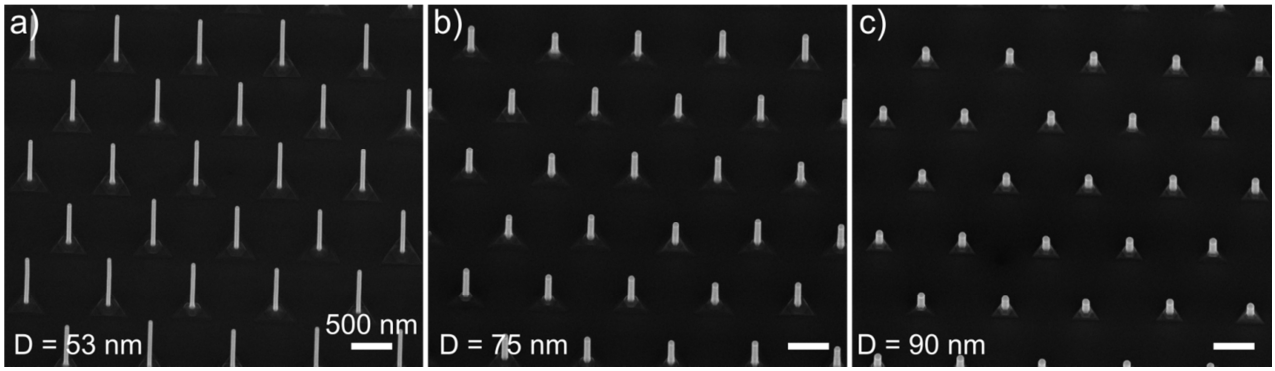

Figure 8.6. 30^{o} tilted SEM images of InAs NW arrays with 1000 nm pitch, growth time of 7.5 min and NW diameters around (a) 53 nm, (b) 75 nm, and (c) 90 nm. Scale bar is the same in all three images. Reprinted with permission from V. G. Dubrovskii, Y. Berdnikov, J. Schmidtbauer, M. Borg, K. Storm, K. Deppert, J. Johansson, Length distributions of nanowires growing by surface diffusion, Crystal Growth & Design **16**, 2167-2172 (2016). Copyright (2016) American Chemical Society.

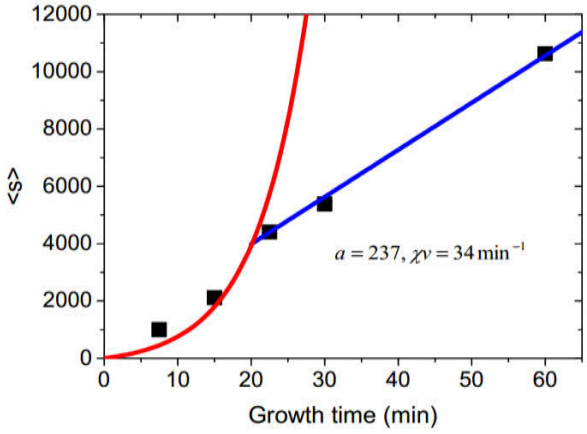

Figure 8.7. Transition from the exponential to linear growth regime of the 100-110 nm diameter InAs NWs (symbols), the fitting parameters in Eq. (8.19) for the lines are: $a = 237$, $\chi v = 34$ mim^{-1} and $C = 0.247$. Reprinted with permission from V. G. Dubrovskii, Y. Berdnikov, J. Schmidtbauer, M. Borg, K. Storm, K. Deppert, J. Johansson, Length distributions of nanowires growing by surface diffusion, Crystal Growth & Design **16**, 2167-2172 (2016). Copyright (2016) American Chemical Society.

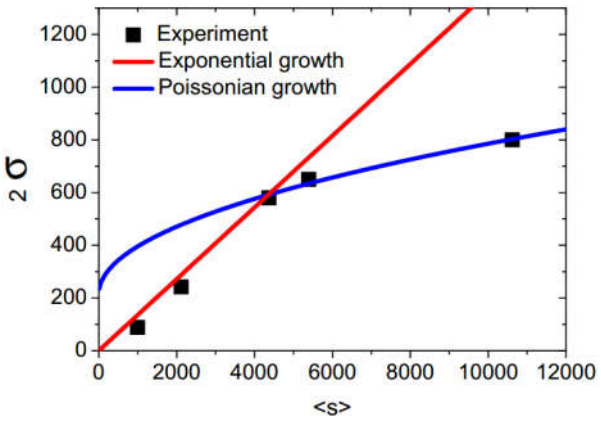

Figure 8.8. Best fits by Eqs. (8.19) (lines) of the experimental standard deviations of the 100-110 diameter NW LDs (symbols) versus the mean length at different growth times. Reprinted with permission from V. G. Dubrovskii, Y. Berdnikov, J. Schmidtbauer, M. Borg, K. Storm, K. Deppert, J. Johansson, Length distributions of nanowires growing by surface diffusion, Crystal Growth & Design **16**, 2167-2172 (2016). Copyright (2016) American Chemical Society.

Figures 8.7 and 8.8 show the measured mean length $\langle s \rangle$ and LD width 2σ (expressed in MLs) of 100-110 nm diameter NWs. It is seen that the mean length increases exponentially with the growth time for $t < 22.5$ min and linearly for longer times. The standard deviation is proportional to the mean length for $t < 22.5$ but becomes sub-linear for longer times. Such changes are attributed to the transition from the length-linear to length-independent NW growth rates, as discussed previously. Therefore, these data were fitted with

$$\langle s \rangle = s_{\max} + \left(1 + \frac{s_{\max}}{a}\right) C\chi v (t - t_{\max}); \quad \sigma^2 = < s > - s_{\max}. \tag{8.19}$$

Here, $t_{\max}$ is the time at which the mean NW length reaches the diffusion length $s_{\max}$ (4400 MLs, or about 1500 nm according to Figure 8.7) and C is a constant deduced from the fit.

The solution for the NW LDs at $t > t_{\max}$ is then obtained by convoluting the two Gaussians representing the Poissonian Green function and the Polya LD at $t = t_{\max}$, given by Eq. (8.18). The resulting LD has the form

$$f(s,\langle s\rangle) \cong \frac{1}{\sqrt{2\pi}\sigma}\exp\left[-\frac{\left(s-\langle s\rangle\right)^2}{2\sigma^2}\right], \qquad \sigma^2 = \begin{cases} \dfrac{\langle s\rangle^2}{a}, \langle s\rangle \le s_{\max} \\ \dfrac{s_{\max}^2}{a} + < s > -s_{\max}, < s > \ge s_{\max} \end{cases}.$$

(8.20)

This solution holds for any $< s >$, while the mean length is given by Eq. (8.17) in the exponential stage until $\langle s\rangle < s_{\max}$ and by the corresponding Eq. (8.19) when $\langle s\rangle > s_{\max}$. Since no difference in the growth rate of very short NWs was noticed, the diffusion flux from the substrate was neglected. From Eq. (8.11), this gives $a = \chi R/(2\varphi h)$, showing that a scales as R.

Figure 8.9 shows the experimental LDs and their best fits by Eq. (8.20) for NWs with different diameters grown for the same time of 7.5 min. The fitting values of a indeed scale linearly with the NW diameter, as predicted by the model [93]. It is noteworthy that the fits are obtained with rather high $a \ge 140$. This is not surprising because the a parameter contains a large value of R/h in the range of 140-300, while the coefficient $\chi/(2\varphi)$ is expected to be of the order of one. This confirms the assumption $\langle s\rangle >> a >> 1$, which allows us to use the Gaussian LD given by Eq. (8.18) instead of the exact solution for the discrete LD. Figure 8.10 shows the experimental LDs and their Gaussian fits for NWs of 100-110 nm diameter at different growth times. The mean length and width of these LDs are given in Figures 8.7 and 8.8. The fits are obtained with the same $a = 237$ for each growth time, which again confirms the validity of the model. One of the main conclusions is that the LDs acquire the broad Polya-like shape already at the initial stage of growth, in which In adatoms are collected from the entire NW length. Therefore, the VLS growth regimes controlled by the diffusion transport of group III adatoms are not desirable for obtaining sharp NW LDs.

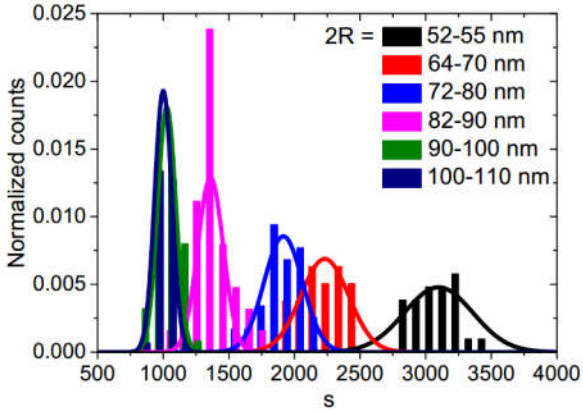

Figure 8.9. Normalized experimental LDs (histograms) of differently sized InAs NWs grown for 7.5 min. The data for 52-55, 64-70, 72-80, 82-90, 90-100 and 100-110 nm diameter NWs are fitted by Eq. (8.20) (lines) with $a = 140$, $< s >= 3098$, $a = 160$ $< s >= 2231$ MLs, $a = 180$, $\langle s \rangle = 1915$ MLs, $a = 200$, $\langle s \rangle = 1472$ MLs, $a = 220$, $\langle s \rangle = 1027$ MLs, and $a = 237$, $\langle s \rangle = 1000$ MLs, respectively. For this growth time, all the LDs are Polya-like because the mean length is shorter than $s_{max} = 4400$ MLs. Reprinted with permission from V. G. Dubrovskii, Y. Berdnikov, J. Schmidtbauer, M. Borg, K. Storm, K. Deppert, J. Johansson, Length distributions of nanowires growing by surface diffusion, Crystal Growth & Design **16**, 2167-2172 (2016). Copyright (2016) American Chemical Society.

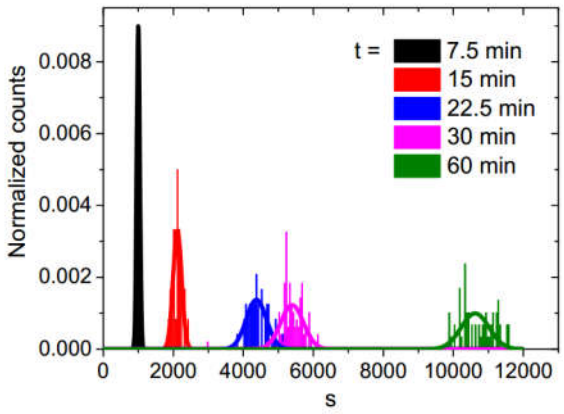

Figure 8.10. Broadening of the LD of 100-110 nm diameter InAs NWs with the growth time: experimental LDs (histograms), fitted by the Gaussian distributions (lines) with $a = 237$ and $\langle s \rangle$ = 1000, 2110, 4400, 5400, and 10600 MLs for the growth times of 7.5, 15, 22.5, 30, and 60 min, respectively. Reprinted with permission from V. G. Dubrovskii, Y. Berdnikov, J. Schmidtbauer, M. Borg, K. Storm, K. Deppert, J. Johansson, Length distributions of nanowires growing by surface diffusion, Crystal Growth & Design **16**, 2167-2172 (2016). Copyright (2016) American Chemical Society.

To this end, we have discussed different mechanisms of broadening the Poisson LDs of NWs. Let us now see if it is possible to achieve sub-Poissonian narrowing of the LDs. The only effect which is expected to be beneficial from this perspective is nucleation antibunching observed experimentally and explained theoretically in Ref. [88]. Using the method described in Section 6 for $InP_{1-x}As_x$ NWs with modulated composition, the nucleation statistics in individual NW was analyzed as shown in Figure 8.11. The length of each oscillation of composition in an individual NW is measured to within 1 ML [Figure 8.11 (a)]. In the mononuclear growth regime,

the NW axial growth rate is fixed by the rate of nucleation at the catalyst-solid interface and the number of MLs grown equals the number of nucleation events. The length of each oscillation (in MLs) thus equals the number of nucleation events in the time period Δt. If these nucleation events occurred independently of each other, the probability of a given number m of nucleations taking place during Δt should follow the Poisson statistics. Figure 8.11 (b) compares the distribution of the oscillation lengths with a Poisson distribution, normalized to the same total number of oscillations. The nucleation statistics are markedly sub-Poissonian. In three NW segments studied (see Ref. [88] for the details), the measured standard deviations are less than half the Poisson standard deviations. This proves that the nucleation events are not independent.

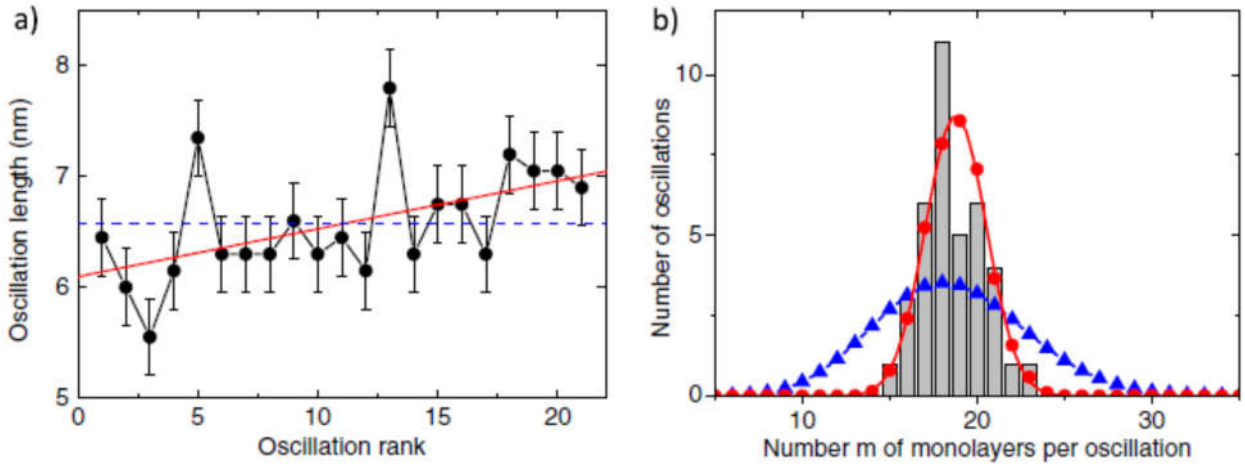

Figure 8.11. (a) Length of successive oscillations. The dashed line gives the mean length; the solid line is a linear regression $dL/dt \propto t$. (b) Histogram of the numbers of nucleation events per oscillation. The two curves represent distributions calculated for a large number of nucleation events and normalized to the total number of experimental counts: Poissonian statistics (triangles), self-regulated statistics (disks). Reprinted figure with permission from F. Glas, J. C. Harmand and G. Patriarche, Physical Review Letters **104**, 135501 (2010), https://doi.org/10.1103/PhysRevLett.104.135501. Copyright (2010) by the American Physical Society.

This effect was explained by nucleation antibunching, whereby the probability to nucleate the next ML decreases exponentially immediately after nucleation of the previous ML [88]. Therefore, the next nucleation event becomes improbable until the droplet is refilled from vapor with the missing As. The measure of nucleation antibunching is readily obtained from the

following considerations. The chemical potential decrease immediately after nucleation of one ML equals

$$\delta\Delta\overline{\mu} = c_5 \frac{\partial\Delta\overline{\mu}}{\partial c_5}(1-2c_5)\frac{1}{N_5}\frac{\pi R^2}{\Omega_S}. \tag{8.21}$$

Approximating the nucleation barrier under the exponent of the Zeldovich nucleation rate [Eq. (3.11)] as

$$\frac{a^2}{4(\Delta\overline{\mu}-\delta\Delta\overline{\mu})} \cong \frac{a^2}{4\Delta\overline{\mu}} + \frac{a^2}{4\Delta\overline{\mu}^2}\delta\Delta\overline{\mu} \tag{8.22}$$

and using Eq. (3.8) for the critical size i_c, we note that the decrease in the nucleation probability immediately after nucleation equals $\exp(-\varepsilon)$, with

$$\varepsilon = c_5 \frac{\partial\Delta\overline{\mu}}{\partial c_5}(1-2c_5) i_c(\Delta\overline{\mu})\frac{1}{N_5}. \tag{8.23}$$

This ε is called the antibunching parameter in what follows. It can equivalently be presented in the form

$$\varepsilon = \frac{3\widetilde{\Omega}_L}{f(\beta)\Omega_S} c_5 \frac{\partial\Delta\overline{\mu}}{\partial c_5} i_c(\Delta\overline{\mu})\frac{h}{c_5 R}. \tag{8.24}$$

In these expressions, the chemical potential, its derivative with respect to c_5, and c_5 itself should be taken before nucleation. Clearly, the antibunching effect is stronger for thinner NWs and low group V concentrations in the droplet (small R and c_5), and disappears at large R. As an example, ε equals 0.2 for <111> GaAs NWs ($\widetilde{\Omega}_L = 0.02\,\text{nm}^3$, $\Omega_S = 0.0452\,\text{nm}^3$, $h = 0.326$ nm) with $R =$ 50 nm and $\beta = 127^\text{o}$ if we assume $\overline{c}(\partial\Delta\mu/\partial\overline{c}) = 1$, $\overline{c} = 0.03$ and $i_c(\Delta\overline{\mu}) = 5$.

Glas [99] presented the exact solution for sub-Poissonian nucleation statistics in individual VLS NWs, controlled by the sole parameter ε. Later, Glas and Dubrovskii [95] considered the effect of nucleation antibunching on the LDs within the ensembles of NWs by using three different methods: (i) numerical simulations in a large ensemble of NWs, (ii) exact analytical solution for the LD and its statistical properties based on the results obtained for

individual NW [99], and (iii) simplified analytic approach based on the continuum rate equation. The main goal was to obtain the LD as a function of two parameters, ε for antibunching and $\alpha = p_0 / v$ for the nucleation delay, assuming the NW nucleation rate in the form of exponential decay $p_0 \exp(-p_0 t)$ as discussed earlier.

For the exact analytical calculations, the central object is the probability $\pi_s(T|p_I)$ that exactly *s* nucleations occur during a time interval of length *T*, conditional to the fact that the NP was p_I at the beginning of this interval. According to Ref. [99], $\pi_s(T|p_I)$ is given by

$$\pi_s(T|p_I) = \sum_{m=0}^{s} \frac{g_{s-m}}{(\gamma;\gamma)_m} \exp[\quad \gamma^m E(T) p_I/(\varepsilon v)] \,. \tag{8.25}$$

Here, $\gamma = \exp(-\varepsilon)$, $(\gamma;\gamma)_m = (1 \quad \gamma)(1 \quad \gamma^2) \ldots (1 \quad \gamma^m)$ is the q-Pochhammer symbol (for $m \geq 1$, with $(\gamma;\gamma)_0 = 1$), $g_m = (\quad 1)^m \gamma^{\frac{m(m-1)}{2}} / (\gamma;\gamma)_m$, and $E(T) = \mathrm{e}^{\varepsilon v T} \quad 1$. The probability p_I corresponds to the beginning of growth, just after forming the first ML of the NW (the third parameter which is not required in the continuum theory).

The conditional probability $\pi_s(T|p_I)$ is a powerful tool for calculating the time evolution of ensembles of NWs. Indeed, the ensemble LD is simply given by the convolution of this probability with the distribution of times of formation of the first ML, which equals $p_0 \exp(-p_0 T)$. After some calculations (see Ref. [95] for the details), the LD can be expressed in terms of the incomplete gamma functions $\Gamma(x, y)$ as

$$f_s(\tau) = \theta \rho^{-\theta} \sum_{m=0}^{s-1} \frac{g_{s-1-m}}{(\gamma;\gamma)_m} \exp[\alpha(m \quad \tau) + \rho e^{-m\varepsilon}] \left[\Gamma\left(\theta, \rho e^{\varepsilon(\tau - m)}\right) \quad \Gamma(\theta, \rho e^{-\varepsilon m}) \right] \tag{8.26}$$

for $s \geq 1$, with $\theta = \varepsilon^{-1}\alpha = \varepsilon^{-1} p_0 / v$, $\rho = \varepsilon^{-1} p_I / v$ and $\tau = vT$ as the normalized growth time. These formulas are exact for any values of parameters $\neq 0$, α , p_I and time τ and are computationally efficient unless ε is very small. The LDs so calculated agree extremely well with those obtained from numerical simulations [95]. This confirms that for identical and non-interacting NWs, the statistics of the ensemble may be calculated from those of the single NW.

The average length (in MLs) of the NW ensemble at time τ equals

$$s = (\gamma;\gamma)_\infty \sum_{m=0}^{\infty} \frac{1}{(\gamma;\gamma)_m} \{1 - e^{-\alpha\tau} - \theta\rho^{-\theta}\exp[\alpha(m - \tau) + \rho e^{-m\varepsilon}] [\Gamma(\theta, \rho e^{\varepsilon(\tau-m)}) - \Gamma(\theta, \rho e^{-\varepsilon m})]\} + 1 - e^{-\alpha\tau}. \quad (8.27)$$

The variance of the LD is given by

$$\sigma^2 = 2(\gamma;\gamma)_\infty \sum_{m=0}^{\infty} \frac{m - \Phi(\gamma)}{(\gamma;\gamma)_m} \{1 - e^{-\alpha\tau} - \theta\rho^{-\theta}\exp[\alpha(m - \tau) + \rho e^{-m\varepsilon}] [\Gamma(\theta, \rho e^{\varepsilon(\tau-m)}) - \Gamma(\theta, \rho e^{-\varepsilon m})]\} + 3 s - s^2 - 2(1 - e^{-\alpha\tau}), \quad (8.28)$$

where $\Phi(\gamma) = \sum_{p=1}^{\infty} \gamma^p/(1 - \gamma^p)$ is the Lambert series with unit coefficients. It turns out that the parameter p_1 has no influence on the LDs of sufficiently long NWs of interest, so the statistical properties of the ensemble are controlled by the two parameters ε and α.

In the continuum approach, the asymptotic method of Ref. [100] was used, which formally requires $\varepsilon << 1$. The instantaneous growth rates in the continuum Eq. (8.2) for $s >> 1$ were taken in the form

$$p_s(t) = p(vt - s) = ve^{\varepsilon(vt-s)}, \quad (8.29)$$

describing the exponential growth of the nucleation probability with time due to incoming flux and its exponential decrease immediately after the ML formation. Green's function of Eq. (8.2) is obtained in the form

$$F(\rho, z) = \frac{1 + \varepsilon\rho}{\sqrt{2\pi}\sigma} \exp\left[-\frac{(\rho - z)^2}{2\sigma^2}\right], \quad (8.30)$$

with

$$\rho = \frac{e^{\varepsilon s} - 1}{\varepsilon}, \; z = \frac{e^{\varepsilon\tau} - 1}{\varepsilon}, \; \sigma^2 = z + \frac{\varepsilon z^2}{2}. \quad (8.31)$$

This solution is quite interesting as it combines the Poissonian LD at $\varepsilon \to 0$ with self-regulated LD at $\varepsilon > 0$. In the latter case, Green's function becomes a universal function of $s - \tau$:

$$F(s-\tau)=\sqrt{\frac{\varepsilon}{\pi}}e^{\varepsilon(s-\tau)}\exp\left[-\frac{1}{\varepsilon}\left(e^{\varepsilon(s-\tau)}-1\right)^2\right]. \tag{8.32}$$

This property directly shows that Green's function does not broaden with time due to nucleation antibunching. For small enough ε and large s, it is well approximated by the Gaussian

$$F(s-\tau)=\sqrt{\frac{\varepsilon}{\pi}}\exp\left[-\varepsilon(s-\tau)^2\right] \tag{8.33}$$

Clearly, the mean length of this LD remains τ but the variance is time-independent and equals $1/(2\varepsilon)$ rather than growing infinitely as in the Poissonian case. The variance $1/(2\varepsilon)$ exactly equals the one obtained in Ref. [99] for individual NW.

Convolution of Green's function given by Eq. (8.33) with the nucleation rate $J(\tau)=\alpha\exp(-\alpha\tau)$ according to Eq. (8.3) yields the asymptotic LD in the form

$$f(s-\tau)=\frac{\alpha}{2}e^{\alpha(s-\tau)+\alpha^2/(4\varepsilon)}\operatorname{erfc}\left[\sqrt{\varepsilon}(s-\tau)+\frac{\alpha}{2\sqrt{\varepsilon}}\right]. \tag{8.34}$$

This universal LD depends only on the difference $x=s-\tau$ and hence its shape does not change with time. The mean length and variance of the fully formed LD given by Eq. (8.34) equal

$$\langle s\rangle=\tau-\frac{1}{\alpha},\quad \sigma^2=\frac{1}{2\varepsilon}+\frac{1}{\alpha^2}. \tag{8.35}$$

It is interesting to note that the Poissonian growth with nucleation delay can be resumed from these results by setting $\varepsilon=1/(2\tau)$, which transforms Eqs. (8.34) and (8.35) to Eqs. (8.8) and (8.10), respectively.

Figure 8.12 shows how the universal LD $f(x)$ at a fixed ε of 0.1 is broadened for smaller α, corresponding to longer NW nucleation delays. Figure 8.13 shows the narrowing of the LDs due to increasing the antibunching parameter ε, at a given $\alpha=0.07$. This effect is stronger for smaller ε, while for larger ε the LDs converge to a shape that is simply determined by the duration of the NW nucleation step. In both figures, the excellent quantitative

agreement is obtained between the exact LDs given by Eq. (8.26) and the continuum LD given by Eq. (8.34).

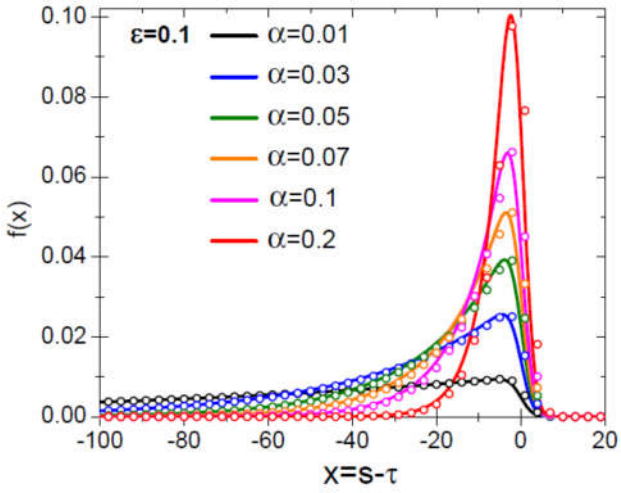

Figure 8.12. Shapes of the universal LD at a fixed $\varepsilon = 0.1$ and different α ranging from 0.01 to 0.2. Lines: continuum approximation [Eq. (8.34)]. Symbols: exact solution [Eq. (8.26)], for $p_s = v$. Reprinted figure with permission from F. Glas and V. G. Dubrovskii, Physical Review Materials **1**, 036003 (2017), https://doi.org/10.1103/PhysRevMaterials.1.036003. Copyright (2017) by the American Physical Society.

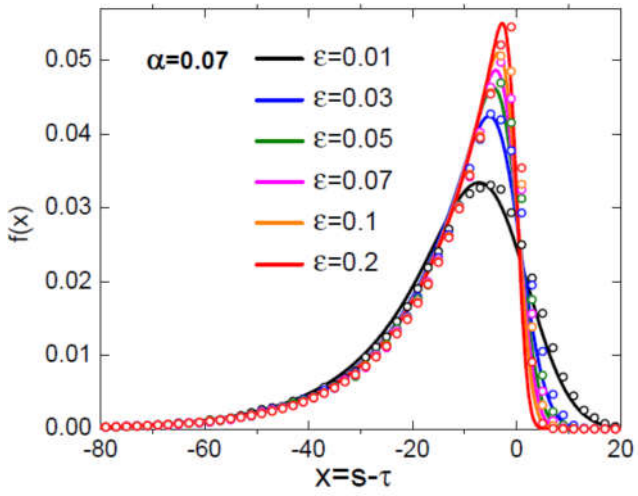

Figure 8.13. Shapes of the universal LD at a fixed $\alpha = 0.07$ and different ε ranging from 0.01 to 0.2. Lines: continuum approximation [Eq. (8.34)] Symbols: exact solution for $p_s = v$, using Eq. (8.26) for $\varepsilon \geq 0.1$ and numerical simulation for $\varepsilon \leq 0.07$. Reprinted figure with permission from F. Glas and V. G. Dubrovskii, Physical Review Materials **1**, 036003 (2017), https://doi.org/10.1103/PhysRevMaterials.1.036003. Copyright (2017) by the American Physical Society.

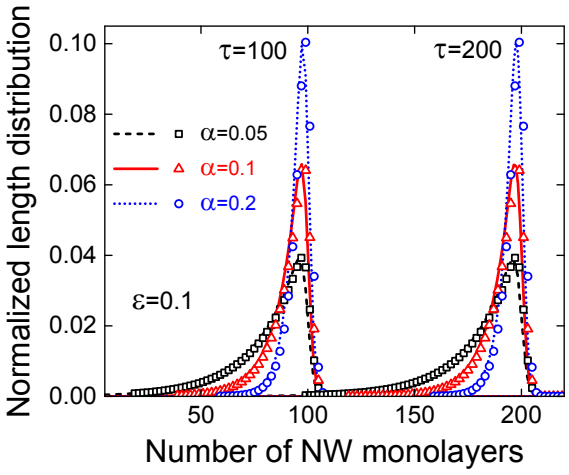

Figure 8.14. Discrete (symbols) and continuum (lines) LDs obtained from Eq. (8.26) and Eq. (8.34),

respectively, for two different growth times and three different values of α (0.05, 0.1 and 0.2), at a fixed $\varepsilon = 0.1$ and for $p_s = v$ in Eq. (8.26). Reprinted figure with permission from F. Glas and V. G. Dubrovskii, Physical Review Materials **1**, 036003 (2017), https://doi.org/10.1103/PhysRevMaterials.1.036003. Copyright (2017) by the American Physical Society.

Figure 8.14 shows the comparison between the LDs obtained from discrete Eq. (8.26) and continuum Eq. (8.34) and demonstrates again their excellent quantitative correlation. The LD shapes are almost identical; however, the continuum LDs are slightly shifted toward smaller lengths. This is explained by the fact that in the continuum approximation, the NWs are assumed to emerge with zero length while actually they nucleate with a minimum length of 1 ML. The variances of the LDs obtained numerically as the long time asymptotics to the exact Eq. (8.28) and from Eq. (8.35) are also extremely close (see Ref. [95] for a more detailed discussion).

Summarizing the results of Ref. [95], it was demonstrated by three different methods that nucleation antibunching in individual NWs, described by the antibunching parameter ε, completely suppresses the Poissonian broadening of LDs within ensembles of NWs. The initial nucleation randomness, described by the parameter α, affects the LDs forever, which is why the asymptotic variances and the LD shapes depend on the two parameters ε and α. However small these parameters may be, the LDs finally acquire time-independent shapes rather than spread infinitely with the growth time. Numerical simulations over large ensembles of NWs and two different analytical approaches based on discrete and continuum rate equations yield very similar results. Recent experimental results confirm qualitatively these predictions by showing markedly sub-Poissonian LDs of Ga-catalyzed GaAs NWs [30,31]. However, quantitative comparison with these data requires some care. In theoretical analysis, we used a time-independent antibunching parameter throughout the entire growth process, while the GaAs NWs of Ref. [30] grow also in diameter, which affects the ε value according to Eq. (8.24). In addition, we assumed a time-independent nucleation probability for forming the first NW ML. This corresponds to the VLS regimes with long incubation times for NW growth (small α). Surface diffusion effects may

affect the described picture, which seems more relevant for self-catalyzed III-V NWs. All these questions require further studies.

We now present one example of sub-Poissonian LDs observed in ensembles of self-catalyzed GaAs NWs [30] (more examples are given in Ref. [31]). Ga-catalyzed GaAs NWs of Ref. [30] were grown by MBE on p-Si(111) substrates by the procedure which is presented step-by-step in Figure 8.15. Before the first growth step, the Si(111) substrates were dipped in HF in order to remove the native oxide and immediately transferred to vacuum where they were first annealed at 275 °C for 1 h and then at 700 °C for 10 min. Then GaAs nanocrystals were grown by droplet epitaxy; (1) Ga droplets were first formed by depositing 0.09 MLs of Ga at 550 °C and then (2) crystallized into GaAs by a 10 min As_2 exposure. The sample temperature in step 1 is a critical parameter that defines the density of the nucleation sites. In step 3, the sample was removed from vacuum and exposed to air for 18 h in order to form an oxide layer on the Si(111) surface. In the following step (4), the sample was transferred back to vacuum where it was annealed at 660 °C for 30 min in order to remove the GaAs nanocrystals and reveal oxide free nucleation sites. In the final surface preparation steps (5) Ga droplets were formed in the nucleation sites by depositing Ga for 60 s at 640 °C using a growth rate of 0.3 ML/s, and (6) subsequently removed by annealing at 660 °C for 10 min. The purpose of steps 5 and 6 is to prepare the nucleation sites for subsequent NW growth. By introducing these additional steps to the process presented in Ref. [101], a high vertical yield of 70% is obtained, without having to use Ga pre-deposition at the beginning of the NW growth. Finally, in step (7) the NW growth was initiated by simultaneously opening the Ga shutter and As valve and using sample temperature of 640 °C. The Ga growth rate was 0.3 ML/s and As_2/Ga flux ratio 9. The NW samples were grown using different growth durations: 3 min, 6 min, 20 min, 40 min, 50 min, and 80 min. The 50 min sample was grown on a template having nucleation site density of 2×10^8 cm^{-2} while a slightly higher density of 4×10^8 cm^{-2} was used for the other samples, resulting in NW densities of 0.7×10^8 cm^{-2} and 1.5×10^8 cm^{-2}, respectively.

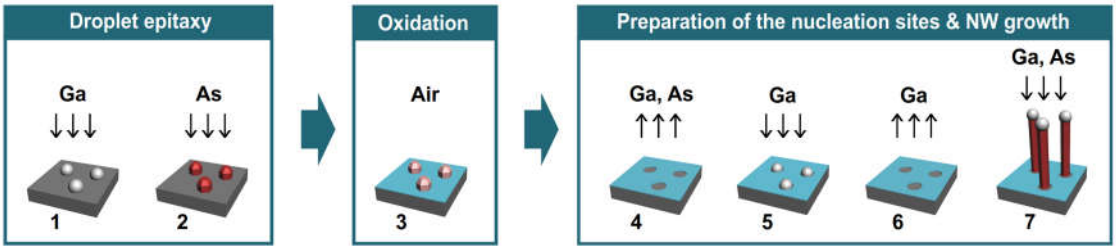

Figure 8.15. Description of the NW growth process. Steps 1 and 2: formation of GaAs nanocrystals on oxide-free Si(111) by droplet epitaxy; Step 3: spontaneous oxidation of the Si surface by air exposure; Step 4: removal of the GaAs nanocrystals by annealing; Steps 5 and 6: formation of Ga droplets inside the holes and subsequent evaporation of the Ga droplets by annealing; Step 7: Ga-catalyzed NW growth. Reprinted with permission from E. S. Koivusalo, T. V. Hakkarainen, M. Guina and V. G. Dubrovskii, Sub-Poissonian narrowing of length distributions realized in Ga-catalyzed GaAs nanowires, Nano Letters **17**, 5350-5355 (2017). Copyright (2017) American Chemical Society.

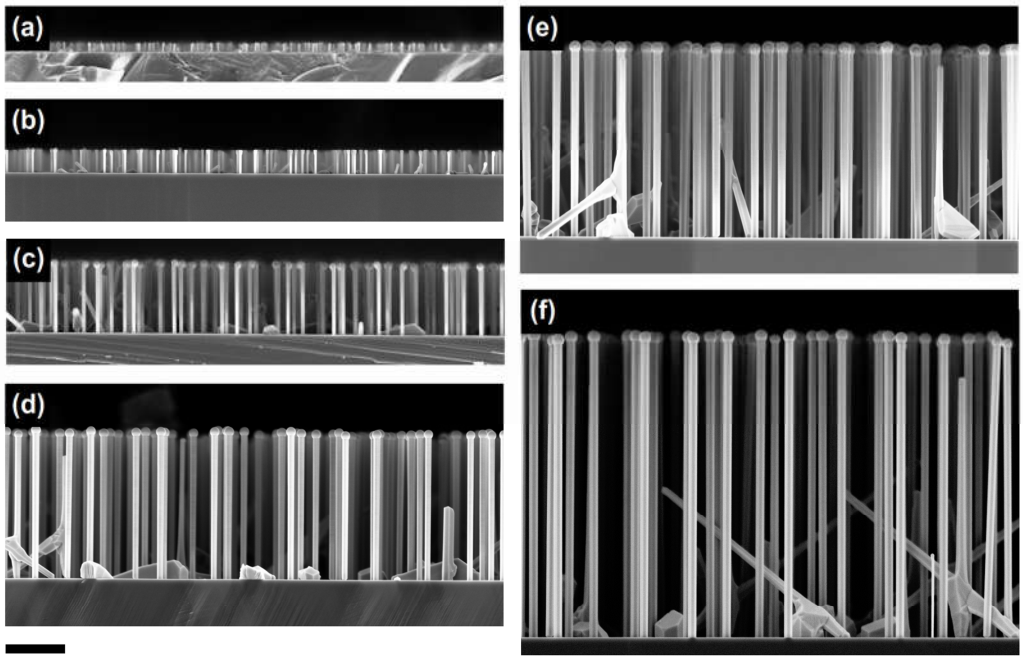

Figure 8.16. Cross-sectional SEM images of Ga-catalyzed GaAs NWs grown for 3 min (a), 6 min (b), 20min (c), 40 min (d), 50min (e), and 80 min (f). Scale bar is 1 µm. Reprinted with permission from E. S. Koivusalo, T. V. Hakkarainen, H. V. A. Galeti, Y. G. Gobato, V. G. Dubrovskii and M. D. Guina, Deterministic switching of the growth direction of self-catalyzed GaAs nanowires, Nano Letters **19**, 82-89 (2019). Copyright (2019) American Chemical Society.

Figure 8.16 shows cross-sectional SEM images of the NWs after different growth durations. It is evident from the SEM images that the NWs obtained by this method remain

remarkably uniform throughout the growth process from 3 min up to 80 min growth duration. Statistical analysis shows the linear time dependence of the NW length, with the axial growth rate V of 62.8 nm/min. The NW diameter increases first linearly and then saturates as the NW length increases, probably reaching the stable diameter as described in Section 7. The measured LDs of these NWs after different growth times remain surprisingly narrow as shown in Fig. 8.17, particularly for longer growth times. The mean NW length is given by $\langle L \rangle = Vt$, with V = 62.8 nm/min as the effective influx of As. The measured LDs after 40, 50 and 80 min of growth are markedly sub-Poissonian, as shown in Fig. 8.18. For example, the variance of 2480 nm long NWs obtained after 40 min of growth is only 367 nm^2, which is more than twice smaller than the Poisson variance

$$\sigma_P^2 = h\langle L \rangle \tag{8.36}$$

of 808 nm^2 for this mean length.

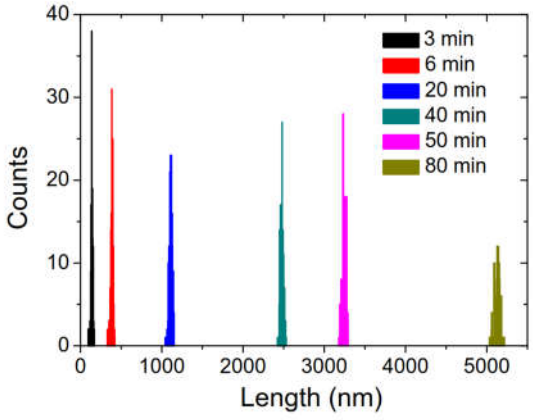

Figure 8.17. Measured length histograms of Ga-catalyzed GaAs NWs at t = 3, 6, 20, 40, 50 and 80 min. Reprinted with permission from E. S. Koivusalo, T. V. Hakkarainen, H. V. A. Galeti, Y. G. Gobato, V. G. Dubrovskii and M. D. Guina, Deterministic switching of the growth direction of self-catalyzed GaAs nanowires, Nano Letters **19**, 82-89 (2019). Copyright (2019) American Chemical Society.

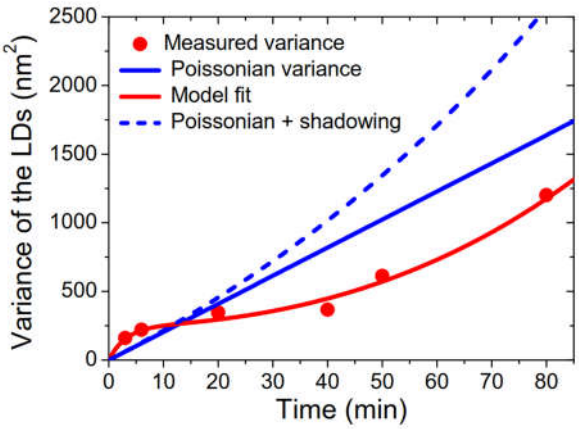

Figure 8.18. Measured variance of the GaAs NW LDs versus the growth time (symbols). Solid linear line shows the corresponding Poisson variance $\sigma_P^2 = h\langle L \rangle = hVt$, with V = 62.8. The red line shows theoretical fit by Eq. (8.37) which includes the shadowing effect. The dashed blue line corresponds to the Poissonian growth with shadowing. Reprinted with permission from E. S. Koivusalo, T. V. Hakkarainen, H. V. A. Galeti, Y.

G. Gobato, V. G. Dubrovskii and M. D. Guina, Deterministic switching of the growth direction of self-catalyzed GaAs nanowires, Nano Letters **19**, 82-89 (2019). Copyright (2019) American Chemical Society.

It is clear from Fig. 8.18 that the LD variance first increases with time, then almost saturates at the sub-Poissonian value and starts to increase again for longer NWs, remaining, however, sub-Poissonian even for ~ 5200 nm long NWs. The model of Ref. [30] thus assumed (i) the initial nucleation-induced broadening of the LD induced by random nucleation from the substrate surface, (ii) the complete suppression of the fluctuation-induced broadening by nucleation antibuncing, and (iii) additional broadening due to the shadowing effect, which becomes important for longer NWs. Broadeing of the LDs by partial shadowing of the As flux, including re-emitted flux, can be understood simply from the fact that longer NWs are less shadowed and hence grow faster, while shorter NWs are more shadowed and grow slower than the longer ones. As a result (see Ref. [30] for the details), the model expression for the variance is given by

$$\sigma^2 = \sigma_*^2\left(1 - e^{-\langle L\rangle/L_*}\right) + hL_0\left(e^{\langle L\rangle/L_0} - 1 - \langle L\rangle/L_0\right). \tag{8.37}$$

This equation shows that, in the absence of Poissonian broadening, the length variation is determined by the two factors – the initial nucleation randomness of the NWs emerging from the substrate (leading asymptotically to the time-independent variance σ_*^2 with the characteristic saturation length L_*) and the additional broadening due to the shadow effect (which becomes important for long NWs having the mean length on the order of the shadowing length L_0).

The line in Fig. 8.18 demonstrates the excellent fit to the measured variance obtained from Eq. (8.37) with $\sigma_*^2 = 250$ nm^2, $L_* = 200$ nm and $L_0 = 6000$ nm. The dashed line in Fig. 8.18 corresponds to the Poissonian growth influenced by the shadow effect, with the same L_0 of 6000 nm and shows that the LDs without nucleation antibunching would be even broader than

Poissonian in this case. Saturation of the variance in the intermediate growth stage requires that the nucleation step is fast (a short L_*) and the shadowing length L_0 is large. The nucleation variance σ_*^2 depends on the preparation technique used for Ga droplets, the type of the substrate/oxide and the nucleation rate of stable NWs emerging from Ga droplets which may be changed by the As flux. In comparison to the previous work [101], by eliminating the Ga pre-deposition step in the beginning of the NW growth we were able to reduce the incubation time and significantly reduce the saturation level of the variance.

Overall, the results presented in this Section and in Section 7 suggest that remarkable size uniformity can be achieved within the ensembles of III-V NWs, particularly those obtained in the self-catalyzed approach. Together with a tremendous progress in growing such NWs on Si substrates, and introducing high quality heterostructures in NWs, this may open a new path for monolithically integrated NW-based photonic devices and optoelectronic circuits, with a high degree of NW ordering in terms of both radii and length.

9. Semiconductor alloys in nanowires

9.1. Introduction

In the field of planar (2D) epitaxial structures, it is well known that the range of possible applications is vastly extended by using alloys instead of pure elemental semiconductors or simple stoichiometric binary III-V or II-VI compounds. This allows one to access band gap energies intermediate between those of the end components of the alloy. Moreover, in the frequent case where alloy composition variations induce changes of lattice parameter, one can play on the strain exerted by a substrate or by various parts of an heterostructure on each other to tune further the electronic and optical properties of the alloys. In this respect, the 1D geometry has two important consequences that distinguish NWs from planar structures: first, because of strain relaxation at the free sidewalls, one can associate without creating extended defects, materials that are much more lattice-mismatched than would be possible in the 2D case; second,

the strain fields are generally less homogeneous and more complex. These points will be treated in section 10.

Many semiconductor alloys have been fabricated in the form of NWs. This includes alloys between group IV elements, primarily Si-Ge [102] but also Ge-Sn [103], and many III-V and II-VI ternary and even quaternary alloys (for an overview, see e.g. Ref. [104]). The aim may be to obtain fully or locally homogeneous NWs, or else to create a controlled composition gradient along the axis. Alloys may also form unwantedly when growth fluxes are switched to form an axial heterostructure between nominally non-alloyed sections (e.g. Si_xGe_{1-x} forms at the interface between pure Si and pure Ge sections) or when, despite steady growth conditions, the relative influx of the various components changes with time (for instance because of different diffusion lengths).

Quite generally, the major question is that of the dependence of the alloy composition on the growth conditions, which here include, in addition to what we considered before, the growth fluxes of all the elements that are alloyed in the NW (or at least their ratios). Alloys may form in NW shells but these grow in the vapor-solid mode, whereas we concentrate on VLS growth. A key point is then to describe theoretically the relationship between liquid and solid compositions. This in turn is an essential step in the modeling of the effect of the growth conditions (fluxes and temperature) on the solid formed; however, this all-important question requires in addition the description of how the liquid droplet is fed by the external fluxes, which is in itself a complicated question (see section 1.4).

9.2. Description of the vapor, liquid and solid phases

For each phase ϕ, the number n_ϕ of constituents must be distinguished from the number of independent compositional parameters i_ϕ required to describe the thermodynamic state of this phase. Usually, $n_V = n_S$, since each element of the solid is provided by a separate vapor flux, be it single atoms or molecules. For self-catalyzed III-V growth, $n_L = n_S$ but $n_L > n_S$ when a

foreign catalyst is used. The vapor state is characterized by fluxes or partial pressures, so that in general $i_V = n_V$ (3 for self-catalyzed growth of ternary alloys, 2 for Ge_xSi_{1-x}).

We shall consider the simplest case, $i_S = 1$, of a solid composition defined by a single atomic concentration x (for species A, that of the other species B being $1-x$). This holds for binary alloys of elementary semiconductors, such as Ge_xSi_{1-x}, and for ternary alloys of compound semiconductors (in the latter case, the numbers of atoms on each sublattice are equal: atomic species A, B sharing a sublattice while the other is fully occupied by species C produce a pseudo-binary $A_xB_{1-x}C$ alloy). With $i_S = 1$, we have $n_L = 3$, $i_L = 2$ for self-catalyzed growth: the liquid is a genuine ternary alloy, but its state is defined by two atomic concentrations that add up to 1 (e.g. y_{Al} and y_{As} for $Al_xGa_{1-x}As$ NWs, with $y_{Ga} = 1 \quad y_{Al} \quad y_{As}$). With a foreign catalyst, $i_L = 3$ or more (if a mixture of foreign metals is used).

9.3. Dependence of alloy composition on vapor fluxes

It is only in the simplest cases that one can model how the alloy composition x depends on the vapor fluxes. In particular, in stationary VLS growth, the rate at which each component enters the droplet must equal its rate of consumption. However, an element may reach the liquid via various pathways (vapor, surface diffusion, reemission; see section 3); conversely, in addition to solid growth, it may be removed from the liquid by desorption or reverse diffusion along the sidewalls.

Following Dubrovskii [105], if the vapor composition is defined by

$$z = \frac{I_A}{I_A + I_B}, \tag{9.1}$$

with I_A and I_B the atomic contents of the MBE fluxes or CVD flows, the fraction of element A effectively available for growth is:

$$Z = \frac{V_A}{V_A + V_B}, \tag{9.2}$$

where V_A or V_B is given by the right sides of Eq. (3.4) for group III elements and of Eq. (3.5) for group V elements. The two cases are however quite different. Eq. (3.4) assumes a constant surface diffusion flux to the droplet, independent of the liquid composition. This may be acceptable for mixed group III alloys. In this case, the stationary growth constraint $x = Z$ solves the problem. If however surface diffusion depends on the chemical potentials in the liquid, or if the liquid also loses atoms by desorption, with a desorption flux that depends strongly on the concentration of the desorbing species in the droplet, as in the case of mixed group V alloys, then equation $x = Z$ is still valid, but Z now depends on liquid composition and the equation needs to be solved self-consistently..

The simple group III case is a rare instance where we can ignore the state of the liquid. In general, during steady state growth, the liquid composition will adjust to provide a nucleation rate (or more generally a growth rate) that balances the influx of the various elements, but we have to determine this composition.

9.4. Dependence of solid composition upon liquid composition

Except in the simplest cases treated in section 9.3, determining which solid composition a liquid of a given composition will produce is an essential step of VLS growth modeling. This will in particular give the solid composition profile in a NW as a function of evolving liquid composition, for instance during heterostructure formation. This can in turn be related in a self-consistent fashion to the changes in the growth fluxes, as will be illustrated in section 10. We now review briefly several approaches (items (a) to (d)) for the solid-liquid composition dependence. Note that all quantities of interest, in particular the chemical potentials, depend on temperature in addition to compositions. This dependence is kept implicit, the calculations being performed at a given temperature.

(a) For a ternary compound semiconductor $A_xB_{1-x}C$, a simple description of the solid-liquid dependence is derived in the regular growth model (section 3). Generalizing Eq. (3.14),

the rates of formation of the AC and BC pairs from a liquid with atomic concentrations y_i are assumed to be $K_A y_A y_C$ and $K_B y_B y_C$, respectively, with K_A, K_B the appropriate rate constants. It follows that:

$$x = \frac{\varepsilon y}{1+(\varepsilon-1)y}, \tag{9.3}$$

with $y = \frac{y_A}{y_A + y_B}$ and $\varepsilon = \frac{K_A}{K_B}$. Eq. (9.3) is analogous to the Everett isotherm for adsorption and becomes the Langmuir isotherm for $\varepsilon >> 1$.

Dubrovskii showed that, within this model and assuming that the rates of loss of the various NW components by the droplet (via desorption or diffusion) are proportional to their respective concentrations, the steady state relation between solid (x) and vapor (z) can be determined analytically [52].

The other approaches make use, in various ways, of the differences of chemical potential $\Delta\mu_k$ of each alloy constituent unit *k* between liquid and solid phases (these units are atoms for group IV alloys and pairs for ternary compounds; see Eq. (3.7) and ref. [14]). The calculation of the chemical potentials of use for VLS growth of III-V NWs, with or without foreign catalyst, has been discussed in section 6.2. We describe briefly these approaches.

(b) It may simply be assumed that the rate of incorporation of each unit is proportional to the relevant difference of chemical potential [107]. A difficulty is that the proportionality constants are *a priori* unknown. The underlying idea is that ML composition is defined not at nucleation stage (since critical nuclei are very small) but during its extension over the top facet.

(c) Another approach, on the contrary, makes use of equilibrium thermodynamics. Let us illustrate this in the case of mixed group III self-catalyzed III-V NWs, such as $A_xB_{1-x}As$. Since $i_S = 1$ and $i_L = 2$, there are in total three independent compositions for the L-S system. Equilibrium fixes $\Delta\mu_{AC} = 0$, $\Delta\mu_{BC} = 0$ for the two pairs. This gives the well-known result that the solid composition *x* is fixed by a single concentration in the liquid, for instance y_A. The

method consists in using this equilibrium relationship also during growth. This may look too simplistic, since NWs grow well out of equilibrium. The underlying idea is that, for such systems, the growth rate is set by the group V concentration y_C in the liquid whereas the relative incorporation of A and B into the solid is more likely to be governed by group-III concentrations in the liquid phase and barriers for attachment to the solid, which presumably depend only weakly on y_{As}. Note that this does not make any assumption about the composition of the solid nucleus that mediates the formation of each ML, but simply supposes that this nucleus is sufficiently small for the ML composition to be determined by post-nucleation attachment kinetics [108,109]. This effective 'decoupling' between group III and group V atoms was checked experimentally for MBE-grown $Al_{1-x}Ga_xAs$ NWs [108,109].

(d) Probably the most sophisticated models proposed so far rely on a version of the CNT (see section 3) developed to handle the nucleation of a phase of *a priori* unknown composition. The formation energy F of any 2D island (sections 3 and 6) now depends not only on its size but also on its composition (or alternatively, on the absolute numbers of both types of atoms or pairs that it contains). Accordingly, the critical island is defined by critical size (section 3) and critical composition. In 1950, this problem was solved elegantly by Reiss, albeit in quite a different context [110]. The formation energy of an island of radius r and composition x is:

$$F(r,x) = -c_1 r^2 h \Delta\mu(y_A, y_C, x) + c_2 \gamma_e r h, \tag{9.4}$$

where c_1, c_2 are constants depending on nucleus geometry and γ_e the surface (or edge) energy of the 2D island, introduced in section 3. Note that, in this out of equilibrium situation, we retain the full dependence of $\Delta\mu$ on three independent compositions. Reiss shows that the size and composition of the critical island are the coordinates of the saddle point, solutions of system $\frac{\partial F}{\partial r} = 0, \frac{\partial F}{\partial x} = 0$, with $\frac{\partial^2 F}{\partial r^2} < 0, \frac{\partial^2 F}{\partial x^2} > 0$. The conditions on the *r* derivatives are similar to the standard CNT conditions. In turn, the composition of the critical island minimizes the standard nucleation barrier calculated for any fixed island composition. Note that all derivatives should be

taken at given liquid composition. Figure 9.1 gives an example of such a saddle point in the formation energy surface for the self-catalyzed (Al,Ga,As) system. Only introduced in 2017 in the field of alloy NW growth, this nucleation-based approach is now used in systems of ever increasing complexity [84,105,106,109,111,112,113].

However, finding the critical island is not the end of the story, since its size is usually much smaller than that of the NW top facet. What is required is the composition of the full ML that forms by lateral growth of the critical island. The simplest assumption is that the whole ML adopts the critical island composition [105,106,109] (note that this assumption is opposite to that underlying approach (b)). Although difficult to justify, it was shown to lead to accurate predictions of the composition profiles in $Al_xGa_{1-x}As$ NWs, measured with ML axial resolution [109] (see section 10). Based on the discussion by Dubrovskii and coworkers of the growth rate of supercritical islands in the non-alloyed case [6,50], Johansson and Ghasemi calculated formally the rates of incorporation to the island of the two species constituting the alloy [114]. However, they concentrated on the limit of large islands. An accurate description of the average composition of the ML will require further investigations.

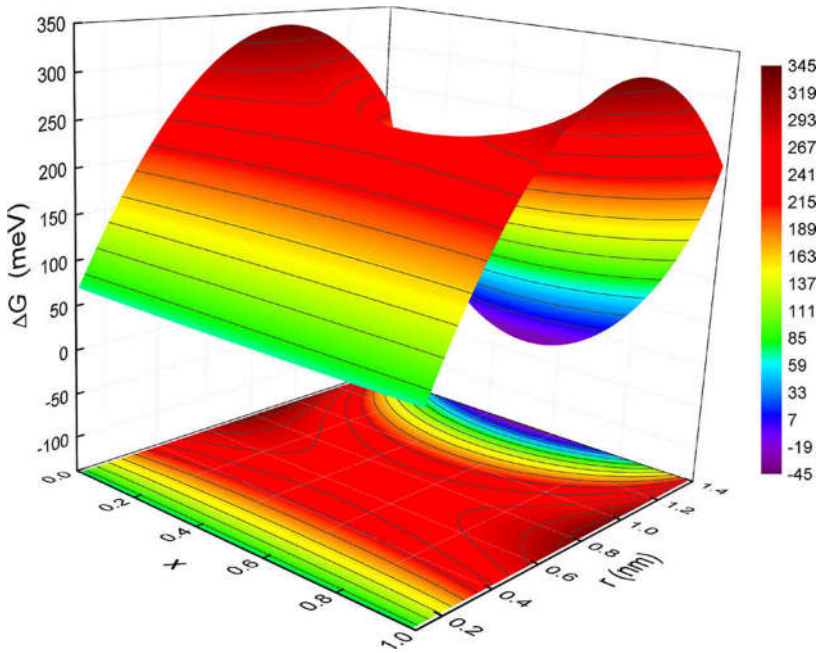

Figure 9.1. Variation of the formation energy F of an $Al_xGa_{1-x}As$ nucleus as a function of its size r

and fractional AlAs content x, calculated at temperature T = 883 K using the thermodynamic data of Li *et al.* [148]. Nucleus edge energy is γ_e = 0.123 J m^{-2} independently of x. Fixed liquid composition: y_{Al} = 0.002, y_{As} = 0.01. Reprinted with permission from F. Glas, Comparison of modeling strategies for the growth of heterostructures in III-V nanowires, Crystal Growth & Design **17**, 4785-4794 (2017). Copyright (2017) American Chemical Society.

Another issue is that of the possible dependence of edge energy γ_e (Eq. (9.4)) on island composition *x*, the so-called Renninger-Wilemski problem. This option was eliminated by Reiss in the case of liquid droplets growing from a vapor, for reason of surface segregation of the constituent with lowest surface tension [110]. It is not clear that this argument should hold for the very small solid nuclei that are typical of VLS growth. However, Glas showed that the already mentioned composition profiles in $Al_xGa_{1-x}As$ NWs where better fitted under this assumption than by supposing that γ_e increases with the Al content of the island [109].

In any case, assuming a composition-independent edge energy simplifies the problem of the liquid-solid composition dependence. From Eq. (9.4), maximizing *F* is then equivalent to minimizing $\Delta\mu(y_A, y_C, x)$ as a function of *x* for the given liquid composition (y_A, y_C). This difference reads:

$$\Delta\mu(y_A, y_C, x) = x\,\Delta\mu_{AC} + (1-x)\Delta\mu_{BC}, \tag{9.5}$$

with:

$$\Delta\mu_{AC} = \mu_A^L + \mu_C^L - \mu_{AC}^S, \qquad \Delta\mu_{BC} = \mu_B^L + \mu_C^L - \mu_{BC}^S. \tag{9.6}$$

In these expressions, at a given temperature, the chemical potentials μ_i^L in the liquid (Eq (6.14)) depend only on liquid composition whereas the chemical potentials μ_{AC}^S, μ_{BC}^S of the two III-V pairs in the solid depend only on *x*. In the regular solution model (see section 6.2), which has been widely used for compound semiconductors, the mixing enthalpy of the solid alloy simply

writes $\omega_S x(1-x)$, with ω_S the interaction parameter, and the entropy of mixing is $-k_B\left[x\ln x+(1-x)\ln(1-x)\right]$. Then:

$$\mu_{AC}^{S}=\mu_{AC}^{AC}+\omega_s(1-x)^2+k_BT\ln x,\quad \mu_{BC}^{S}=\mu_{BC}^{BC}+\omega_s x^2+k_BT\ln(1-x), \tag{9.7}$$

where μ_{AC}^{AC} and μ_{BC}^{BC} are the chemical potentials of AC and BC pairs in binaries AC and BC, which depend only on temperature. From Eqs. (9.5)-(9.7), we find that condition $\partial\Delta\mu/\partial x=0$ is equivalent to $\Delta\mu_{AC}=\Delta\mu_{BC}$. Note that these two quantities depend on liquid and solid compositions and that this constraint is *a priori* weaker than the equilibrium condition $\Delta\mu_{AC}=\Delta\mu_{BC}=0$. Using Eqs. (9.6)-(9.7), the saddle point condition $\Delta\mu_{AC}=\Delta\mu_{BC}$ can be rewritten as an implicit relation between the liquid and solid compositions [105,106,107]:

$$\varphi(y_A,y_C)=k_BT\ln\left(\frac{x}{1-x}\right)-\omega_s(2x-1), \tag{9.8}$$

with:

$$\varphi(y_A,y_C)=\mu_A^L-\mu_B^L-\left(\mu_{AC}^{AC}-\mu_{BC}^{BC}\right). \tag{9.9}$$

Dubrovskii noted that, if the liquid is also assumed to be a regular solution (see section 6.2), which means (in the self-catalyzed case) that its mixing enthalpy contains only the three interaction terms $\omega_{ij}^L y_i^L y_j^L$ associated to the three pairs of unlike atoms (with ω_{ij}^L the interaction parameter for pair (i,j)), Eq. (9.9) becomes a simple implicit relation linking the compositions of liquid and solid:

$$\frac{y}{1-y}\exp\left(-2y_{tot}\frac{\omega_{AB}^L}{k_BT}y\right)=\frac{x}{1-x}\exp\left[-\frac{\omega_s}{k_BT}(2x-1)-\alpha\right], \tag{9.10}$$

where $y=\dfrac{y_A}{y_A+y_B}$, $y_{tot}=y_A+y_B$ and:

$$\alpha=\mu_A^A-\mu_B^B-\left(\mu_{AC}^{AC}-\mu_{BC}^{BC}\right)+\omega_{AB}y_{tot}+(\omega_{AC}-\omega_{BC})(1-y_{tot}). \tag{9.11}$$

with μ_i^i the chemical potential of element i in its pure liquid form [105,106].

The concentrations of the volatile group V elements (except possibly Sb) are known to be very low in any catalyst liquid. Hence, for mixed P-As systems, $y_{tot} << 1$ and Eq. (9.10) becomes an explicit relation between atomic fractions in liquid and solid:

$$y = \frac{x}{x + (1-x)\exp\left[\dfrac{\omega_s (2x-1) + \alpha'}{k_B T}\right]}, \tag{9.12}$$

with $\alpha' = \mu_A^A - \mu_B^B - \left(\mu_{AC}^{AC} - \mu_{BC}^{BC}\right) + \omega_{AB} + \omega_{AC} - \omega_{BC}$ independent on compositions.

For mixed group III systems, the full calculations show that very wide ranges of solid compositions can be achieved with very composition-asymmetric liquids: any $Al_xGa_{1-x}As$ solid (except nearly pure AlAs) can be obtained with a very low Al concentration in the liquid (Fig. 9.2, left) and any $In_xGa_{1-x}As$ or $In_xGa_{1-x}P$ solid (save nearly pure GaAs or GaP) with a very low Ga concentration in the liquid (Fig. 9.2, right). This is related to the very different affinities of the three group III atoms for a given group V atom (P or As), themselves related to the differences of cohesive energies of the three solid binaries (these affinities increase from In to Ga to Al). Moreover, for self-catalyzed systems, $y_{tot} \approx 1$. Then, Eq. (9.12) with a constant α' is again a very good approximation; specifically, $\alpha' = \mu_A^A - \mu_B^B - \left(\mu_{AC}^{AC} - \mu_{BC}^{BC}\right) + \omega_{AB}$ for $Al_xGa_{1-x}As$ and $\alpha' = \mu_A^A - \mu_B^B - \left(\mu_{AC}^{AC} - \mu_{BC}^{BC}\right) - \omega_{AB}$ for $In_xGa_{1-x}As$ or $In_xGa_{1-x}P$.

Hence, for ternary III-V alloys, in the liquid, one NW element is much more abundant than all the others (namely, the group III element for mixed group V systems, In for mixed In-Ga or In-Al systems, Ga for mixed Al-Ga systems). An important consequence is that the regular solution model (with only pair interactions, possibly in a reduced number) is usually very accurate, since higher order concentration products are extremely small. This analysis was developed rigorously in references [105,106], where more details can be found.

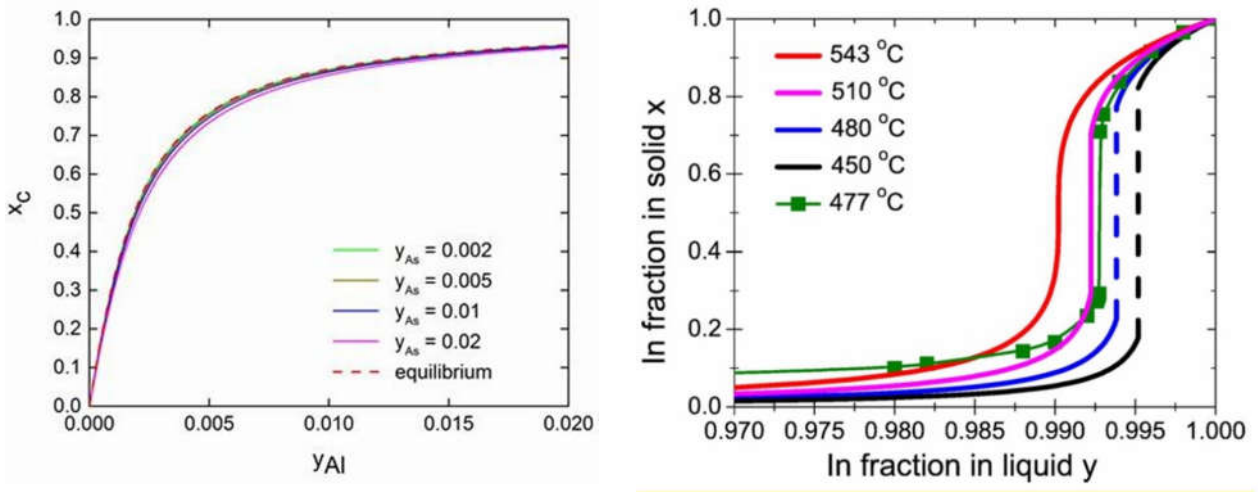

Figure 9.2. Left: (Al,Ga,As) system at T =873 K. Variation of the Al concentration in the critical $Al_xGa_{1-x}As$ nucleus as a function Al concentration in liquid, for various As concentrations y_{As} in the liquid. The dashed curve gives the variation at equilibrium. Reprinted with permission from F. Glas, Comparison of modeling strategies for the growth of heterostructures in III-V nanowires, Crystal Growth & Design **17**, 4785-4794 (2017). Copyright (2017) American Chemical Society. Right: (Ga,In,As) system. Variation of the In concentration in the critical $In_xGa_{1-x}As$ nucleus as a function In concentration in liquid at different temperatures for $c_{tot} = 0.99$. Reprinted from Material & Design, Vol. 132, V. G. Dubrovskii, A. A. Koryakin and N. V. Sibirev, Understanding the composition of ternary III-V nanowires and axial nanowire heterostructures in nucleation-limited regime, pp. 400-408, Copyright (2017), with permission from Elsevier.

This said, it is remarkable that, at least for mixed group III alloy, the simple quasi-equilibrium model (c) and the nucleation model (d) often give very similar results. This has been studied in detail for the lattice-matched $Al_xGa_{1-x}As$ system [109] (see Fig. 9.2, left) but it is also the case for the $In_xGa_{1-x}As$ or $In_xGa_{1-x}P$ systems [115]. This can be understood as follows. From Eq. (9.6), the saddle point condition $\Delta\mu_{AC} = \Delta\mu_{BC}$, which yields nucleus composition x for a given liquid composition (y_A, y_C), rewrites $\mu_A^L - \mu_B^L = \mu_{AC}^S - \mu_{BC}^S$, where the left hand side depends only on (y_A, y_C) and the right hand side only on x. If the chemical potentials μ_A^L, μ_B^L of the group III species depend little on the group V concentration y_C, then x depends effectively only on y_A, and this dependence can be computed for an arbitrary value of y_C, for

instance that corresponding to equilibrium. This explains the near-coincidence between the equilibrium and nucleation models for mixed group III alloys.

10. Heterostructures in nanowires

NWs offer great flexibility for associating different materials in a single nanostructure, which opens broad fields of basic research and applications. The 1D geometry of NWs lends itself to two elementary types of combinations: in axial heterostructures, material B is stacked on top of material A; in radial heterostructures, a shell of material B is wrapped around a core of material A. These can be elaborated into superlattice-type multiple axial or core-shell structures but also into mixed heterostructures: for instance, a quantum size section inserted axially between two barriers can be wrapped in a barrier shell, to produce a genuine quantum dot. In addition to these compositional heterostructures, crystal phase heterostructures, associating the cubic and hexagonal crystalline forms of the same material can be formed in NWs [116,117].

Standard axial heterostructures may be fabricated in the VLS mode by switching the growth fluxes. This is not possible for radial heterostructures, which are fabricated in the VS mode, with solid B nucleating on an already formed A NW directly from the vapor phase. Since this chapter deals with VLS, we will only consider axial heterostructures.

Heterostructures frequently associate materials with different lattice parameters. We first recall briefly the specific features and advantages of axial heterostructures in terms of strain relaxation, as compared with 2D structures, although these features are not specific to VLS-grown NWs. In the second part of this section, we will then discuss the VLS growth of axial heterostructures.

10.1. Elastic and plastic strain relaxation in axial heterostructures - Critical dimensions

The sidewalls of the NWs are free surfaces which permit a very efficient elastic relaxation. This has two main consequences: the strain field is more complex and less

homogeneous than in planar heterostructures and the usually deleterious plastic relaxation is hindered. Let us assume that, on top of a NW stem of radius *R* of material A, we grow a "layer" of thickness h of material B with larger stress-free (intrinsic) lattice parameter (this applies to elastically isotropic or cubic materials; for hexagonal crystals, several lattice parameters come into play). We first assume that strain relaxation remains elastic (no extended defect forms). At the very beginning of growth, since $h << R$, the system is in a quasi-2D state: the layer contracts in-plane to adapt to the stem lattice parameter and expands quadratically along the NW axis. Very soon however, strain starts distributing between layer and stem because strain relaxation of both parts is possible at the sidewalls while maintaining a coherent interface; the elastic energy stored in the system is therefore lower than in the 2D case (for the same volume of layer). This makes less likely the formation of interfacial dislocations. When *h* becomes of the order of *R*, the layer in-plane parameter approaches its strain-free value and further deposit is virtually unstrained. Following Glas [8,10], this effect may be quantified by introducing function $f(\rho) = W_e^{NW} / W_e^{2D}$ of aspect ratio $\rho = h/(2R)$, with W_e^{NW} the elastic energy stored in the whole system and W_e^{2D} the elastic energy in a cylinder of radius *R* cut in a 2D system with the same layer thickness *h* (for a semi-infinite substrate, W_e^{2D} is entirely stored in the layer) (Fig. 10.1). Then, $f(\rho) \to 1$ when $\rho \to 0$. Conversely, for $h >> R$, W_e^{NW} saturates while W_e^{2D} still scales with the volume $\pi R^2 h$ of the layer, hence $f(\rho) \sim \rho^{-1}$. By performing numerous finite elements numerical calculations, Glas showed that a very good approximation of function *f*, for elastically isotropic materials with identical elastic constants, is given by:

$$f(\rho) = \frac{1 + \tau_1 \rho \exp(-\tau_3 \rho)}{1 + \tau_2 \rho} . \qquad (10.1)$$

where parameters τ_i $(i = 1,2,3)$ depend only on the Poisson's ratio of the materials [10,118]. This is a refinement of Glas' original approximation, with numerator equal to 1 [8]. The elastic

energy is considerably reduced with respect to the 2D case, for instance to about a tenth of its 2D value for $\rho \approx 0.12$ (Fig. 10.1).

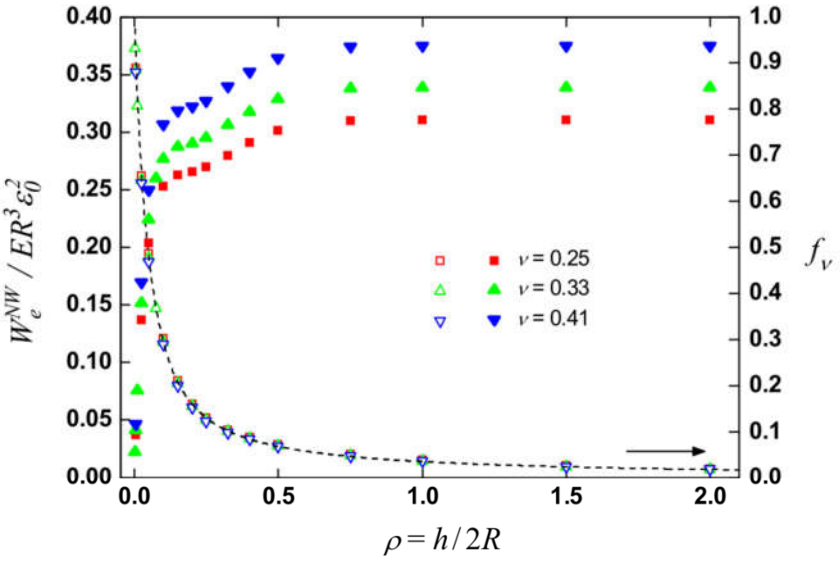

Figure 10.1. Full symbols, left scale: Variation with layer aspect ratio ρ of the total elastic energy stored in the NW (without plastic relaxation), for an isotropically elastic system with identical elastic parameters in stem and layer, and for three values of Poisson ratio ν. This energy is normalize as indicated, with E the Young's modulus, R the NW radius and ε_0 the relative misfit between stem and layer. Empty symbols, right scale: Ratio between this energy and the energy in the same volume of a 2D system. Reprinted from Semiconductors and Semimetals, vol. 93, F. Glas, Strain in nanowires and nanowire heterostructures, pp. 79-123, Copyright (2015), with permission from Elsevier.

Let us now consider the plastic relaxation of this system, which may occur via the introduction of dislocations with an edge-type component in the stem/layer interface. For given NW radius R and layer thickness h, we compare W_e^{NW} with W_p^{NW}, the energy of the system with one or several interfacial dislocations. The critical layer thickness, if any, is the thickness beyond which $W_e^{NW} > W_p^{NW}$. Indeed, W_p^{NW} includes (in addition to a reduced elastic energy) an energy associated with the dislocation core, which (neglecting possible atomic rearrangements at the intersection with the sidewalls) is proportional to the dislocation length, and hence to R, and independent of h, of the precise location of the defects in the interface and even of their number.

Hence, for small *h*, $W_p^{NW} > W_e^{NW}$. Calculations of the variation of the critical layer thickness h_c with NW radius have been performed by Glas [8,10]. h_c tends to the 2D critical thickness when $R \to \infty$ and increases with decreasing *R*. Whereas in the 2D case, W_e^{2D} scales indefinitely with *h* and always becomes larger than the energy in presence of dislocations (which increases only as $\ln(h)$), this is not necessarily the case for a NW. Actually, for any misfit ε_0, $h_c(R)$ becomes infinite for some radius R_c. This is the critical radius $R_c(\varepsilon_0)$. When $R < R_c(\varepsilon_0)$, it should be possible to grow a layer of arbitrary thickness without introducing dislocations.

Glas gave a simple analytical formulas that allows one to determine the critical radius as a function of misfit. Since R_c typically amounts to several tens of nm even for misfits of several % (for which the 2D critical thickness may be subnanometric), NWs having this radius (or less) are easily fabricated in most systems. Moreover, the very existence of a critical radius can be demonstrated on purely dimensional arguments [8]. We saw that, at large *h*, the layer (and hence the stem) are substantially strained only over a height of order *R*. Hence, the limit of W_e^{NW} at large *h* scales with R^3. We also saw that, on the other hand, W_p^{NW} contains a part scaling with *R*. From these different power-law dependences in *R*, it follows that, if the layer is thick enough, the dislocation energy always dominates, provided *R* is small enough. This proves the existence of a critical radius R_c below which plastic relaxation is unfavorable, whatever the layer thickness.

To conclude, lateral relaxation at the free sidewalls is a characteristic feature of NWs that enables very efficient stress relaxation. This allows for a much larger range of defect-free structures than in planar heterostructures or even in standard quantum dots structures.

10.2. VLS growth of axial heterostructures

Heterostructures in NWs have been fabricated for more than 20 years. A great variety of combinations has been achieved, associating elementary semiconductors [107,119,120], binary III-V compounds with alternating elements of either group III [121,122] or group V [59,123-132, 143], as well as mixed group III [133-138], group V [139,140] or group VI [141,-142] alloys. The epitaxy techniques standardly used for the VLS growth of homogeneous NWs (see section 2) have also been used for heterostructures, including MBE [119] and chemical vapor deposition (CVD) [107,120] for Si-Ge, and MOVPE [121-124,126-129,132-134,139,140], solid-source and gas-source MBE [131,136-138,141,142] and CBE [143,144,160] for compound semiconductors.

In addition to the great flexibility in terms of misfit discussed in section 10.1, axial heterostructures also offer, in principle, freedom of design and ease of control: for instance, a section of material B can be sandwiched between sections of material A, its diameter set by the NW stem diameter, its height by the growth time. In practice, controlling the section height, the sharpness of the interfaces and even the composition of the material in the case of alloys, may however be challenging.

A major difficulty is commonly associated with the "reservoir effect" (Fig. 10.2). We mentioned in section 2 that the liquid droplet acts as a reservoir of NW atoms. Whereas this is usually not a problem during the growth of a homogeneous NW, this may cause trouble for heterostructures. Indeed, during the growth of elementary semiconductor B or compound BC, B atoms reside in the droplet to ensure adequate supersaturation. Even if one switches abruptly the growth flux to A (in order to grow material A or compound AC), B will remain for some time in the droplet before it is eliminated. Elimination occurs via desorption or sidewall surface diffusion but also by incorporation in the growing NW. The joint presence of A and B in the liquid, in a proportion varying over time, thus leads to forming an A_xB_{1-x} or $A_xB_{1-x}C$ alloy, which composition evolves during growth, in other words a composition gradient. As a rule of thumb, before switching to B, the number of A atoms in the droplet scales as $\bar{y}_A R^3$, with $\bar{y}_A$ the (average) steady state concentration for A growth. In the graded solid section, this number will

distribute over a length L and hence a volume of order LR^2. Hence, $L \sim \bar{y}_{Al}/R$. This readily gives simple recipes for growing sharp interfaces: use small NW radii and elements diluted in the droplet. One way to reduce the solubility and the concentration of a NW element in the seed particle is to use solid catalysts. This is effective but it generates its own problems, in particular a low growth rate. Anyway, the VSS growth mode lies out of the scope of this review.

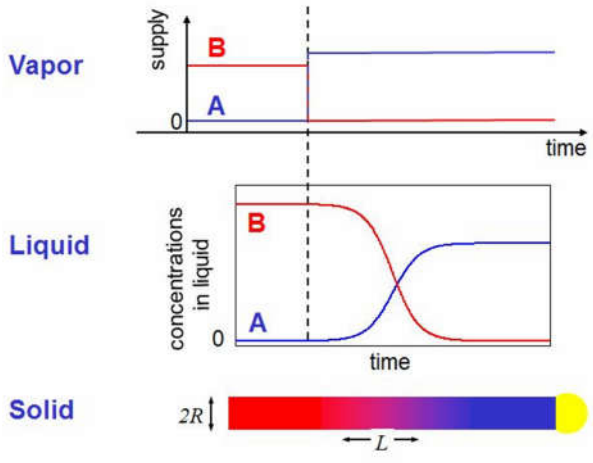

Figure 10.2. Schematics of the reservoir effect, illustrating the time variations of compositions of vapor, liquid and solid.

The simple linear dependence of the length of the transition region upon NW radius was checked for instance in the case of Au-catalyzed Ge/Si heterostructures [107,119]. In Ref. [119], the proportionality constant between R and L was found to be on the order of 1. This confirms that the concentrations of group IV elements in the catalyst are of several tens of percent, as expected from the equilibrium phase diagrams of the Au-Si and Au-Ge systems [145] (see the discussion at beginning of section 2 and generic figure 2.1).

According to the same simple estimate, it was long thought that heterostructures of III-V compounds alternating group V atoms offered the best prospect of interface sharpness, simply because the steady state concentrations of As or P in the liquid catalyst (whatever it is) are much smaller than those of group III elements or elementary semiconductors. Experimentally, sharp interfaces have indeed been obtained in alternating group V systems based on the (P,As) couple [123-125,128,131,140,160]. Since P is present at an even lower concentration in the liquid than

As (its equilibrium concentration is typically 5 times smaller), the P→As interface tends to be sharper than the As→P interface [131], as expected from our simple estimate of interface width. Interfaces tend to be broader when one of the group V elements is Sb, especially at the top of the Sb-rich segments [127,139]. This can be related to the much higher concentration of Sb in the catalyst droplet as compared with the other group V elements [146]. Since the group V species desorb from the droplet, growth interruptions further reduce the amount of species A stored in the droplet before introducing species B and hence sharpen the interfaces. This was demonstrated in the case of GaAs-GaP heterostructures [131]. Technical specificities may however degrade interface sharpness even in this favorable case, for instance the relatively long residence time of residual group V species in the MBE growth chamber after shutter closure, due to poor pumping efficiency [131].

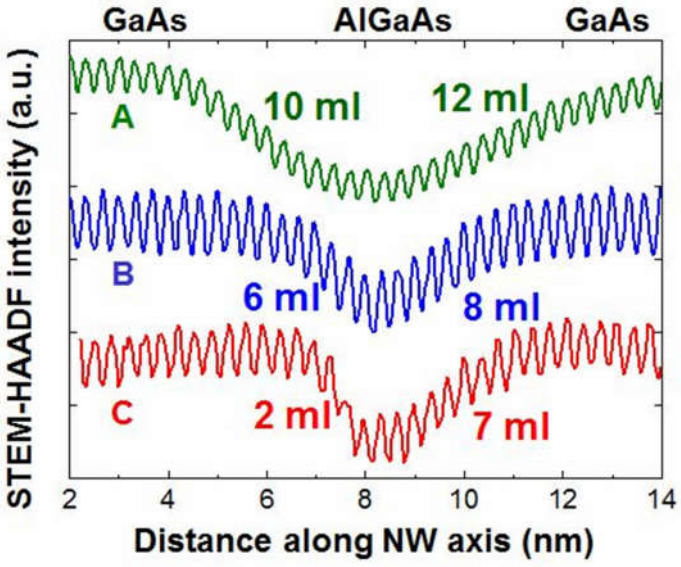

Figure 10.3. STEM-HAADF intensities measured across three $Al_xGa_{1-x}As$ axial insertions grown by MBE for 5 s in a GaAs NW. Each oscillation corresponds to a single ML and the intensity averaged over an oscillation decreases when x increases. Sample A and B were grown by simply switching the Al flux on and off while maintaining the Ga and As fluxes (the latter lower for sample B than for sample A)? Sample C was grown using the pre-filling technique described in the text. Reprinted with permission from G. Priante, F. Glas, G. Patriarche, K. Pantzas, F. Oehler, J.-C. Harmand, Sharpening the interfaces of axial heterostructures in self-catalyzed AlGaAs nanowires: experiment and theory, Nano Letters **16**, 1917-1924 (2016). Copyright (2016) American Chemical Society.

On the other hand, given the high group III concentrations in the liquid, the same simple argument seemed to preclude sharp transitions in mixed-group III systems (and especially so in the self-catalyzed scheme, when the droplet is made of at least 99% group III atoms). Recent experimental work [108] and theoretical studies of the liquid-solid composition dependence, summarized in section 9.3, have demonstrated that this is fortunately not the case: reasonably sharp interfaces may be obtained even in mixed group III heterostructures (Fig. 10.3). This can be understood as follows. As discussed in section 9.4, the liquid is overwhelmingly composed of one of the group III elements, In in the case of (In,Ga) or (In,Al) systems, Ga for the (Al,Ga) system. This means, for instance, that when growing an $Al_xGa_{1-x}As$ section atop a GaAs stem, little Al is needed in the liquid to reach high Al concentrations in the solid. The necessary y_{Al} will thus be reached rapidly and the GaAs → $Al_xGa_{1-x}As$ interface will be sharp. Moreover, since little Al is stored in the droplet during alloy growth, it will be consumed rapidly when forming the reverse $Al_xGa_{1-x}As$ → GaAs interface, which will also be sharp. This is rather satisfactory, but the interface widths measured by Priante *et al.* in samples with simple Ga-Al switches were still about 10 MLs (for rather thick NWs) 108] (Fig. 10.3, samples A and B). The interface sharpness can be improved by implementing appropriate growth strategies. In this case, Priante *et al.* performed a growth interruption after GaAs growth, during which the droplet was pre-filled with Al so that the first subsequently grown $Al_xGa_{1-x}As$ MLs were richer in Al. This produced a spectacular decrease of interface width to about 2 MLs [108] (Fig. 10.3, sample C). Other methods of manipulation of the liquid composition have been devised to improve interface abruptness [147].

10.3. Modeling the formation of axial heterostructures

Modeling the dynamics of heterostructure formation, with the aim of obtaining the axial composition profile generated by non-steady growth conditions and finding conditions insuring sharp interfaces, relies on coupling the dependence of solid composition upon liquid composition (discussed in section 9.4), which in itself is time-independent, with the rates at which the various

elements are added to the droplet (by direct fluxes, reemission, surface diffusion...) or removed from it (by growth, desorption...).

Let us consider again a ternary $A_xB_{1-x}C$ compound semiconductor alloy. Very generally, we may write, reasoning on full MLs, equations governing the variations of the numbers N_i of each species i in the liquid:

$$\frac{dN_A}{dt} = -\rho(\mathbf{y})\, x(\mathbf{y}) N^{ML} + \left(\frac{dN_A}{dt}\right)_{in} (\phi_A, \mathbf{y}), \tag{10.2a}$$

$$\frac{dN_B}{dt} = -\rho(\mathbf{y})\, [1 - x(\mathbf{y})]\, N^{ML} + \left(\frac{dN_B}{dt}\right)_{in} (\phi_B, \mathbf{y}), \tag{10.2b}$$

$$\frac{dN_C}{dt} = -\rho(\mathbf{y}) N^{ML} + \left(\frac{dN_C}{dt}\right)_{in} (\phi_C, \mathbf{y}). \tag{10.2c}$$

The first terms on the right hand side are the rates at which each species is removed from the liquid by incorporation into the solid, with ρ the rate of ML formation (which depends on liquid composition $\mathbf{y}$, this vector representing the i_L independent compositions characterizing a given liquid; see section 9.2), N^{ML} the number of atoms of each group (i.*e.* III or V) in a ML, and $x(\mathbf{y})$ the time-independent function relating solid composition to liquid compositions, discussed in section (9.4). In turn, $(dN_i/dt)_{in}$ is the net rate at which species i is added to the droplet, or removed from it, by any process except incorporation to the solid. Each rate may depend not only on the corresponding vapor flux ϕ_i but also on the composition of the liquid, which governs desorption and diffusion. All these contributions were discussed in the previous sections.

If the NW radius and the droplet contact angle are constant, the numbers N_i relate straightforwardly to concentrations y_i. A time-dependent geometry can be accounted for by adding extra equations. Note also that the rate of ML formation may depend on NW radius (this

is the case for nucleation-mediated growth; see section 3); the rates of input/output via diffusion or desorption also depend on NW radius.

Solving system (19) yields the time dependence of the composition of the liquid and hence of the solid via the $x(\mathbf{y})$ relation. One is usually more interested in the variation of the NW composition along the NW axis. For this, in principle, the absolute growth rate ρ and input rates $(dN_i/dt)_{in}$ are not needed, but their ratios must be known. Discrete versions giving the various compositions at each ML step are sometimes used [107]. As will be seen below, additional hypotheses may reduce the number of equations.

We now briefly illustrate various ways of modeling the composition profile in heterostructures, either numerically or analytically, and using any of the four types (a)-(d) of liquid-solid composition relationship reviewed in section 9.4.

System (9) (or its equivalent in simpler or more complex cases) can be solved in a purely numerical fashion. This was done by Periwal *et al.* for Ge_xSi_{1-x} heterostructures using a type (b) composition relationship [107]. The authors show that the Si/Ge_xSi_{1-x} and Ge_xSi_{1-x}/Si are always asymmetric, irrespective of the Ge concentration or NW diameter. Another numerical solution was developed by Priante *et al.* for heterostructures based on self-catalyzed $Al_xGa_{1-x}As$ alloys [108]. Within the type (c) equilibrium scheme, a single concentration, *e.g* y_{Al}, defines the state of the liquid at a given temperature. From Eq. (10.2a), it obeys equation:

$$\frac{d\,y_{Al}}{dt} = -g\,\rho\,x(y_{Al}) + \frac{I_{Al}}{N^L}, \qquad (10.3)$$

with I_{Al} the Al current (atoms per unit time) entering the droplet, g a geometrical factor and N^L the total number of atoms in the liquid. In separate experiments, the growth rate ρ was checked to be independent of solid composition for long sections of $Al_xGa_{1-x}As$ NWs, and this was assumed to hold during heterostructure formation. For an $Al_xGa_{1-x}As$ barrier inserted in a GaAs NW, post-growth ML-resolved STEM-HAADF composition measurements (see section 6.1 and circles in Fig. 10.4, left) yielded precise values of growth rate and of total number of Al

atoms delivered to the system, from which I_{Al} is easily obtained, knowing the delivery time. The observed NW geometry gave access to parameters g and N^L. Eq. (10.3) could then be solved using the $x(y_{Al})$ relation obtained from available thermodynamic data [148]. The authors showed that the computed profiles reproduce the experiments very well [108] (Fig. 10.4, left). The same experiments were later modeled within the nucleation scheme (d). Eq. (10.3) was used again but now the solid composition depends on both y_{Al} and y_{As} (see section 9.4). Modeling was thus carried out assuming different constant low values of y_{As} and it was shown that the profiles depend little on this concentration [109] (Fig. 10.4, left panel). As mentioned in section 9.4, this somehow validates the equilibrium scheme (c), at least in this system.

Turning now to analytical solutions, the simplest of these is derived within the regular growth scheme (a). Dubrovskii showed that, for simple A-B vapor flux commutation (without growth interruption), the concentrations of A and B in the solid vary exponentially at the interface (and independently of each other when a foreign catalyst is used). This solution can easily incorporate growth interruptions, which are confirmed to sharpen the interfaces in mixed group V systems (as discussed in section 10.2).

Within the nucleation scheme (d), numerical solutions of system (10.2), as discussed above, may easily handle the accurate thermodynamic descriptions of the liquid available in the literature for some systems, in particular, the self-catalyzed ones [84,109,111-112,148-150]. However, as mentioned in section 9.4 and discussed in depth by Dubrovskii *et al.* [106], for many III-V alloys at least, using such multi-parameter descriptions may be unnecessary given the specificities of these systems. Instead, analytical liquid-solid relationships based on the regular solution model, such as discussed in section 9.4, may lead to analytical descriptions of the axial composition profile in the NW.

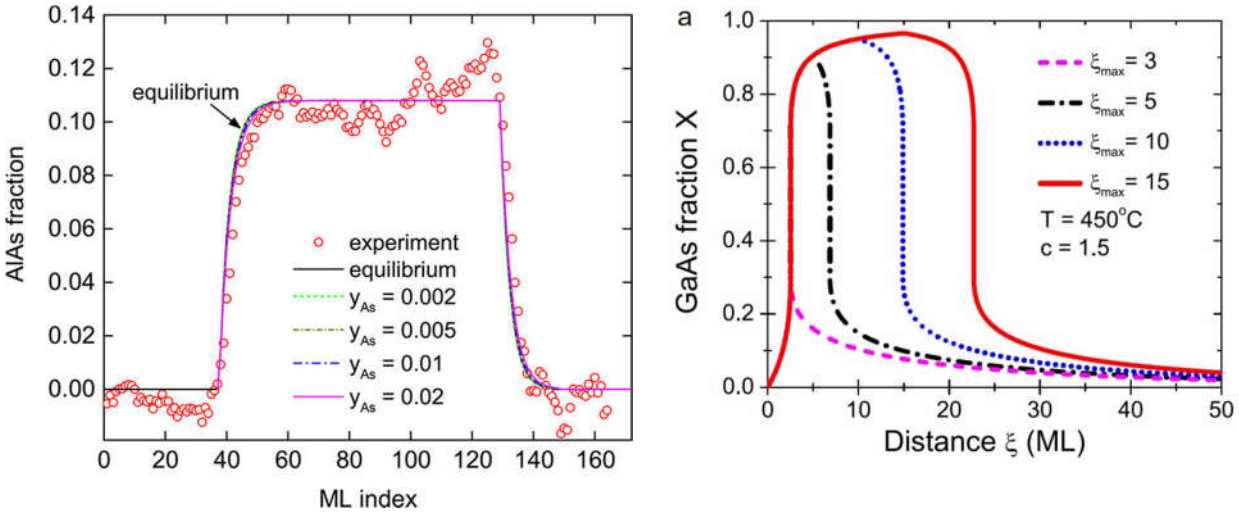

Figure 10.4. Left: Composition profiles through a GaAs-Al_xGa_{1-x}As-GaAs heterostructure calculated numerically using the nucleation model with different values of y_{As}, compared with equilibrium calculation and experimental data (circles, ref. [108]), at temperature T = 873 K. Reprinted with permission from F. Glas, Comparison of modeling strategies for the growth of heterostructures in III-V nanowires, Crystal Growth & Design **17**, 4785-4794 (2017). Copyright (2017) American Chemical Society.Right: Composition profiles through a GaAs-Ga_xIn_{1-x}As-GaAs heterostructure calculated analytically using the nucleation model. To form the heterostructure, the GaAs supply was replaced by an InAs supply during a time corresponding to the growth of ξ_{max} MLs. The different curves correspond to different values of this parameter. Reprinted from Material & Design, Vol. 132, V. G. Dubrovskii, A. A. Koryakin and N. V. Sibirev, Understanding the composition of ternary III-V nanowires and axial nanowire heterostructures in nucleation-limited regime, pp. 400-408, Copyright (2017), with permission from Elsevier. In both cases, the nucleus edge energy is assumed to be composition-independent.

This is shown by the analytical solutions obtained for interfaces in the $Al_xGa_{1-x}As$ system [106]. For this alloy without size effect (AlAs and GaAs are nearly lattice-matched), it is often assumed that the solid interaction parameter ω_S is effectively null (see *e.g.* [152]). In absence of growth interruption, with a simple switch of the Al and Ga fluxes, an equation linking explicitly axial coordinate and Al content can be derived [106]. This confirms that the interface width is dominated by the reservoir effect and proportional to a quantity scaling with R, which agrees with both experiments and numerical modeling based either on equilibrium (c) or nucleation (d) [108,109]. Further analytical results confirm the benefit of performing growth interruptions when switching the growth fluxes.

Systems based on mismatched binaries, with non-zero interaction parameter ω_S, present a miscibility gap below critical temperature $T_c = \omega_S / (2k_B)$ [F51]. At any temperature $T < T_c$ exists a range of instable solid composition, say $[x_1, x_2]$; any solid within this range will tend to decompose in solids of compositions x_1 and x_2. Consider such a ternary $A_xB_{1-x}C$ system grown self-catalytically below T_c (Fig. 10.4, right). Starting from $y_A = 0$, the liquid will be in equilibrium with solids with continuously increasing AC content x up to a certain critical value y_A^c. This particular liquid is in equilibrium with both solids of compositions x_1 and x_2. Liquids with A concentration further increasing from y_A^c will again be in equilibrium with solids with AC contents increasing smoothly from x_2. It can then be expected that the interface profile will be driven by the reservoir effect for $y \le y_A^c$ and $y \ge y_A^c$; however, the abrupt shift from x_1 to x_2 driven by an infinitesimal change of liquid composition around y_A^c should produce a locally very sharp interface. Dubrovskii showed that this is also the case not only in the equilibrium scheme (c) but also in the nucleation scheme (d) [105,106]. In this case, for each liquid composition within a certain range, there are actually two saddle points, hence two critical solid compositions, corresponding to different nucleation barriers, the lower of which is expected to give the composition of the critical nucleus giving rise to the ML. Since no nucleus ever adopts a composition within the miscibility gap, the formation of a locally very sharp interface is also predicted in this case. Atomically sharp interfaces in such lattice-mismatched were indeed observed [F153]. The right panel of Fig. 10.4 demonstrates this effect. If however the growth time of the insertion is too short, the remaining reservoir effect may prevent the solid composition to reach the edge of the miscibility gap and no sharp interface is obtained (see profiles for low values of $\xi_{\max}$ in right panel of Fig. 10.4).

11. Polytypism

11.1. Introduction

One of the most puzzling features of semiconductor NWs is that they frequently exhibit polytypism. Namely, several crystalline forms with the same composition coexist either in different NWs of the same ensemble or, most often, in a single NW. This is all the more surprising since, for many materials, in particular the III-V compounds, polytypism is specific of NWs: it appears neither in their bulk counterpart (or only in extreme pressure or temperature conditions) nor in other types of nanostructures. As far as growth is concerned, polytypism raises two main questions: Why does it appear? Is it possible to control it?

We will discuss polytypism in NWs of III-V compounds based on P, As or Sb, for which it is best documented. In bulk or quantum dot form, these III-V materials invariably adopt the cubic ZB structure. We exclude N-based compounds, which lowest energy structure is hexagonal WZ and which growth mode is usually non-VLS, catalyst-free. Polytypism also occurs in NWs of II-VI compounds [142], but this is less specific to NWs, and in Si NWs [154]. In addition to ground-state cubic ZB, the other structure most frequently encountered is hexagonal WZ (other hexagonal polytypes may be observed in some systems, but usually as transitory forms between ZB and WZ [155]). The differences of cohesive energy between the ZB and WZ forms are given in Table 10.1 for various semiconductors.

NWs usually grow along a ZB <111> direction (section 2) or WZ <0001> direction (the latter sometimes called c axis). Along these axes, the two structures consist in different stacking of the same biatomic III-V planes (MLs). In ZB (a FCC structure), the three lateral positions of the planes, called A,B,C occur periodically, producing an ABCABC... sequence, while only two positions occur in WZ, which produces an ABABAB... stacking (the A,B,C labelling is arbitrary; only the relative positions of the plane matter). Hence, these structures are easily distinguished when observing the NWs by high resolution TEM with the electron beam along a properly chosen zone axis normal to the growth axis, or by electron or X-ray diffraction.

The coexistence of ZB and WZ was first observed in InAs and GaAs NWs by Hiruma and coworkers, more than 25 years ago [156,157]. However, explanations of the formation of WZ were first proposed much later and remain few. In the next section, we review the models that have been devised so far. We summarize the main features of these models and the key parameters involved, namely surface, interface and edge energies, supersaturation of the droplet medium, contact angle of the catalyst particle and interfacial structure of the liquid.

Table 10.1. Difference of cohesive energy ΔE_{coh} between the ZB and WZ structures for various materials, in meV per atom pair. Second row: *ab initio* calculations from references [158] (a) and [159] (b) (for GaSb, see ref. [151]). Third row: estimate based on the measured stacking fault energies collected in ref. [160] (see ref. [161]). Fourth row: estimated errors on third row values.

Material	GaP	InP	GaAs	InAs	GaSb	InSb	ZnS	ZnSe	ZnTe	Si
ΔE_{coh}	18.4 [a]	5.8 [b]	24.0 [a]	12.4 [b]	29.8	16.2 [b]	6.2 [b]	10.6 [b]	12.8 [b]	23.4 [b]
ΔE_{coh}	21.5	9	22.5	15	26.5	19	≤ 3	6.5	8	27.5
	1.5	1.5	3.5	1.5	3.5	2		0.5	1	3.5

11.2. Models

In principle, the formation of ZB in NWs of the materials considered does not require any explanation. For any model explaining the formation of WZ, care should however be taken that it does not predict its occurrence in conditions where experiments show ZB to form!

(1) *Total energy models*

The first model proposed for the formation of WZ in NWs is not growth-related [162,163]. The idea is to consider the total energy of fully formed ZB and WZ NWs. This includes the bulk energy, which favors ZB, and energies associated with the sidewall surfaces and with the vertical edges between these facets. For a section of height H of a NW of radius R, these energies scale respectively as HR^2, HR and H. For sufficiently small radii, the terms

of lowest orders in R dominate the total energy. Hence, if the sidewall surface energy density or the edge line energy density is lower for WZ than for ZB, the total energy of the NW will be lower in the WZ form than in the ZB form, provided R is small enough. Qualitatively, Akiyama et al. argue that the ZB edges have more dangling bonds, and hence a larger specific energy, than the corresponding WZ edges [162]. This is substantiated by calculating the total energies using an empirical interaction potential between neighbor atoms [162,163], with the conclusion that, indeed, for all our III-V binaries, there exists a critical radius R_c below which the total energy of the NW is lower in the WZ structure. These ideas were elaborated by others, who performed *ab initio* calculations for GaAs NWs with different radii. From the variation of the total energy, they could extract the specific energies of facets and edges [62,63]. These calculations show that, on purely energetic grounds, narrow NWs should adopt the WZ structure. However, the critical radii thus found are all very small. For GaAs, the three groups find critical radii between 2 and 8 nm [62,63,163]. For the nine III-V binaries considered, the critical radii range between 6 and 15 nm [163].

Although the Akiyama-Ito theory was adduced to explain some systematic observations of pure WZ in NWs of very small radii [164], it cannot account for the numerous observations NWs of totally or partially WZ structure, with radii of many tens of nm. This is why, in 2007, Glas proposed a nucleation-based model of the formation of WZ that does not suffer from such NW radius restrictions [42]. This will be reviewed in the next section.

(2) ***Nucleation-based model***

From the very early days of the theory of VLS growth, the mechanism of 2D nucleation of new MLs at the solid-liquid interface was deemed to operate at intermediate supersaturations [165]. Many theoretical investigations indicate that 2D nucleation actually mediates NW growth and that the mononuclear regime, whereby each ML requires a single nucleation event, is very frequent (although polynucleation and regular growth cannot be entirely excluded at very high supersaturations; see section 3). Recent *in situ* TEM observations have brought strong support to

this idea: all show NWs growing ML by ML and detailed quantitative analysis of the videos indicates that each ML starts with a nucleation event, even if the event itself is too elusive to be captured [49].

Glas noted that each new ML could form in ZB or WZ position with respect to the already formed NW: calling AB the sequence of the two last formed MLs, the new ML will be in ZB position if it adopts the C position, in WZ position if it adopts the A position (position B is forbidden). It is reasonable to assume that this position is actually fixed by the position adopted by the nucleus and then adopted by the whole ML that grows laterally from it [42].

Then, explanation of WZ formation reduces to that of 2D nucleation in WZ position. Glas argued that if the nucleus is formed anywhere at the S-L interface, the ZB and WZ positions are not much different (in terms of atomic environment) so that ZB position should be favored on energetics grounds (interaction with the underlying MLs). However, this might not be the case if the nucleus forms at the TPL: part of its perimeter is then in contact with the vapor instead of the liquid and this might favor the WZ position [42]. This is akin to the idea at the basis of the total energy models (1), but, since the nucleus is always found to be very small (section 6.4), its perimeter has a very strong impact on its formation energy F (see sections 3 and 9.4).

The expression of the nucleation barrier given in section 6.4 must be adapted to differentiate between nuclei positions (ZB or WZ) and locations with respect to the TPL. Very simply, for ZB and WZ, we find barriers:

$$\Delta G_c^{ZB} = A\,\frac{\left(\gamma^{ZB}\right)^2}{\Delta\mu}, \qquad \Delta G_c^{WZ} = A\,\frac{\left(\gamma^{WZ}\right)^2}{\Delta\mu - \Delta E_{coh}} \ . \tag{11.1}$$

Here, A is a constant depending on material and nucleus geometry (assumed to be the same for ZB and WZ nuclei) and $\Delta\mu > 0$ is the difference of chemical potential between liquid and bulk ZB solid, which has to be diminished for a nucleus in WZ position. This reduction relates to the interaction of the nucleus with the underlying MLs; taking it equal to the difference of cohesive energy between bulk WZ and ZB (counted positive, as in Table 10.1) is only an approximation.

γ^{ZB} and γ^{WZ} are the specific energies of the step bordering the nucleus (in line with the CNT, these are usually taken as energies per unit area, even though the nucleus is only 1 ML high). According to what we just mentioned, we take $\gamma^{WZ} = \gamma^{ZB} = \gamma_e$ for nuclei away from the TPL, γ_e being the energy of a step in contact with the liquid (Fig. 11.1(a)). If however the nucleus forms at the TPL, a fraction x_{TPL} of its perimeter is in contact with the vapor (section 6.3), which should have a different energy depending on the type of the nucleus (Fig. 11.1(b)). A key point of the model is that this energy is not simply the phase-dependent energy γ_{SV}^{j} of the interface between the sidewall of a NW of structure *j* (ZB or WZ) and vapor: when forming at the TPL, the nucleus indeed acquires an interface with the vapor but this interface "replaces" part of the liquid-vapor that preexisted (this part is indicated by a thick curved line in Fig. 11.1(a)), the energy of which should be subtracted from the formation energy. We are thus lead to affect to this portion of the nucleus perimeter a phase-dependent *effective energy*, a simple expression of which is [42]:

$$\gamma_{eff}^{j} = \gamma_{SV}^{j} - \gamma_{LV} \sin\beta . \tag{11.2}$$

Here, γ_{LV} is the specific energy of the liquid-vapor interface, a portion of which is deleted for TPL nucleation (hence the minus sign), and this portion depends on the contact angle β of the droplet [42]. Finally, the edge energies of ZB and WZ nuclei (to be inserted in Eq. (11.1)), with standard contributions from those parts of the perimeter in contact with the liquid and phase-dependent effective contributions (11.2) from those parts at the TPL, are:

$$\gamma^{j} = (1 - x_{TPL})\gamma_e + x_{TPL}\,\gamma_{eff}^{j} . \tag{11.3}$$

Solid-vapor interface energies are probably larger than the energies γ_e of edges in contact with the liquid [40]. If so, it is only thanks to the destruction of part of the liquid-vapor interface that TPL nucleation may be favored. Eq. (11.2) predicts that this is more likely to happen for contact angles around $\pi/2$.

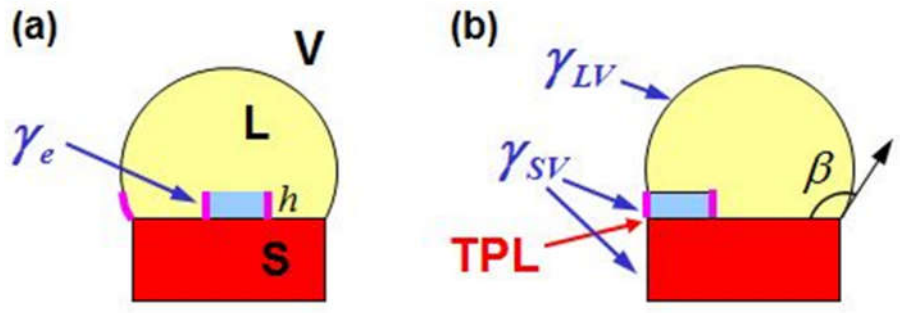

Figure 11.1. Schematics of nucleation away from the TPL (a) and at the TPL (b), with relevant interface energies indicated. The crystal phase is not specified.

From Eqs. (11.1)-(11.3), it becomes clear that, provided $\gamma_{SV}^{WZ} < \gamma_{SV}^{ZB}$ and TPL nucleation is favored, the nucleation barrier for WZ formation at the TPL may be lower than the nucleation barriers for ZB formation at the TPL or away from the TPL. Given the strong dependence of the nucleation rate on the nucleation barrier (section 3), this will largely advantage, on kinetics ground, the formation of a nucleus in WZ position, and therefore of a WZ ML. However, from Eq. (11.1), condition $\Delta G_c^{WZ} < \Delta G_c^{ZB}$ requires in addition that the chemical potential be large enough. Specifically, comparing for instance the two barriers for nucleation at the TPL, and assuming to simplify $\Delta\mu$ large with respect to ΔE_{coh} and a small relative difference $\Delta\gamma_{SV}$ of solid-vapor energies between the two phases, we find that $\Delta\mu$ must be larger than a critical value:

$$\Delta\mu^* \approx 2x\,\Delta E_{coh}\,\frac{\gamma^{ZB}}{\Delta\gamma_{SV}}. \qquad (11.4)$$

Whereas the condition $\gamma_{SV}^{WZ} < \gamma_{SV}^{ZB}$ is mainly related to the NW material (but also possibly to the growth conditions, since the solid-vapor interface energies may depend on the composition of the vapor), condition $\Delta\mu > \Delta\mu^*$ is mainly related to growth conditions set by the experimenter, which determine the supersaturation in the liquid (section 6.4).

This theory was initially developed in ref. [42], where it was argued that the conditions for WZ formation might easily be met in NW growth. It has become the basis of the vast

majority of models discussing the formation of the WZ phase in NWs. It has of course been refined in many ways (for instance, to take into account that, whereas nucleation away from the TPL can occur on most of the NW top facet, nucleation at the TPL can occur only on a small ring at the TPL [44]). We will not describe these developments, for which the reader may refer to section 6.6 of ref. [6]. Instead, we discuss how theory and experiments have confirmed virtually all the assumptions on which it is founded.

A key condition for WZ nucleation (at the TPL) is that $\gamma_{SV}^{WZ} < \gamma_{SV}^{ZB}$. *Ab initio* calculations have indeed confirmed that this is the case at least for several materials, such as GaAs and InAs, and for some of their sidewall facets commonly found in real NWs [62,63,166]. Simpler calculations based on broken bonds lead to the same conclusions, although they produce larger surface energies [167]. Even though the surface energy differences so calculated are rather small (typically only a few %), the corresponding critical values of the difference of chemical potential (Eq. (11.4)) seem to be easily attainable given the chemical potentials deduced from comparison of other experiments with models (*e.g.* regarding the kinetics of self-catalyzed GaAs growth; see ref. [40], section 6.4 and Fig. 6.10).

A very striking confirmation of a key point of the model was recently brought by *in situ* TEM experiments. Harmand *et al.* observed the VLS growth of Au-catalyzed GaAs NWs by solid source MBE in a dedicated TEM [49]. Both ZB and WZ MLs were found to grow in the mononuclear regime. Whereas ZB MLs extend very quickly after nucleation, WZ MLs advance slowly (as already reported in ref. [48]) and, by tilting the solid-liquid interface with respect to the electron beam, it is possible to follow the evolution of the geometry of their edge as the coverage of the NW top facet increases. The first fraction of ML that is observed forms very quickly after nucleation and it is systematically located at the TPL, and even at the corner between two sides of the hexagon that constitutes the TPL. In the experiments, this fraction is about 10% of a full ML, which is probably larger than the nucleus. However, probabilistic

arguments indicate that these observations make nucleation at the TPL of the WZ MLs extremely likely [49].

As already mentioned, Eq. (11.2) predicts that nucleation at the TPL, and hence WZ formation, is more likely to happen for contact angles around $\pi/2$. Conversely, *in situ* TEM reveals another correlation between structure and contact angle. Namely, for GaAs at least, at large contact angle (β over about 125°), the solid-liquid interface is truncated and ZB grows. At angles closer to $\pi/2$ (although maybe still larger than that value), the solid-liquid interface is flat and WZ grows. A model has been devised that shows that, irrespective of the solid structure and depending on surface and interface energies, the truncated shape may be favored at large β and the flat shape around $\pi/2$ [48]. It is then tempting to reason that, for contact angles around $\pi/2$, the interface is truncated so that the (111) top facet (where nucleation occurs) is not in contact with the vapor anymore. Obviously, in absence of a proper TPL (as considered in the nucleation-based model; of course, there is still a TPL, but at the edge of the truncation facet (see Fig. 4.1(c)), nucleation cannot occur at the TPL, hence WZ does not form and ZB prevails. This simple interpretation is however questionable. First, it only holds if truncation is present all around the NW, which is not clear at all at the moment. Second, although nucleation at the TPL and planar solid-liquid interface are both predicted to occur for angles around $\pi/2$ [42,48], the corresponding critical angles depend partially on different parameters and have no reason to be equal. This leaves open the question of the exact coincidence between WZ formation and vanishing of truncation observed experimentally. These questions are further discussed in section 4.

Finally, we note that the nucleation-based model describes stacking defects in otherwise perfect structures as well as polytypism. In both case, we are concerned with the position (WZ or ZB) adopted by the new ML. For instance, in the ZB structure, a stacking fault correspond to a local AB**A**BC sequence, a twin boundary to a change of stacking direction ABCAB**C**BACBA,

with only the single ML in bold wrongly stacked. Of course, forming a WZ segment requires that all successive form in WZ position.

(3) *Ordering at the solid-liquid interface*

The only other explanation of WZ formation seems to be that of Algra *et al.* [168]. These authors propose that WZ formation in Au-catalyzed InP NWs results from the peculiar arrangement adopted by the heavy Au and In atoms in the liquid in the very vicinity of the top facet of the NW. Such liquid ordering is a well-known phenomenon [169]. Typically, the density of the liquid is modulated over a few atomic layers in the direction normal to the interface but there is also some solid-like lateral ordering, especially in the first layer.

Based on surface X-ray diffraction measurements on macroscopic interfaces between solid InP and (Au,In,P) liquids supplemented by *ab initio* calculations, the authors were able to show that, in the liquid, the heavy atoms close to the solid tend to occupy specific positions. They argue that, when a new InP ML forms, this hinders the atom to occupy the ZB positions and channels them to the WZ positions.

This mechanism is not specific to NWs. It should produce WZ crystals even if growth of wide crystals is carried out from the appropriate liquids. However, such growth has not been carried out in these experiments. Somewhat surprisingly, this interesting alternative route to WZ formation during VLS growth has not been further investigated.

11.3. Crystal phase heterostructures

Polytypism enable a NW-specific type of heterostructure very different from those that associate different materials or different alloy compositions (section 10). Instead, these heterostructures combine different crystalline structures of the same material. Such ZB/WZ mixed structures have long been observed to form spontaneously and more or less randomly in III-V NWs [156] and for many years, it was rather the fabrication of single phase NWs that was a challenge. One of the interests of such heterostructures is that the interfaces may be ideally

abrupt, although mixed structures or higher order polytypes [155] may form between two pure phase sections. Another one is that, for each material, the ZB and WZ forms have different electronic structures, in particular different band gap energies. The phrase 'crystal phase heterostructure' (or 'crystal phase quantum dot') actually appeared when one started studying their optical properties (in GaAs [116] or InP [117]) or their transport properties (in InAs [170]). The control of the lengths of the sections of each phase became a new challenge and spectacular early results were obtained in fabricating periodic ZB/WZ stacks controlled to the ML [170] (Fig. 11.2).

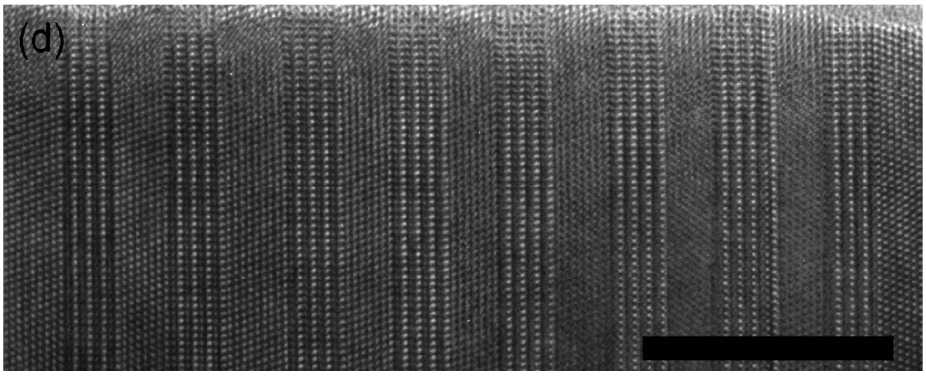

Figure 11.2. Periodic crystal phase heterostructure fabricated by Dick *et al.* in an InAs NW (growth axis is horizontal). The characteristic periods of 2 MLs for WZ (strong contrast) and 3 MLs for ZB (lower contrast). Scale bar is 20 nm. Reprinted with permission from K. A. Dick, C. Thelander, L. Samuelson, P. Caroff, Crystal phase engineering in single InAs nanowires, Nano Letters **10**, 3494-3499 (2010). Copyright (2010) American Chemical Society.

Recent *in situ* TEM experiments have demonstrated that, as discussed in section 4, the droplet contact angle is a key parameter for phase selection [48], with ZB forming at large and small contact angles and WZ in an intermediate range [61]. It is likely that the painstaking studies that allowed Dick *et al.* blindfoldly to form nearly perfect ZB/WZ superlattices [170] amounted primarily to controlling this parameter. As discussed in section 11.2, both the nucleation-based model of WZ formation [42,44] and the more recent models describing the morphology of the NW sidewalls and of the solid-liquid interface (section 4) attribute a prominent role to contact angle, with WZ predicted to form at intermediate angles. As yet, a full

understanding of the interplay between these various parameters and of the role of the chemical potential, has however not been achieved.

Acknowledgments

The long-established collaboration between the authors is currently supported by InternationalResearch Project "Physics of nanostructures and innovative devices based on compound semiconductors" (PHYNICS) established between Centre National de la Recherche Scientifique (CNRS) and the Russian Foundation for Basic Research (RFBR). The authors acknowledge fruitful discussions with their colleagues Jean-Christophe Harmand, Gilles Patriarche, Fabrice Oehler, Federico Panciera Giacomo Priante, George Cirlin and Nikolai Sibirev. VGD thanks the Russian Science Foundation for financial support under the Grant 19-72-30004. FG acknowledges financial support from Agence Nationale de la Recherche within projects ESPADON ANR-15-CE24-0029 and NanoMAX 10-EQPX-0050, and from the European Commission within Marie Skodowska-Curie Innovative Training Network INDEED (No 722176).

References

1. Wagner, R. S., Ellis, W. C.: Vapor-liquid-solid mechanism of single crystal growth. Appl. Phys. Lett. **4**, 89-90 (1964).

2. Givargizov, E. I.: Highly Anisotropic Crystals, Springer, 1987.

3. Zhang, A., Zheng, G., Lieber, C. M.: Nanowires: building blocks for nanoscience and nanotechnology. Springer, 2016.

4. Yang, P., Yan, P. R., Fardy, M.: Semiconductor nanowires: What's next? Nano Lett. **10**, 1529-1536 (2010).

5. Seifert, W., Borgström, M., Deppert, K., Dick, K. A., Johansson, J., Larsson, M. W., Mårtensson, T., Sköld, N., Svensson, C. P. T., Wacaser, B. A., Wallenberg, L. R., Samuelson,

L.: Growth of one-dimensional nanostructures in MOVPE. J. Cryst. Growth **272**, 211-220 (2004).

6. Dubrovskii, V. G.: Nucleation theory and growth of nanostructures. Springer, 2014.

7. Dubrovskii, V. G.: Theory of VLS growth of compound semiconductors. In: A. Fontcuberta i Morral, S. A. Dayeh, and C. Jagadish, editors, Semiconductors and Semimetals, v. 93, Burlington: Academic Press, 2015, pp. 1-78.

8. Glas, F.: Critical dimensions for the plastic relaxation of strained axial heterostructures in free-standing nanowires. Phys. Rev. B **74**, 121302R (2006).

9. Zhang, X., Dubrovskii, V. G., Sibirev, N. V., Ren, X.: Analytical study of elastic relaxation and plastic deformation in nanostructures on lattice mismatched substrates. Cryst. Growth Des. **11**, 5441-5448 (2011).

10. Glas, F.: Strain in nanowires and nanowire heterostructures. In: A. Fontcuberta i Morral, S. A. Dayeh, and C. Jagadish, editors, Semiconductors and Semimetals, v. 93, Burlington: Academic Press, 2015, pp. 79-123.

11. Dubrovskii, V. G.; Cirlin, G. E., Soshnikov, I. P., Tonkikh, A. A., Sibirev, N. V., Samsonenko, Yu. B., Ustinov, V. M.: Diffusion-induced growth of GaAs nanowhiskers: theory and experiment. Phys. Rev. B **71**, 205325 (2005).

12. Harmand, J. C., Patriarche, G., Péré-Laperne, N., Mérat-Combes, M.-N., Travers, L., Glas, F.: Analysis of vapor-liquid-solid mechanism in Au-assisted GaAs nanowire growth. Appl. Phys. Lett. **87**, 203101 (2005).

13. Smith, W. F.; Hashemi, J.: Foundations of materials science and engineering (4th ed.). McGraw-Hill, 2006, pp. 318-320.

14. Glas, F.: Chemical potentials for Au-assisted vapor-liquid-solid growth of III-V nanowires. J. Appl. Phys. **108**, 073506 (2010).

15. Joyce, H. J., Gao, Q., Tan, H. H., Jagadish, C., Kim, Y., Fickenscher, M. A., Perera, S., Hoang, T. B., Smith, L. M., Jackson, H. E., Yarrison-Rice, J. M., Zhang, X., Zou, J.: Unexpected benefits of rapid growth rate for III–V nanowires. Nano Lett. **9**, 695-701 (2009).

16. Chuang, L. C., Moewe, M., Chase, C., Kobayashi, N. P., Chang-Hasnain, C.: Critical diameter for III-V nanowires grown on lattice-mismatched substrates. Appl. Phys. Lett. **90**, 043115 (2007).

17. Halder, N. N., Kelrich, A., Kauffmann, Y., Cohen, S., Ritter, D.: Growth of wurtzite InP/GaP core-shell nanowires by metal-organic molecular beam epitaxy. J. Cryst. Growth **463**, 10-13 (2017).

18. Husanu, E., Ercolani, D., Gemmi, M., Sorba, L.: Growth of defect-free GaP nanowires. Nanotechnology **25**, 205601 (2014).

19. Plante, M. C., LaPierre, R. R.: Growth mechanisms of GaAs nanowires by gas source molecular beam epitaxy. J. Cryst. Growth **286**, 394-399 (2006).

20. Gil, E., Dubrovskii, V. G., Avit, G., André, Y., Leroux, C., Lekhal, K., Grecenkov, J., Trassoudaine, A., Castelluci, D., Monier, G., Ramdani, M. R., Robert-Goumet, C., Bideux, L., Harmand, J. C., Glas, F.: Record pure zincblende phase in GaAs nanowires down to 5 nm in radius. Nano Lett. **14**, 3938 (2014).

21. Mårtensson, T., Carlberg, P., Borgström, M., Montelius, L., Seifert, W., Samuelson, L.: Nanowire arrays defined by nanoimprint lithography. Nano Lett. **4**, 699-702 (2004).

22. Colombo, C., Spirkoska, D., Frimmer, M., Abstreiter, G., Fontcuberta i Morral, A.: Ga-assisted catalyst-free growth mechanism of GaAs nanowires by molecular beam epitaxy. Phys. Rev. B **77**, 155326 (2008).

23. Jabeen, F., Grillo, V., Rubini, S., Martelli, F.: Self-catalyzed growth of GaAs nanowires on cleaved Si by molecular beam epitaxy. Nanotechnology 19, 275711 (2008).

24. Gibson, S. J., Boulanger, J. P.; LaPierre R. R.: Opportunities and pitfalls in patterned self-catalyzed GaAs nanowire growth on silicon. Semicond. Sci. Technol. **28**, 105025 (2013).

25. Priante, G., Ambrosini, S., Dubrovskii, V. G., Franciosi, A., Rubini, S.: Stopping and resuming at will the growth of GaAs nanowires. Cryst. Growth Des. **13**, 3976-3984 (2013).

26. Ramdani, M. R., Harmand, J. C., Glas, F., Patriarche, G., Travers, L.: Arsenic pathways in self-catalyzed growth of GaAs nanowires. Cryst. Growth Des. **13**, 91-96 (2013).

27. Dubrovskii, V. G., Cirlin, G. E., Sibirev, N. V., Jabeen, F., Harmand, J. C., Werner, P.: New mode of vapor-liquid-solid nanowire growth. Nano Lett. **11**, 1247-1253 (2011).

28. Dubrovskii, V. G., Xu, T., Díaz Álvarez, A., Larrieu, G., A., Plissard, S. R., Caroff, P., Glas, F., Grandidier, B.: Self-equilibration of the diameter of Ga-catalyzed GaAs nanowires. Nano Lett. **15**, 5580-5584 (2015).

29. Bastiman, F., Küpers, H., Somaschini, C., Geelhaar, L.: Growth map for Ga-assisted growth of GaAs nanowires on Si(111) substrates by molecular beam epitaxy. Nanotechnology **27**, 095601 (2016).

30. Koivusalo, E. S., Hakkarainen, T. V., Guina, M., Dubrovskii, V. G.: Sub-Poissonian narrowing of length distributions realized in Ga-catalyzed GaAs nanowires. Nano Lett. **17**, 5350-5355 (2017).

31. Tauchnitz, T., Berdnikov, Y., Dubrovskii, V. G., Schneider, H., Helm, M., Dimakis E.: A simple route to synchronized nucleation of self-catalyzed GaAs nanowires on silicon for sub-Poissonian length distributions. Nanotechnology **29**, 504004 (2018).

32. Dong, Z., André, Y., Dubrovskii, V. G., Bougerol, C., Leroux, C., Ramdani, M. R., Monier, G., Trassoudaine, A., Castelluci, D., Gil. E.: Self-catalyzed GaAs nanowires on silicon by hydride vapor phase epitaxy. Nanotechnology 27, 455601 (2017).

33. Vukajlovic-Plestina, J., Kim, W., Dubrovskii, V. G., Tütüncüoğlu, G., Lagier, M., Potts, H., Friedl, M., Fontcuberta i Morral, A.: Engineering the size distributions of ordered GaAs nanowires on silicon. Nano Lett. **17**, 4101-4108 (2017).

34. Tersoff, J.: Stable self-catalyzed growth of III–V nanowires. Nano Lett. **15**, 6609-6613 (2015).

35. Kim, W., Dubrovskii, V. G., Vukajlovic-Plestina, J., Tütüncüoglu, G., Francaviglia, L., Güniat, L., Potts, H., Friedl, M., Leran, J.-B., Fontcuberta i Morral, A.: Bistability of contact angle and its role in achieving quantum-thin self-assisted GaAs nanowires. Nano Lett. **18**, 49-57 (2018).

36. Koivusalo, E. S., Hakkarainen, T. V.; Galeti, H. V. A., Gobato, Y. G., Dubrovskii, V. G., Guina, M. D.: Deterministic switching of the growth direction of self-catalyzed GaAs nanowires. Nano Lett. **19**, 82-89 (2019).

37. Dubrovskii, V. G.: Influence of the group V element on the chemical potential and crystal structure of Au-catalyzed III-V nanowires. Appl. Phys. Lett. **104**, 053110 (2014).

38. Glas, F.: Vapor fluxes on the apical droplet during nanowire growth by molecular beam epitaxy. Phys. Status Solidi B **247**, 254-258 (2010).

39. Schubert, L., Werner, P., Zakharov, N. D., Gerth, G., Kolb, F.M., Long, L., Gösele, U., Tan, T. Y.: Silicon nanowhiskers grown on <111> Si substrates by molecular beam epitaxy. Appl. Phys. Lett. **84**, 4968-4970 (2004).

40. Glas, F., Ramdani, M. R., Patriarche, G., Harmand, J. C.: Predictive modeling of self-catalyzed III-V nanowire growth. Phys. Rev. B **88**, 195304 (2013).

41. Dubrovskii, V. G.: Group V sensitive vapor-liquid-solid growth of Au-catalyzed and self-catalyzed III-V nanowires. J. Cryst. Growth **440**, 62-68 (2016).

42. Glas, F., Harmand, J. C., Patriarche, G.: Why does wurtzite form in nanowires of III-V zinc-blende semiconductors? Phys. Rev. Lett. **99**, 146101 (2007).

43. Dubrovskii, V. G., Sibirev, N. V.: Growth rate of a crystal facet of arbitrary size and the growth kinetics of vertical nanowires. Phys. Rev. E **70**, 031604 (2004).

44. Dubrovskii, V. G., Sibirev, N. V., Harmand, J. C., Glas, F.: Growth kinetics and crystal structure of semiconductor nanowires. Phys. Rev. B **78**, 235301 (2008).

45. Kashchiev, D.: Dependence of the growth rate of nanowires on the nanowire diameter. Cryst. Growth Des. **6**, 1154-1156 (2006).

46. Mårtensson, E. K., Lehmann, S., Dick, K. A., Johansson J.: Simulation of GaAs nanowire growth and crystal structure. Nano Lett. **19**, 1197-1203 (2019)

47. Wen, C.-Y., Tersoff, J., Hillerich, K., Reuter, M. C., Park, J. H., Kodambaka, S., Stach, E. A., Ross, F. M.: Periodically changing morphology of the growth interface in Si, Ge, and GaP nanowires. Phys. Rev. Lett. **107**, 025503 (2011).

48. Jacobsson, D., Panciera, F., Tersoff, J., Reuter, M. C., Lehmann, S., Hofmann, S., Dick, K. A., Ross, F. M.: Interface dynamics and crystal phase switching in GaAs nanowires. Nature **531**, 317-322 (2016).

49. Harmand, J. C., Patriarche, G., Glas, F., Panciera, F., Florea, I., Maurice, J.-L., Travers, L., Ollivier, Y.: Atomic step flow on a nanofacet. Phys. Rev. Lett. **121**, 166101 (2018).

50. Dubrovskii, V. G., Grecenkov, J.: Zeldovich nucleation rate, self-consistency renormalization, and crystal phase of Au-catalyzed GaAs nanowires. Cryst. Growth Des. **15**, 340-347 (2015).

51. Ameruddin, A. S., Caroff, P., Tan, H. H., Jagadish, C., Dubrovskii, V. G.: Understanding the growth and composition evolution of gold-seeded ternary InGaAs nanowires. Nanoscale **7**, 16266 (2015).

52. Dubrovskii, V. G.: Fully analytical description for the composition of ternary vapor-liquid-solid nanowires. Cryst. Growth Des. **15**, 5738-5743 (2015).

53. Dubrovskii, V. G., Sibirev, N. V.: Factors influencing the interfacial abruptness in axial III-V nanowire heterostructures. Cryst. Growth Des. **16**, 2019-2023 (2016).

54. Dubrovskii, V. G.: Compositional control of gold-catalyzed ternary nanowires and axial nanowire heterostructures based on $IIIP_{1-x}As_x$. J. Cryst. Growth **498**, 179-185 (2018).

55. Dubrovskii, V. G., Sokolova, Zh. V., Rylkova, M. V., Zhiglinsky, A. A.: Composition and contact angle of Au-III-V droplets on top of Au-catalyzed III-V nanowires. Materials Physics and Mechanics **36**, 1-7 (2018).

56. Nebol'sin, V. A., Shchetinin, A. A.: Role of surface energy in the vapor–liquid–solid growth of silicon. Inorg. Mater. **39**, 899-903 (2003).

57. Ross, F. M., Tersoff, J., Reuter, M. C.: Sawtooth faceting in silicon nanowires. Phys. Rev. Lett. **95**, 146104 (2005).

58. Dubrovskii, V. G.: Development of growth theory for vapor-liquid-solid nanowires: contact angle, truncated facets and crystal phase. Cryst. Growth Des. **17**, 2544-2548 (2017).

59. Zannier, V., Rossi, F., Dubrovskii, V. G., Ercolani, D., Battiato, S., Sorba, L.: Nanoparticle stability in axial InAs InP nanowire heterostructures with atomically sharp interfaces. Nano Lett. **18**, 167-174 (2018).

60. Johansson, J., Karlsson, L. S., Dick, K. A., Bolinsson, J., Wacaser, B. A., Deppert, K., Samuelson, L.: Effects of supersaturation on the crystal structure of gold seeded III–V nanowires. Cryst. Growth Des. **9**, 766-773 (2009).

61. Panciera, F., Baraissov Z., Patriarche, G., Dubrovskii, V. G., Glas, F., Travers, L., Mirsaidov U., Harmand, J.-C.: Phase selection in self-catalyzed GaAs nanowires. Nano Lett. 20, 1669-1675 (2020).

62. Pankoke, V., Kratzer, P., Sakong, S.: Calculation of the diameter-dependent polytypism in GaAs nanowires from an atomic motif expansion of the formation energy. Phys. Rev. B **84**, 075455 (2011).

63. Rosini, M., Magri, R.: Surface effects on the atomic and electronic structure of unpassivated GaAs nanowires. ACS Nano **4**, 6021-6031 (2010).

64. Moll, N., Kley, A., Pehlke, E., Scheffler, M.: GaAs equilibrium crystal shape from first principles. Phys. Rev. B **54**, 8844-8855 (1996).

65. Dubrovskii, V. G., Sibirev, N. V., Cirlin, G. E., Soshnikov, I. P., Chen, W. H., Larde, R., Cadel, E., Pareige, P., Xu, T., Grandidier, B., Nys, J.-P., Stievenard, D., Moewe, M., Chuang, L. C., Chang-Hasnain, C.: Gibbs-Thomson and diffusion-induced contributions to the growth rate of Si, InP and GaAs nanowires. Phys. Rev. B **79**, 205316 (2009).

66. Mohan, P., Motohisa, J., Fukui, T.: Controlled growth of highly uniform, axial/radial direction-defined, individually addressable InP nanowire arrays. Nanotechnology 2005, 16, 2903.

67. Tomioka, K., Mohan, P., Noborisaka, J., Hara, S., Motohisa, J., Fukui, T.: Growth of highly uniform InAs nanowire arrays by selective-area MOVPE. J. Cryst. Growth **298**, 644-647 (2007).

68. Dalacu, D., Kam, A., Austing, D. G., Wu, X., Lapointe, J., Aers, G. C., Poole, P. J.: Selective-area vapour–liquid–solid growth of InP nanowires. Nanotechnology **20**, 395602 (2009).

69. Hertenberger, S., Rudolph, D., Bichler, M., Finley, J. J., Abstreiter, G., Koblmüller, G.: Growth kinetics in position-controlled and catalyst-free InAs nanowire arrays on Si(111) grown by selective area molecular beam epitaxy. J. Appl. Phys. **2010**, 108, 114316 (2010).

70. Bassett, K. P., Mohseni, P. K., Li, X.: Evolution of GaAs nanowire geometry in selective area epitaxy. Appl. Phys. Lett. 106, 133102 (2015).

71. Robson, M., Azizur-Rahman, K. M., Parent, D., Wojdylo, P., Thompson, D. A., LaPierre, R. R.: Multispectral absorptance from large-diameter InAsSb nanowire arrays in a single epitaxial growth on silicon. Nano Futures **1**, 035001 (2017).

72. Robson, M. T., Dubrovskii, V. G., LaPierre, R. R.: Conditions for high yield of selective-area epitaxy InAs nanowires on SiOx/Si(111) substrates. Nanotechnology **26**, 465301 (2015).

73. Gao, Q., Dubrovskii, V. G., Caroff, P., Wong-Leung, J., Li, L., Guo, Y., Fu, L., Tan, H. H., Jagadish, C.: Simultaneous selective-area and vapor-liquid-solid growth of InP nanowire arrays. Nano Lett. **16**, 4361-4367 (2016).

74. Dubrovskii, V. G.: Evolution of the length and radius of III-V nanowires grown by selective area epitaxy. ACS Omega **4**, 8400-8405 (2019).

75. Sibirev, N. V., Tchernycheva, M., Timofeeva, M. A., Harmand, J. C., Cirlin, G. E., Dubrovskii, V. G.: Influence of shadow effect on the growth and shape of InAs nanowires. J. Appl. Phys. **111**, 104317 (2012).

76. Dubrovskii, V. G., Sibirev, N. V., Cirlin, G. E., Bouravleuv, A. D., Samsonenko, Y. B., Dheeraj, D. L., Zhou, H. L., Sartel, C., Harmand, J. C., Patriarche, G., Glas, F.: Role of non-linear effects in nanowire growth and crystal phase. Phys. Rev. B **80**, 205305 (2009).

77. Harmand, J. C., Glas, F., Patriarche, G.: Growth kinetics of a single $InP_{1-x}As_x$ nanowire. Phys. Rev. B **81**, 235436 (2010).

78. Dubrovskii, V. G., Hervieu, Yu. Yu.: 2014. Diffusion-induced growth of nanowires: generalized boundary conditions and self-consistent kinetic equation. J. Cryst. Growth **401**, 431-440 (2014).

79. Johansson, J., Svensson, C. P. T., Mårtensson, T., Samuelson, L., Seifert, W.: Mass transport model for semiconductor nanowire growth. J. Phys. Chem. B **109**, 13567-13571 (2005).

80. Fröberg, L. E., Seifert, W., Johansson, J.: Diameter-dependent growth rate of InAs nanowires. Phys. Rev. B **76**, 153401 (2007).

81. Consonni, V.; Dubrovskii, V. G., Trampert, A.; Geelhaar, L., Riechert. H.: Quantitative description for the growth rate of self-induced GaN nanowires. Phys. Rev. B **85**, 155313 (2012).

82. Dayeh, S. A., Picraux, S. T.: Direct observation of nanoscale size effects in Ge semiconductor nanowire growth. Nano Lett. **10**, 4032-4039 (2010).

83. Dubrovskii, V. G., Sibirev, N. V., Suris, R. A., Cirlin, G. E., Harmand J. C., Ustinov, V. M.: Diffusion controlled growth of semiconductor nanowires: vapor pressure versus high vacuum deposition. Surf. Sci. **601**, 4395-4401 (2007).

84. Leshchenko, E. D., Ghasemi, M., Dubrovskii, V. G., Johansson, J.: Nucleation-limited composition of ternary III-V nanowires forming from quaternary gold based liquid alloys. CrystEngComm **20**, 1649-1655 (2018).

85. Stringfellow, G. B.: Calculation of ternary phase diagrams of III–V systems. J. Phys. Chem. Solids **33**, 665-677 (1972).

86. Glas, F., Dubrovskii, V. G.: Energetics and kinetics of monolayer formation in vapor-liquid-solid nanowire growth. Phys. Rev. Materials **4**, 083401 (2020).

87. Dubrovskii, V. G.: Refinement of nucleation theory for vapor-liquid-solid nanowires. Cryst. Growth Des. **17**, 2589-2593 (2017).

88. Glas, F., Harmand, J. C., Patriarche, G.: Nucleation antibunching in catalyst-assisted nanowire growth. Phys. Rev. Lett. **104**, 135501 (2010).

89. Moewe, M.; Chuang, L. C.; Dubrovskii, V. G.; Chang-Hasnain, C.: Growth mechanisms and crystallographic structure of InP nanowires on lattice-mismatched substrates. J. Appl. Phys., **104**, 044313(2008).

90. Leshchenko, E. D.; Kuyanov, P., LaPierre, R. R., Dubrovskii, V. G.: Tuning the morphology of self-assisted GaP nanowires. Nanotechnology **29**, 225603 (2018).

91. Dubrovskii, V. G.: Self-regulated pulsed nucleation in catalyzed nanowire growth. Phys. Rev. **87**, 195426 (2013).

92. Dubrovskii, V. G., Sibirev, N. V., Berdnikov, Y., Gomes, U. P., Ercolani, D., Zannier, V., Sorba, L.: Length distributions of Au-catalyzed and In-catalyzed InAs nanowires. Nanotechnology **27**, 375602 (2016)

93. Dubrovskii, V. G., Berdnikov, Y., Schmidtbauer, J., Borg, M., Storm, K., Deppert, K., Johansson, J.: Length distributions of nanowires growing by surface diffusion. Cryst. Growth Des. **16**, 2167-2172 (2016).

94. Dubrovskii, V. G.: Length distributions of nanowires: effects of surface diffusion versus nucleation delay. J. Cryst. Growth 463, 139-144 (2017).

95. Glas, F., Dubrovskii, V. G.: Self-narrowing of size distributions of nanostructures by nucleation antibunching. Phys. Rev. Materials **1**, 036003 (2017).

96. Dubrovskii, V. G.: Analytic form of the size distribution in irreversible growth of nanoparticles. Phys. Rev. E **99**, 012105 (2019).

97. Matteini, F., Dubrovskii, V. G., Rüffer, D., Tütüncüoğlu, G., Fontana, Y., Fontcuberta i Morral, A.: Tailoring the diameter and density of self-catalyzed GaAs nanowires on silicon. Nanotechnology **26**, 105603 (2015).

98. Dubrovskii, V. G., Sibirev, N. V.: Analytic scaling function for island-size distributions. Phys. Rev. E **91**, 042408 (2015).

99. Glas, F.: Statistics of sub-Poissonian nucleation in a nanophase. Phys. Rev. B **90**, 125406 (2014).

100. Dubrovskii, V. G.: Fluctuation-induced spreading of size distribution in condensation kinetics. J. Chem. Phys. **131**, 164514 (2009).

101. Hakkarainen, T. V., Schramm, A., Mäkelä, J., Laukkanen, P., Guina, M.: Lithography-free oxide patterns as templates for self-catalyzed growth of highly uniform GaAs nanowires on Si(111). Nanotechnology **26**, 275301 (2015).

102. Choi, S. G., Manandhar, P., Picraux, S. T.: Vapor-liquid-solid epitaxial growth of $Si_{1-x}Ge_x$ alloy nanowires: Composition dependence on precursor reactivity and morphology control for vertical forests. J. Appl. Phys. **118**, 014303 (2015).

103. Biswas, S., Doherty, J., Saladukha, D., Ramasse, Q., Majumdar, D., Upmanyu, M., Singha, A., Ochalski, T., Morris, M. A., Holmes, J. D.: Non-equilibrium induction of tin in germanium: towards direct bandgap $Ge_{1-x}Sn_x$ nanowires. Nature Comm. **7**, 11405 (2016).

104. Pan, A., Nichols, P. L., Ning, C. Z.: Semiconductor alloy nanowires and nanobelts with tunable optical properties. IEEE J. Select. Topics Quant. Electron. **17**, 808-818 (2011).

105. Dubrovskii, V. G.: Understanding the vapor-liquid-solid growth and composition of ternary III-V nanowires and nanowire heterostructures. J. Phys. D: Appl. Phys. **50**, 453001 (2017).

106. Dubrovskii, V. G., Koryakin, A. A., Sibirev, N. V.: Understanding the composition of ternary III-V nanowires and axial nanowire heterostructures in nucleation-limited regime. Mater. Des. **132**, 400-408 (2017).

107. Periwal, P., Sibirev, N. V., Patriarche, G., Salem, B., Bassani, F., Dubrovskii, V. G., Baron, T.: Composition-dependent interfacial abruptness in Au-catalyzed $Si_{1-x}Ge_x/Si/Si_{1-x}Ge_x$ nanowire heterostructures. Nano Lett. **14**, 5140-5147 (2014).

108. Priante, G., Glas, F., Patriarche, G., Pantzas, K., Oehler, F., Harmand, J.-C.: Sharpening the interfaces of axial heterostructures in self-catalyzed AlGaAs nanowires: experiment and theory. Nano Lett. **16**, 1917-1924 (2016).

109. Glas, F.: Comparison of modeling strategies for the growth of heterostructures in III-V nanowires. Cryst. Growth Des. **17**, 4785-4794 (2017).

110. Reiss, H.: The kinetics of phase transitions in binary systems. J. Chem. Phys. **18**, 840-848 (1950).

111. Johansson, J., Ghasemi, M.: Composition of gold alloy seeded InGaAs nanowires in the nucleation limited regime. Cryst. Growth Des. **17**, 1630-1635 (2017).

112. Ghasemi, M., Selleby, M., Johansson, J.: Thermodynamic assessment and binary nucleation modeling of Sn-seeded InGaAs nanowires. J. Cryst. Growth **478**, 152-158 (2017).

113. Johansson, J., Leshchenko, E. D.: Zinc blende and wurtzite crystal structure formation in gold catalyzed InGaAs nanowires. J. Cryst. Growth **509**, 118-123 (2019).

114. Johansson, J., Ghasemi, M.: Kinetically limited composition of ternary III-V nanowires. Phys. Rev. Mater.**1**, 040401 (2017).

115. Scaccabarozzi, A., Cattoni, A., Patriarche, G., Travers, L., Collin, S., Harmand, J.-C., Glas, F., Oehler, F: Stable and high yield growth of GaP and GaAs nanowires arrays using In as a catalyst. Submitted to Nanoscale (June 2020).

116. Spirkoska, D., Arbiol, J., Gustafsson, A., Conesa-Boj, S., Glas, F., Zardo, I., Heigoldt, M., Gass, M. H., Bleloch, A. L., Estrade, S., Kaniber, M., Rossler, J., Peiro, F., Morante, J. R., Abstreiter, G., Samuelson, L., Fontcuberta i Morral, A.: Structural and optical properties of high quality zinc-blende/wurtzite GaAs nanowire heterostructures. Phys. Rev. B **80**, 245325 (2009).

117. Akopian, N., Patriarche, P., Liu, L., Harmand, J.-C., Zwiller, V.: Crystal phase quantum dots. Nano Lett. **10**, 1198-1201 (2010).

118. Glas, F., Daudin, B.: Stress-driven island growth on top of nanowires. Phys. Rev. B **86**, 174112 (2012).

119. Zakharov, N. D., Werner, P., Gerth, G., Schubert, L., Sokolov, L., Gösele, U.: Growth phenomena of Si and Si/Ge nanowires on Si (1 1 1) by molecular beam epitaxy. J. Cryst. Growth **290**, 6-10 (2006).

120. Dayeh, S. A., Wang, J., Li, N., Huang, J. Y., Gin, A. V., Picraux, S. T.: Growth, defect formation, and morphology control of germanium-silicon semiconductor nanowire heterostructures. Nano Lett. **11**, 4200-4206 (2011).

121. Hiruma, K., Murakoshi, H., Yazawa, M., Katsuyama, T.: Self-organized growth of GaAs/InAs heterostructure nanocylinders by organometallic vapor phase epitaxy. J. Cryst. Growth **163**, 226-231 (1996).

122. Paladugu, M., Zou, J., Guo, Y.-N., Zhang, X., Kim, Y., Joyce, H. J., Gao, Q., Tan, H. H., Jagadish, C.: Nature of heterointerfaces in GaAs/InAs and InAs/GaAs axial nanowire heterostructures. Appl. Phys. Lett. **93**, 101911 (2008).

123. Björk, M. T., Ohlsson, B. J., Sass, T., Persson, A. I., Thelander, C., Magnusson, M. H., Deppert, K., Wallenberg, L. R., Samuelson, L.: One-dimensional steeplechase for electrons realized. Nano Lett. **2**, 87-89 (2002).

124. Fröberg, L. E., Wacaser, B. A., Wagner, J. B., Jeppesen, S., Ohlsson, B. J., Deppert, K., Samuelson, L.: Transients in the formation of nanowire heterostructures. Nano Lett. **8**, 3815-3818 (2008).

125. Boulanger, J. P., LaPierre, R. R.: Polytype formation in GaAs/GaP axial nanowire heterostructures. J. Cryst. Growth **332**, 21-26 (2011).

126. Pozuelo, M., Zhou, H., Lin, S., Lipman, S. A., Goorsky, M. S., Hicks, R. F., Kodambaka, S.: Self-catalyzed growth of InP/InSb axial nanowire heterostructures. J. Cryst. Growth **329**, 6-11 (2011).

127. Caroff, P., Wagner, J. B., Dick, K. A., Nilsson, H. A., Jeppsson, M., Deppert, K., Samuelson, L., Wallenberg, L. R., Wernersson, L.-E.: High-quality InAs/InSb nanowire heterostructures grown by metal-organic vapor-phase epitaxy. Small **4**, 878-882 (2008).

128. Borgström, M. T., Verheijen, M. A., Immink, G., de Smet, T., Bakkers, E. P. A. M.: Interface study on heterostructured GaP-GaAs nanowires. Nanotechnology **17**, 4010-4013 (2006).

129. Jeppsson, M., Dick, K. A., Wagner, J. A., Caroff, P., Deppert, K., Samuelson, L., Wernersson, L.-E.: GaAs/GaSb nanowire heterostructures grown by MOVPE. J. Cryst. Growth **310**, 4115-4121 (2008).

130. Boulanger, J. P., LaPierre R. R.: Unveiling transient GaAs/GaP nanowire growth behavior using group V oscillations. Cryst. Growth **388**, 116-123 (2014).

131. Priante, G., Patriarche, G., Oehler, F., Glas, F., Harmand, J.-C.: Abrupt GaP/GaAs interfaces in self-catalyzed nanowires. Nano Lett. **15**, 6036-6041 (2015).

132. Tateno, K., Zhang, G., Takiguchi, M., Gotoh H., Sogawa, T.: VLS growth of alternating InAsP/InP heterostructure nanowires for multiple-quantum-dot structures. Nano Lett. **12**, 2888-2893 (2012).

133. Ouattara, L., Mikkelsen, A., Sköld, N., Eriksson, J., Knaapen, T., Cavar, E., Seifert, W., Samuelson, L., Lundgren, E.: GaAs/AlGaAs nanowire heterostructures studied by scanning tunneling microscopy. Nano Lett. **7**, 2859-2864 (2007).

134. Guo, J., Huang, H., Ren, X., Xin, Y., Cai, S., Huang, Y., Wang, Q., Zhang, X., Wang, W.: Stacking-faults-free zinc blende GaAs/AlGaAs axial heterostructure nanowires during vapor-liquid-solid growth. Chinese Opt. Lett. **9**, 041601 (2011).

135. Tateno, K., Zhang, G., Nakano, H.: Growth of GaInAs/AlInAs heterostructure nanowires for long-wavelength photon emission. Nano Lett. **8**, 3645-3650 (2008).

136. Heiß, M., Gustafsson, A., Conesa-Boj, S., Peiró, F., Morante, J. R., Abstreiter, G., Arbiol, J. G., Samuelson, L., Fontcuberta i Morral, A.: Catalyst-free nanowires with axial $In_xGa_{1-x}As$/GaAs heterostructures. Nanotechnology **20**, 075603 (2009).

137. Krogstrup, P., Yamasaki, J., Sørensen, C. B., Johnson, E., Wagner, J. B., Pennington, R., Aagesen, M., Tanaka, N., Nygård, J.: Junctions in axial III-V heterostructure nanowires obtained

via an interchange of group III elements. Nano Lett. **9**, 3689-3693 (2011).

138. Priante, G., Glas, F., Patriarche, G., Pantzas, K., Oehler, F., Harmand, J.-C.: Sharpening the interfaces of axial heterostructures in self-catalyzed AlGaAs nanowires: experiment and theory. Nano Letters **16**, 1917-1924 (2016).

139. Plissard, S., Dick, K. A., Wallart, X., Caroff, P.: Gold-free GaAs/GaAsSb heterostructure nanowires grown on silicon. Appl. Phys. Lett. **96**, 121901 (2010).

140. Tateno, K., Zhang, G., Takiguchi, M., Gotoh H.: Alternating InAsP/InP heterostructure nanowires grown with tertiarybutyl chloride. Nano Futures **2**, 045006 (2018).

141. Hsiao, C. H., Chang, S. J., Hung, S. C., Cheng, Y. C., Huang, B. R., Wang, S. B., Lan, B. W., Chih, S. H.: ZnSe/ZnCdSe heterostructure nanowires. J. Cryst. Growth **312**, 1670-1675 (2010).

142. Bellet-Amalric, E., Elouneg-Jamroz, M., Rueda-Fonseca, P., Bounouar, S., Den Hertog, M., Bougerol, C., André, R., Genuist, Y., Poizat, J. P., Kheng, K., Cibert, J., Tatarenko, S.: Growth of II–VI ZnSe/CdSe nanowires for quantum dot luminescence. J. Cryst. Growth **378**, 233-237 (2013).

143. Ercolani, D., Rossi, F., Li, A., Roddaro, S., Grillo, V., Salviati, G., Beltram, B., Sorba, L.: InAs/InSb nanowire heterostructures grown by chemical beam epitaxy. Nanotechnology **20**, 505605 (2009).

144. Zannier, V., Rossi, F., Ercolani, D., Sorba, L.: Growth dynamics of InAs/InP nanowire heterostructures by Au-assisted chemical beam epitaxy. Nanotechnology **30**, 094003 (2019).

145. Chevalier, P.-Y.: A thermodynamic evaluation of the Au-Ge and Au-Si systems. Thermochim. Acta, **141**, 217-226 (1989).

146. Burke, R. A., Weng, X., Kuo, M.-W., Song, Y.-W., Itsuno, A. M., Mayer, T. S., Durbin, S. M., Reeves, R. J., Redwing, J. M.: Growth and characterization of unintentionally doped GaSb nanowires. J. Electron. Mater. **39**, 355-364 (2010).

147. Dick, K. A., Bolinsson, J., Borg, B. M., Johansson, J.: Controlling the abruptness of axial

heterojunctions in III V nanowires: Beyond the reservoir effect. Nano Lett. **12**, 3200-3206 (2012).

148. Li, C.; Li, J. B.; Du, Z.; Lu, L.; Zhang, W.: A thermodynamic reassessment of the Al-As-Ga system. J. Phase Equilib. **22**, 26-33 (2001)

149. Li, J.-B., Zhang, W., Li, C., Du, Z.: A thermodynamic assessment of the Ga-As-Sb system. J. Phase Equil. **19**, 466-472 (1998).

150. Li, C., Li, J.-B., Du, Z., Zhang, W.: A thermodynamic assessment of the Ga-In-P system. J. Phase Equil. **21**, 357-363 (2000).

151. Ansara, I., Chatillon, C., Lukas, H. L., Nishizawa, T., Ohtani, H., Ishida, K., Hillert, M., Sundman, B., Argent, B. B., Watson, A., Chart, T., Anderson, T.: A binary database for III-V compound semiconductor systems. Calphad **18**, 177-222 (1994).

152. Glas, F.: Elastic strain relaxation: thermodynamics and kinetics. In: M. Hanbücken, P. Müller and R. B. Wehrspohn, editors, Mechanical stress on the nanoscale - Simulation, material systems and characterization techniques, Weinheim: Wiley-VCH, 2011, pp. 3-26.

153. Zannier, V., Rossi, F., Dubrovskii, V. G., Ercolani, D., Battiato, S., Sorba, L.: Nanoparticle stability in axial InAs-InP nanowire heterostructures with atomically sharp interfaces. Nano Lett. **18**, 167-174 (2018).

154. Tang, J., Maurice, J.-L., Fossard, F., Florea, I., Chen, W., Johnson, E. V., Foldyna, M., Yu, L., Roca i Cabarrocas, P.: Natural occurrence of the diamond hexagonal structure in silicon nanowires grown by plasma assisted vapour-liquid-solid method. Nanoscale **9**, 8113-8118 (2017).

155. Dheeraj, D. L., Patriarche, G., Zhou, H., Hoang, T. B., Moses, A. F., Grønsberg, S., van Helvoort, A. T. J., Fimland, B. O., Weman, H.: Growth and characterization of wurtzite GaAs nanowires with defect-free zinc blende GaAsSb inserts. Nano Lett. **8**, 4459-4463 (2008).

156. Koguchi, M., Kakiyabashi, H., Yazawa, M., Hiruma, K., Katsuyama, T.: Crystal structure change of GaAs and InAs whiskers from zinc-blende to wurtzite type. Jpn. J. Appl. Phys. **31**,

2061-2065 (1992).

157. Hiruma, K., Yazawa, M., Katsuyama, T, Ogawa, K., Haraguchi, K., Koguchi, M., Kakiyabashi, H.: Growth and optical properties of nanometer-scale GaAs and InAs whiskers. J. Appl. Phys. **77**, 447-462 (1995).

158. Yeh, C.-Y., Lu, Z. W., Froyen, S., Zunger, A.: Zinc-blende-wurtzite polytypism in semiconductors. Phys. Rev. B **46**, 10086-10097 (1992).

159. Yeh, C.-Y., Lu, Z. W., Froyen, S., Zunger, A.: Predictions and systematizations of the zinc-blende-wurtzite structural energies in binary octet compounds. Phys. Rev. B **45**, 12130-12133 (1992).

160. Takeuchi, S., Suzuki, K.: Stacking fault energies of tetrahedrally coordinated crystals. phys. stat. sol. (a) **171**, 99-103 (1999).

161. Glas, F.: A simple calculation of energy changes upon stacking fault formation or local crystalline phase transition in semiconductors. J. Appl. Phys. **104**, 093520 (2008).

162. Akiyama, T., Nakamura, K., Ito, T.: Structural stability and electronic structures of InP nanowires: Role of surface dangling bonds on nanowire facets. Phys. Rev. B **73**, 235308 (2006).

163. Akiyama, T., Sano, K., Nakamura, K., Ito, T.: An empirical potential approach to wurtzite-zinc-blende polytypism in group III–V semiconductor nanowires. Jpn. J. Appl. Phys. **45**, L275-L278 (2006).

164. Shtrikman, H., Popovitz-Biro, R., Kretinin, A., Houben, L., Heiblum, M., Bukala, M., Galicka, M., Buczko, R., Kacman, P.: Method for suppression of stacking faults in wurtzite III-V nanowires. Nano Lett. **9**, 1506-1510 (2009)

165. Mutaftschiev, B., Kern, R., Georges, C.: Sur le mécanisme VLS de croissance des whiskers. Phys. Lett. **16**, 32-33 (1965).

166. Hilner, E., Håkanson, U., Fröberg, L. E., Karlsson, M., Kratzer, P., Lundgren, E., Samuelson, L., Mikkelsen, A.: Direct atomic scale imaging of III-V nanowire surfaces. Nano Lett. **8**, 3978-3982 (2011).

167. Sibirev, N. V., Timofeeva, M. A., Bol'shakova, A. D., Nazarenko, M. V., Dubrovskii, V. G.: Surface energy and crystal structure of nanowhiskers of III–V semiconductor compounds. Phys. Sol. State **52**, 1531-1538 (2010).

168. Algra, R. E., Vonk, V., Wermeille, D., Szweryn, W. J., Verheijen, M. A., van Enckevort, W. J. P., Bode, A. A. C., Noorduin, W. L., Tancini, E., de Jong, A. E. F., Bakkers, E. P. A. M., Vlieg, E.: Formation of wurtzite InP nanowires explained by liquid-ordering. Nano Lett. **11**, 44-48 (2011).

169. Kaplan, W. D., Kauffmann, Y.: Structural order in liquids induced by interfaces with crystals. Annu. Rev. Mater. Res. **36**, 1-48 (2006).

170. Dick, K. A., Thelander, C., Samuelson, L., Caroff, P.: Crystal phase engineering in single InAs nanowires. Nano Lett. **10**, 3494-3499 (2010).